Reservoir Characterization for the Upper Slochteren Formation for the Province of Utrecht to Research the Potential for Deep Geothermal Energy

Thesis report

by

Alex Heye

to obtain the degree of Master of Science in Applied Earth Sciences
at the Delft University of Technology
to be defended publicly on December 4, 2024 at 14:30

Thesis committee:

Chair:	Dr. Prof. D.B. Bruhn
Supervisors:	Dr. K.H.A.A. Wolf.
External examiner:	
Place:	Faculty of Civil Engineering & Geoscience, Delft
Project Duration:	April, 2021 - December, 2024
Student number:	4524500

Abstract

Deep Geothermal Energy, Province of Utrecht, Log Evaluations, Geological Modelling, Reservoir Characterization, Geothermal Exploration, Lower Permian Paleogeography

With the help of the Dutch Seismic Acquisition Program for Geothermal Exploration (SCAN), there is a growing nationwide interest in the exploration and development of Deep Geothermal Energy (DGE) by the geothermal industry. One geological target in the Dutch subsurface that could be suitable for harnessing DGE is the Upper Slochteren Formation of the Early Permian. Previous studies have revealed the geological property distributions of the formation in the densely populated Province of Utrecht. However, the facies distribution of the formation across the area has not explored yet. The thesis is objective is to gather information on the facies distribution of the Upper Slochteren Formation in the Province.

For this purpose, available core slabs from several wells in the region were studied and interpreted for their facies groupings. Each classified facies group is characterized by a specific range in porosity values. Additionally, seven well logs were analyzed for this thesis to evaluate the porosity, net sand, and permeability distributions of the Upper Slochteren Formation. By utilzing the resulting porosity borehole profile values and the 2D SCAN seismic sections, five facies units (aeolian dune (AD), interdune (ID), sandy sheet (SS), fluvial channels (FS), and flood sheet (SF)) were indentified and traced throughout the entire study area. The resulting facies distribution and corresponding geological property distributions are discussed to gain insight into the study area is paleogeographic setting and depositional environment during the Early Permian.

Firstly, for the area north of Amersfoort, the formation is characterized by favorable geological properties (average demonstrated permeability of 149.73 $[mD]$), making this area a high-potential geothermal case. Secondly, the facies maps reveal that the area mainly consisted of aeolian sandy sheet (SS) facies, ephemeral flood sheet (SF) facies, and ephemeral fluviatile channel (FC) facies units. The results also indicate that their distribution was irregular across the study area, with increased quantities of sandy sheet (SS) facies in the northeastern (northwestern Gelderland) and southwestern (Southeast Province of Utrecht) parts of the research area. Furthermore, the results show that at the beginning of the Early Permian period, the quantities of ephemeral flood sheet (SF) and fluviatile channel (FC) facies units were higher, while the amount of sandy sheet (SS) facies units was lower, in contrast to the end of the Early Permian period. Similarly, aeolian dune (AD) and aeolian interdune (ID) facies units were absent from the deposition area of the study region during the Early Permian period.

To better constrain the DGE potential for the Upper Slochteren Formation in the Province of Utrecht, it is recommended to retreive a 3D seismic cube for the high-potential case area. Additionally, it is advised to gather a large quantity of core plugs and core slabs from the Upper Slochteren Formation during future geothermal exploration drilling.

Acknowledgements

After exploring various fields in my early twenties, I founded my interest gravitating towards applied geology. Pursuing a Bachelor's in Applied Earth Science confirmed that this field resonated with my knowledge and scientific interests. The diverse geological excursions and applied exact sciences were areas where I excelled.

Upon obtaining my bachelor's degree, I aimed to deepen my understanding through a Master's track. The Geo Energy Engineering master's program immediately caught my attention due to its mixture of geology and renewable energy sources courses. During my Master's, the educational landscape underwent significant changes due to a global epidemic.

Nevertheless, I persevered to qualify myself as an engineer, culminating in my Master's thesis on Geothermal Energy. Despite facing challenges and missing concrete elements from the outset, I still had managed to complete my thesis. My gratitude go's to Prof. Dr. D.F. Bruhn for guiding me and providing valuable scientific input. Primarily, I thank my parents for their counsel and dedication.

Allow me to introduce my Master's thesis on Geothermal Energy to you with the following anecdote:

Glück Auf

Contents

Abbreviations

Bottom Hole Temperature	BHT
Bulk Water Volume	BWV
Compensated Density Log	CDL
Central Netherlands Basin	CNB
Compensated Neutron Log	CNL
Deep Geothermal Energy	DGE
Digitale Geologische Model-diep	DGM-diep
Dolomite Line	DOL
Density Porosity	DPHI
Delft Sandstone Member	DSSM
Sonic Time	DT
Gamma Ray	GR
Hydrogen Indices	HIs
Induction Deep	ILD
Potassium Mud	KCL
Laterlog Deep	LLD
Limestone line	LST
Logging While Casing	LTC
Medium Depth	MD
Micro Spherically Focused Log	MSFL
Wireline Logging	MWD
Net to Gross	NG
Dutch Oil and Gas Portal	NLOG
One-Way Travel Time	OWT
Peel-Maasbommel Complex	PMB
Repeated Formation Tests	RFT
Density Log	RHOB
Dutch Seismic Acquisition Program for Geothermal Energy	SCAN
Shale Resistivity Log	SN
Southern North Sea Basin	SNS
Square of the Sum of Residuals	SSR
Sandstone Line	SST
True Depth	TD
Netherlands Organisation for Applied Scientific Research	TNO
True Stratigraphic Thickness	TST
True Vertical Depth	TVD
Two-Way Travel Time	TWT
Variscan Mountain Belt	VMB
West Netherlands Basin	WNB
Zechstein Group	ZE

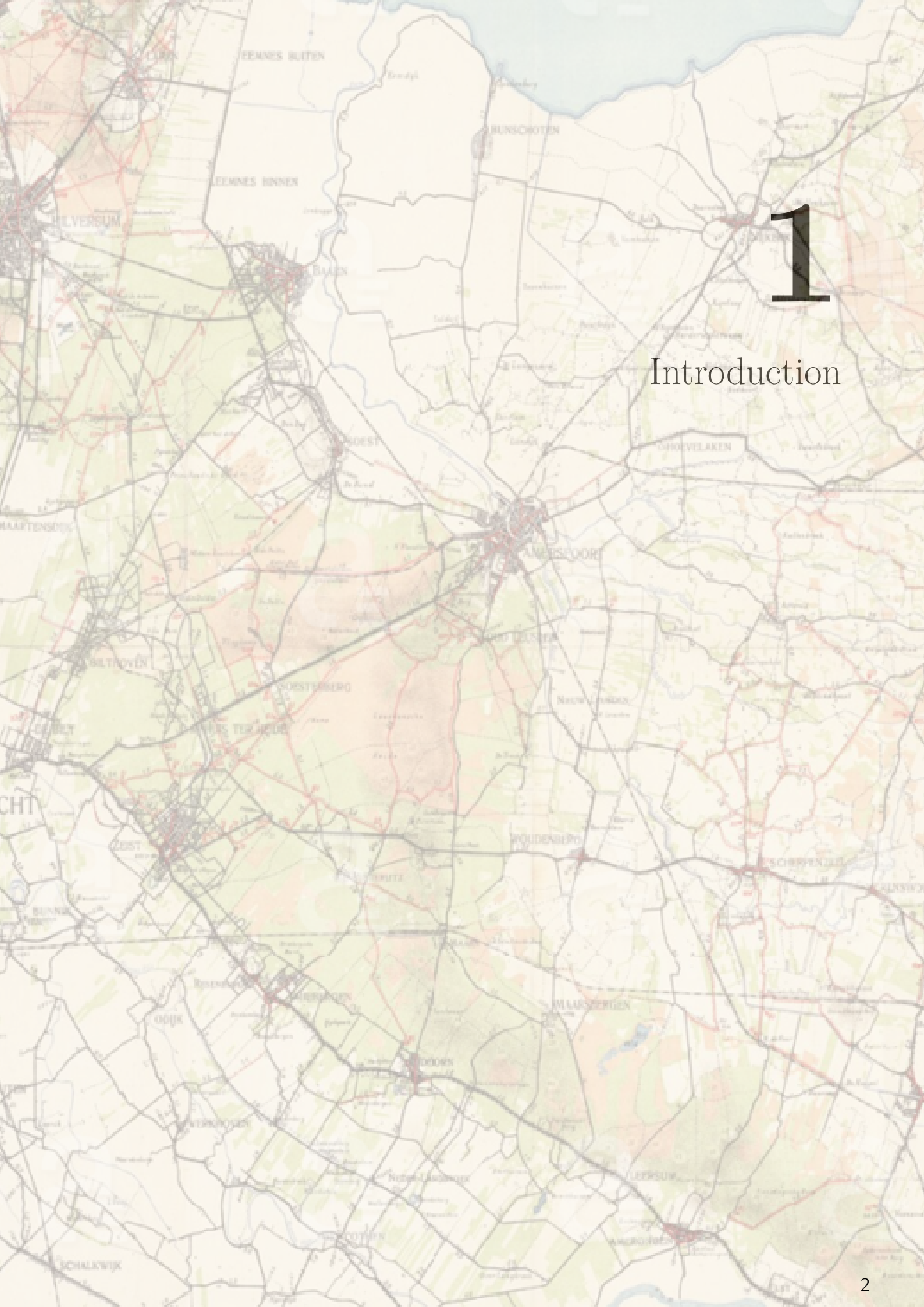

1

Introduction

1.1. The Topic

Geothermal energy, or the exploitation of underground heat sources, has a history dating back thousands of years for the usage of thermal baths and the first industrial installation for electricity generation at the start of the previous century. The exploration of the Geothermal field at Larderello in Italy in 1913 revealed the potential for electricity generation.

Other countries, such as New Zealand, the USA, Iceland, and Japan, followed after 1950 in harnessing geothermal energy for electrical power generation. Despite the commonality of these geothermal sources located in relatively active tectonic regions, it became evident that geothermal exploitation was also feasible in areas with reduced tectonic activity, such as in France and Germany.

Since the Paris Agreement mandates countries to maximize the usage of renewable energy sources in their energy mix, there has been increased interest in the Netherlands to utilize geothermal energy. Consequently, the Seismic Acquisition Program for Geothermal Energy (SCAN) was initiated in 2018 to map the subsurface of the Netherlands for geothermal exploration. The mission is to retrieve a comprehensive survey of underground areas that are relatively unknown in the Netherlands by acquiring seismic sections, thus assessing the potential of geothermal energy in the country Rehling, J., et al. (2020) **[34]**.

1.2. Geothermal Energy in The Netherlands

Before the initation of the Paris Agreement, due to hydrocarbon crises and rising gas and oil prices, there was already growing interest in the exploitation of geothermal energy in the Netherlands. As a result, some greenhouse owners, primarily in the Midwest of the Netherlands with high gas demand for their horticulture, began installing geothermal systems to provide the necessary heat for their greenhouses.

Despite the presence of the Delft Sandstone Member (DSSM) in the Lower Cretaceous of the Midwest Netherlands, exploration efforts expanded in 2012 with the initial drilling into the Upper Slochteren Formation in Koekoekspolder for geothermal purposes. While the initial two years of heat production were successful, a decline in production occurred due to salt clogging. Hereafter during the past ten years in total five doublets (Middenmeer, Middenmeer-2, Heemskerk, Andijk, & Luttegeest according to Buijze, L., et al. (2019) **[9]**) were drilled successively with the Upper Slochteren Formation as geothermal reservoir target.

Since the Upper Slochteren Formation was found at relatively great depths in various parts of the Dutch subsurface, SCAN identified this formation as a potential geological candidate for geothermal exploration (see the formation it's Dutch subsurface distribution as illustrated in Figure **1**). One densely populated area with high heat demand that could be fulfilled by geothermal energy is the Province of Utrecht.

Therefore, it is crucial to investigate the properties of the Upper Slochteren Formation to identify the potential for geothermal energy throughout the region. Before the early 21st century, the western part of the Netherlands underwent extensive hydrocarbon exploration, leading to the drilling of numerous wells in the Dutch subsurface. The Slochteren Formation, located at an ideal depth for hydrocarbon production, is noteworthy. The formation comprises two parts: the Lower Slochteren Formation, predominantly found in the northern Netherlands, and the Upper Slochteren Formation, widespread throughout the Dutch subsurface.

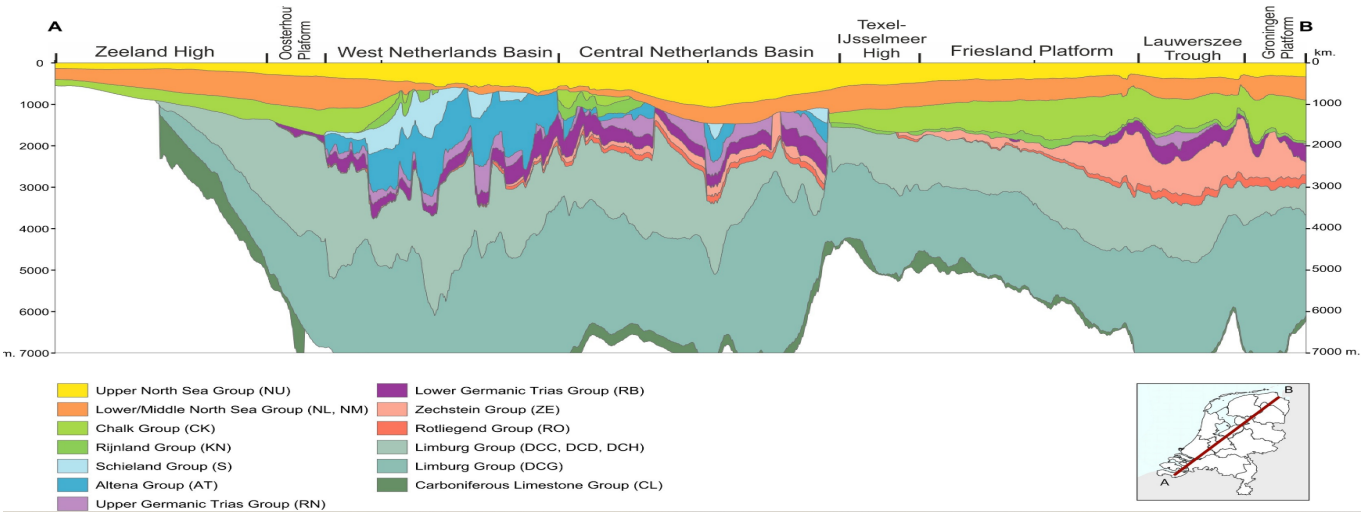

Figure 1: The southwestern to northeastern geological cross section of the Netherlands. The various colours: the geological formations found in the Dutch subsurface. From Békési, et al (2020) [4]).

1.3. Current State of Knowledge

Some studies in the past have already examined the characteristics of the geological unit throughout the area to determine its geothermal potential. Rijks Geologische Dienst (1983) **[34]** depicted the distribution of Early Permian deposition environments across the region based on borehole correlations and core analyses, revealing predominantly aeolian dune deposits. Rijks Geologische Dienst (1983) **[34]** also shown that the geological unit in the province of Utrecht is characterised by primarily high net sand values, ranging from 0.8 $[-]$ to 1 $[-]$.

Ponk, et al (2010) **[32]** indicated that the geological properties (porosity and permeability) of the unit in the area are elevated in the North and Central parts of the Province of Utrecht. However, a study by Boker, U & Leo, C (2021) **[7]** using SCAN seismic sections showed that the porosity and permeability distributions of the unit in the area differ from those presented by Ponk, et al (2010) [?].

The results of the research conducted by Boker, U & Leo, C (2021) **[7]** have not been incorporated in the latest version of the available Digitale Geologische Model-diep DGM-deep v5.0. This model is developed and reviewed by the Netherlands Organization for Applied Scientific Research (TNO). Since the study by Boker, U & Leo, C (2021) **[7]** primarily focused on determining the geological properties of the unit, the unit's facies distribution throughout the area was not considered in the study.

This facies distribution, however, would be crucial to assess whether the Upper Slochteren Formation is suitable for geothermal exploitation, for instance, to mitigate the risk of salt clogging. Therefore, the primary objective of my study is to map the facies distribution of this formation throughout the province.

1.4. Research Design

To investigate the facies distribution of the geological unit throughout the region, it is necessary to analyze core plugs extracted from the subsurface, allowing the identification of various facies units within the formation. Since these facies units are characterized by specific geological properties such as porosity, permeability, and sand content, it is crucial to classify the facies across the area to determine their characteristics.

The resulting facies distribution, firstly, indicates where in the area the favorable geological properties of the unit occur, thus revealing the enhanced geothermal potential. Secondly, the facies distribution provides insights into the depositional environment during the Early Permian, which, in turn, allows the reconstruction of the Early Permian paleogeographic distribution across the region. Ultimately, their distribution can be utilized to identify suitable areas throughout the Province for geothermal exploration.

1.5. The Research Questions

To address the previous mentioned thesis proposal of acquiring the facies distribution of the Slochteren Formation across the area, the following research questions are formulated:

1. What facies are present in the study area, and how are they distributed?

This primary research question is further subdivided into the following sub-questions:

1. What was the paleogeographic environment like during the sediment deposition?
2. How are the reservoir properties of the rock linked to the depositional environment?

To answer the stated research questions, core plugs from several wells around the research area were interpreted for their facies units and dominant sedimentation orientation during the Early Permian. Subsequently, available logs were evaluated to determine the distribution of net sand, porosity, and permeability along their borehole profiles.

Finally, a geological model was generated based on seismic sections, incorporating the resulting logs. By utilizing porosity facies cutoff values, facies units were up-scaled along the formation borehole profiles and then distributed across the entire geological model, resulting in the ultimate facies distribution map across the area.

1.6. Thesis Outline

To execute the thesis approach, the thesis is structured as follows: The methods, which include the core plug analysis and the log analysis are discussed in Chapter **2**. Subsequently, Chapter **3** covers the construction of the geological model, detailing the resulting facies distribution and the porosity, permeability, and net sand distributions across the area. Following this, Chapter **4** presents the ultimate conclusions of this study, with recommendations for future research in Chapter **5** (the thesis outline is illustrated below in Figure **2**).

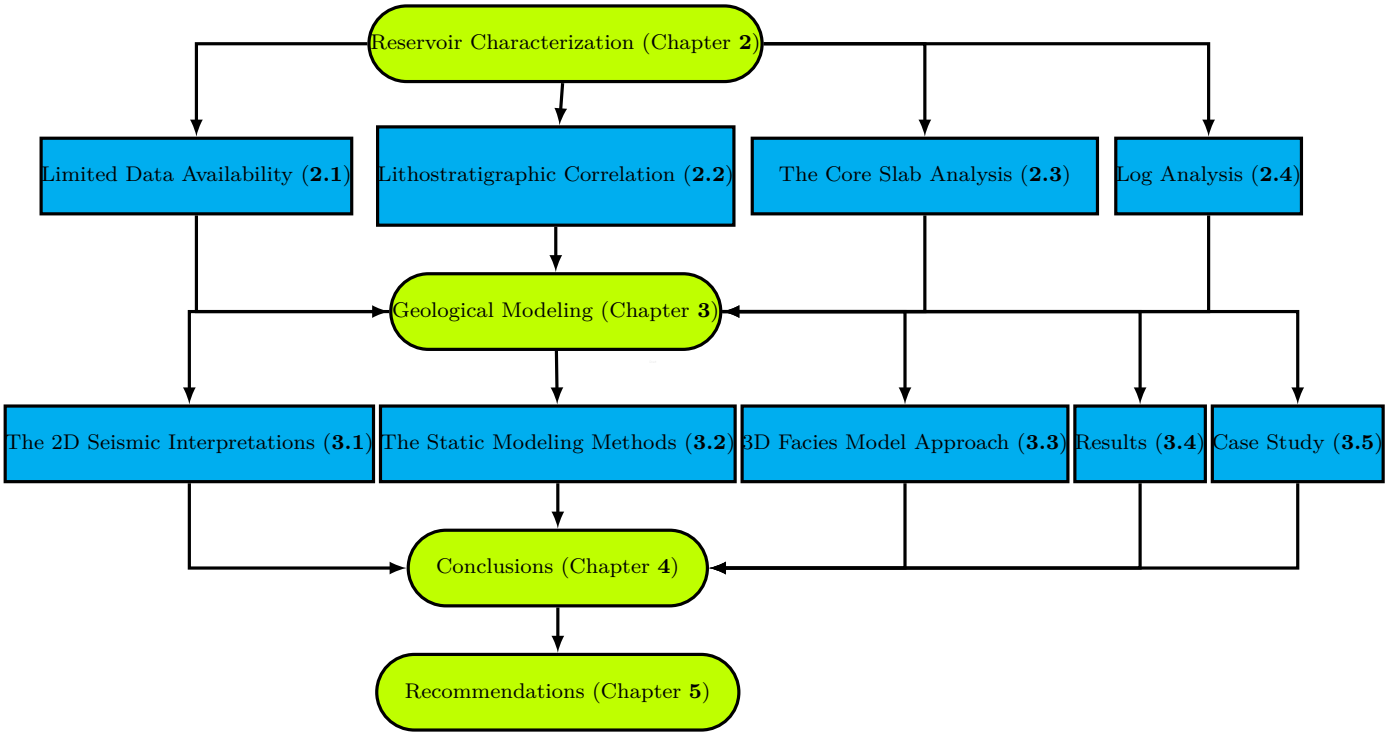

Figure 2: Lime coloured rectangles: the introduction and the concluding chapters, cyan coloured rectangles: the methods and analysis sections, and black arrows: the relations between the individual chapters and sections.

1.7. Geology of the Upper Slochteren Formation

During the late Carboniferous, when swamp deposits dominated the regional surface geology, a shift in climate led to the formation of aeolian dune and sabkha deposits at the beginning of the Permian era. This change in sediment deposition is marked by a stratigraphic hiatus known as the Base Permian Unconformity (BPU).

Due to the warm and arid climate, along with the absence of drainage from the Variscan Belt to the former Southern Permian Basin (SPB), there was no transport of water and sediment. Additionally, the presence of the Variscan Belt in the surrounding areas resulted in substantial accumulation of the Upper Slochteren sediment in the SPB during the Early Permian.

Primarily, coarse-grained sediment was transported towards the edges of the SPB through alluvial fans and subsequent braided river systems. Subsequently, further movement of fine-grained sediment occurred through the wind, leading to the formation of dune fields or erg systems Glennie, K. W. (2010) **[17]** (as illustrated in Figure **3**).

To increase regional knowledge of the Upper Permian period, it's paleogeography, the facies distribution at the start and at the end of this period are determined, and are presented within their maps as discussed in chapter **3**.

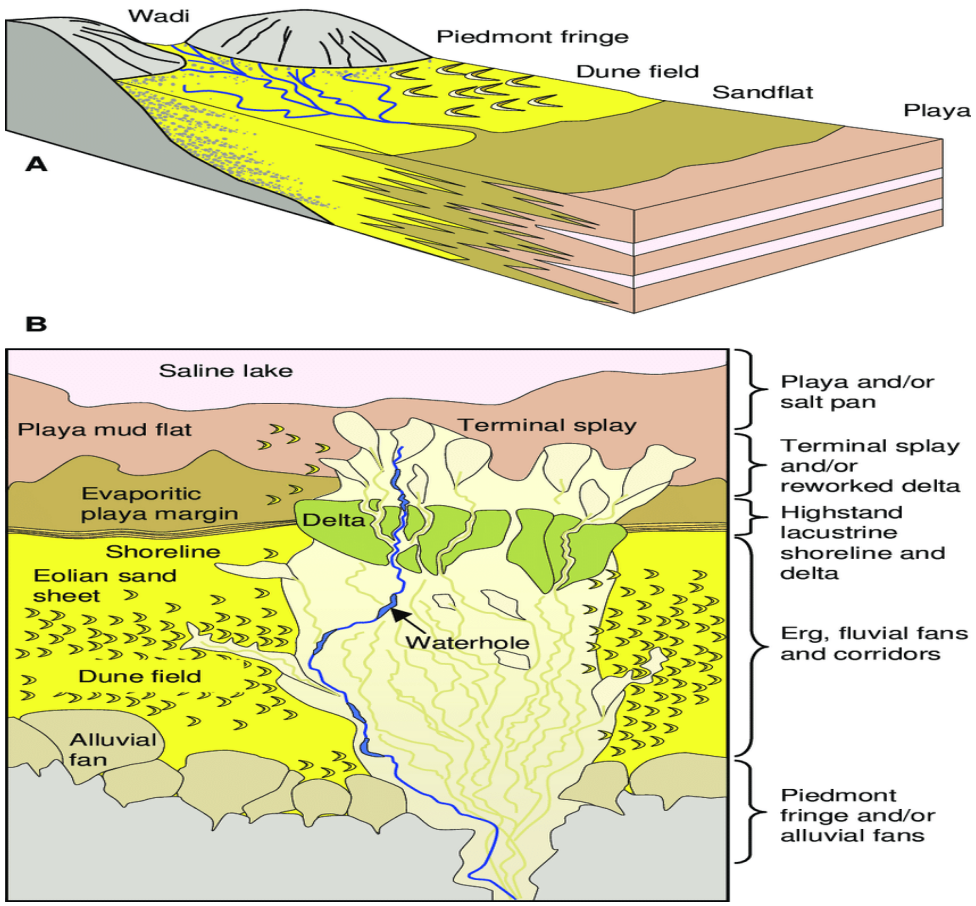

Figure 3: Above: the 3D Lower Permian depositional block diagram across the Dutch subsurface, below: the depositional environment distribution across the Netherlands. The figure is retrieved from Mckie, T. (2011) [**28**].

1.8. The Structural Geology of the Region

Throughout the geological history since the Early Permian, various tectonic events occurred, which shaped the current subsurface conditions in the Province of Utrecht. The breakup of the supercontinent Pangea led to ongoing extension, resulting in the development of normal fault lines in the subsurface, primarily present in the geological formations deposited during the Cretaceous and Jurassic eras.

Other events included the collision of the African Plate and the Iberian plate with the Eurasian plate. As a consequence, subsurface compression occurred in the study area, leading to the presence of reverse fault lines in the subsurface. Additionally, pre-existing normal fault lines were reactivated due to compression phases occurring during the Late Mesozoic (Cretaceous) and the Early Cenozoic (Paleogene).resulting in the development of flower structures in the subsurface.

Tectonically, the Dutch subsurface can be subdivided into highs, basins, edges, and platforms due to the previous mentioned events. For the subsurface of the Province of Utrecht, the structural map by Duin, E. J. T, et al (2006) **[14]** highlights the following geological structures: the Central Netherlands Basin (CNB), the Zandvoort Ridge (ZR), and the Peel-Maasbommel Complex (PMB).

1.9. The Stratigraphy of The Regional Subsurface

As the geothermal potential depends not only on the reservoir formation but also on the underlying (bottom rock) and overlying (cap rock) formations, it is crucial to also investigate the geological properties of both formations across the study area (as listed in Table **1**).

TNO has publicly presented maps for each layer and for each formation, inspecting their occurrence and dominant lithology TNO-GDN.(2019) **[41]**. It appears that the Lowest Z1 Claystone Layer of the Zechstein Group (ZE) is identified as the corresponding cap rock in the area. According to the TNO database, this layer mainly consists of claystone with irregular intercolations of limestone beds. The bottom rock of the Upper Carboniferous period was found to vary across the study area. Around the BLA-01 borehole position, it is formed by the Hellevoetsluis Formation and it's Dutch subsurface distribution (as depicted in Figure **4**), while elsewhere in the area, the bottom formation is represented by the the Maurits Formation, belonging to the Caumer Subgroup. The Hellevoetsluis Formation is mainly composed of siltstones with intercalations of sandstones, and the layers of the Caumer Subgroup consist predominantly of claystones with intercalations of coal beds TNO-GDN.(2017) **[40]**.

From these findings, it could be hypothesized that due to the reduced permeability of claystones, the Caumer Subgroup and the Lowest Z1 Claystone Layer could be favorable as cap and bottom rocks. However, the permeable nature of the sandstones in the Hellevoetsluis Formation could have a detrimental effect as a bottom formation, potentially resulting in lower production from the reservoir formation.

Table 1: Below the regional lithostratigraphic column has listed.

Geological Era	Formation
Upper Permian	Z1 Lower Claystone Layer
Lower Permian	Upper Slochteren Sandstone
Upper Carboniferous	Hellevoetsluis Formation and/or Caumer Subgroup

Figure 4: The Hellevoetsluis Formation distribution (gray shaded area) throughout the Netherlands, as retrieved from TNO-GDN.(2017) [40].

2

Reservoir Characterization

As mentioned in previous studies and the public DGM-v5.0 model, the regional facies distribution of the Upper Slochteren Formation is lacking. Therefore, to constrain the geothermal potential of the formation in the Utrecht region, it is useful to create this regional facies model. As the reservoir properties of the formation are needed for the further assessment of the geothermal potential, this chapter addresses methods to map both the geological property distributions and the facies distribution of the Upper Slochteren Formation.

2.1. Limited Available Data

Due to time constraints, only the facies and geological properties of the reservoir formation are investigated here, excluding those of the upper and lower formations. Seven wells are selected, with True Depths (TD) reaching and exceeding the Upper Slochteren Formation. Information on these wells can be accessed on NLOG. As these boreholes were drilled by the hydrocarbon industry and did not show exploitable gas quantities, not all data (logs and cores) were acquired by them (as listed in Table **4**).

Core plugs and core slabs are available from various wells in both the Geological Core Archive of TNO and the Nederlandse Aardolie Maatschappij (NAM). Core plugs are rock samples extracted by a tool along the borehole and brought to the surface. Since retrieving such samples is time-consuming, core plugs are not available for the entire formation or every well. For the determination of the regional facies distribution, core slabs were analyzed for their grain size and sorting, mineral composition (lithology), sedimentation patterns, bioturbation, and bedding patterns. Available cores for wells WSP-01, BNV-01, ERM-01, and JUT-01 were inspected for these characteristics at their respective locations (as presented in Table **2**). Core analyses are discussed in Section **2.3** of this thesis.

All available seismic data on NLOG across this study area consist of 2D seismic sections. Included in this study were 2D seismic sections published by SCAN and older reprocessed 2D seismic sections from van Lochem, H., et al. (2021) **[27]** (as listed in Table **3**). The SCAN seismic sections used for mapping the formation in the area are shown in Figure **5**.

Table 2: List of core intervals (including: Top and Bot depth) along the boreholes

Borehole	***WSP-01***	***JUT-01***	***ERM-01***	***BNV-01***
Length of core $[m]$	2.7	18	6.5	3
Top depth $[m]$	2192	3256	2640.5	3039
Bottom depth $[m]$	2194.7	3274	2647	3042

Table 3: List of the 2D seismic sections used (including: SCAN & Post processed). *NA*: 2D seismic section was not retrieved.

***SCAN** (sections*	***GTO-19-C011** (sections)*	***GTO-18-C004** (sections)*	***GTO-19-C033-01** (sections)*	***GTO-19-C033-02** (sections)*
SCAN001	NA	NA	NA	NA
SCAN004	L2NAM1982F/L2NAM1984N (NAMDeep)	L2M0B1984A(8413)	L2MOB1986A (MZ86-56)	L2PET1980D (HL-80-08)
SCAN011	NA	L2MOB1985A (8507)	MZ86-70	AM86-15-D
DUGOU022	NA	L2MOB1984A (8412)	MZB5-20/21	AM86-06-D
SCAN023	NA	L2MOB1984A (8508)	MZ87-14	AM68-57-D1
SCAN024	NA	L2MOB1984A (8411)	MZ86-11	H80-06
SCAN025	NA	L2MOB 31985A (8503)	MZ85-16	HL80-05
SCAN028	NA	NA	NA	ZYB3-03
	NA	NA	NA	AM87-05

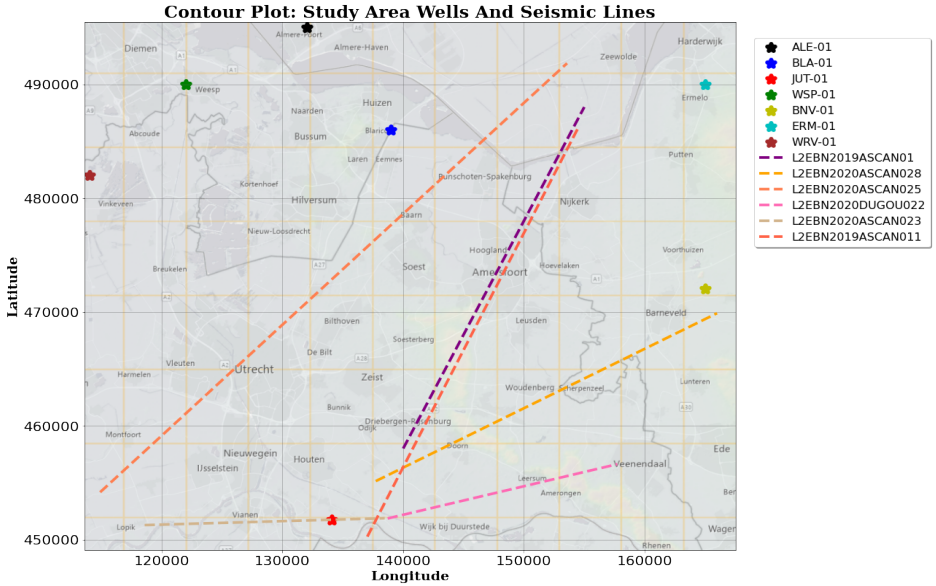

Figure 5: Coloured stars: the well head locations of the seven wells, coloured lines: The 2D SCAN seismic section trajectories as received from NLOG, map: The study area.

Table 4: Well information header; well logs, completion mud composition, formation depth intervals, available core plugs, operator **NA**; no available bottom formation, **N**; no available core plug data, and *; Bottom formation is the Hellevoetsluis Formation TNO-GDN.(2017) [**40**].

Well (code)	*Year (completed)*	*Operator (log acquisition)*	*Logs (measured)*	*Drilling mud (type)*	*Depth top/bottom Cap Rock [m]*	*Depth top/bottom Reservoir Rock [m]*	*Depth top/bottom rock [m]*	*Available Core Plugs (ϕ and k)*
ALE-01	1976	Amoco (MWD)	CAL, GR, DT, RHOB, NPHI, ILD, MSFL, DT	Gypsum Mud HCL	1715.00-1735.00	1735.00-1858.00	1858.00-1877.00	N
BLA-01	1982	Elf Petroland (MWD)	CAl, GR, DT, RHOB, NPHI, ILD, MSFL, DT	XCL Polymer	1487.00-1503.50	1503.50-1642.00	1642.00-1985.00*	ϕ & k
JUT-01	1968	NAM (MWD)	CAL, DT, RHOB, DT, SP	XCL Polymer	3215.00-3240.00	3240.00-3378.00	3378.00-3409.00	ϕ
ERM-01	1969	NAM (MWD)	CAL, GR, DT, RHOB, ILD, MSFL, DT	XCL Polymer	2614.00-2621.00	2621.00-2649.00	NA	ϕ
WSP-01	1970	Amoco (MWD)	CAL, GR, DT, RHOB, ILD, MSFL, DT, SP	XCL Polymer	2168.00-2192.00	2192.00-2197.00	2197.00-2259.00	N
WRV-01	1971	Amoco (MWD)	GR, RHOB, DT	XCL Polymer	2330.00-2340.50	2340.50-2351.50	2351.50-2458.00	N
BNV-01	1971	Amoco (MWD)	DT	XCL Polymer	2927.00-2942.00	2942.00-3043.00	3043.00-3066.00	N

2.2. The Lithostratigraphic Correlation

In order to gain insight into the extension of the Upper Slochteren Formation throughout the study area, a stratigraphic borehole correlation was created. Initially, lithostratigraphy profiles from wells on NLOG indicated that the distribution of the formation in the area is highly irregular. The formation reaches a maximum top depth of 2942.0 m in well BNV-01 and a minimum depth of 1503.5 m in well BLA-01. Additionally, the True Stratigraphic Thickness (TST) of the formation shows irregularities, with a maximum thickness of 138.5 m measured in well BLA-01 and a minimum thickness of 5 m in well WSP-01. Chapter **3** further explains the TST distribution of the formation throughout the study area.

Since Grötsch, J., & Gaupp, R. (2011) **[20]** demonstrated that stratigraphic correlation based on fossil imprints (biostratigraphy) for the Upper Slochteren Formation seems nearly impossible due to the lack of biotic variation in the SPB, alternative stratigraphic correlation methods were sought. Moreover, Grötsch, J., & Gaupp, R. (2011) **[20]** indicated that significant changes in atmospheric isotope concentrations were not recorded in the sediments of the formation due to the relatively short duration of the geological era of 26.7 $[Ma]$ and the relatively high sediment accumulation rate during the Early Permian period.

Given the limitations of the above mentioned correlation methods, and since most wells have both Gamma Ray (GR) logs and Sonic Time (DT) logs, both indicative of lithology, stratigraphy correlation was based on lithology.

From the resulting three well correlations (ALE-01-JUT-01, WRV-01-ALE-01, and WSP-01-BLA-01), it is evident that GR values along the borehole profiles are between 10 $[API]$ and 30 $[API]$ (as illustrated in Figures **6**, **7**, & **8** and corresponding borehole correlation trajectories as presented in Appendix **A.1**). Additionally, no significant differences appear in the GR profiles, indicating that the formation has relatively homogeneous lithology predominantly composed of sandstones.

DT profiles indicate oscillations between 50 $[\frac{\mu s}{ft}]$ and 90 $[\frac{\mu s}{ft}]$, with maximum values observed in well BLA-01. These values imply that the formation is not composed of limestone or dolomite, as DT $<$ 50 $[\frac{\mu s}{ft}]$ would suggest, but primarily consists of sandstones.

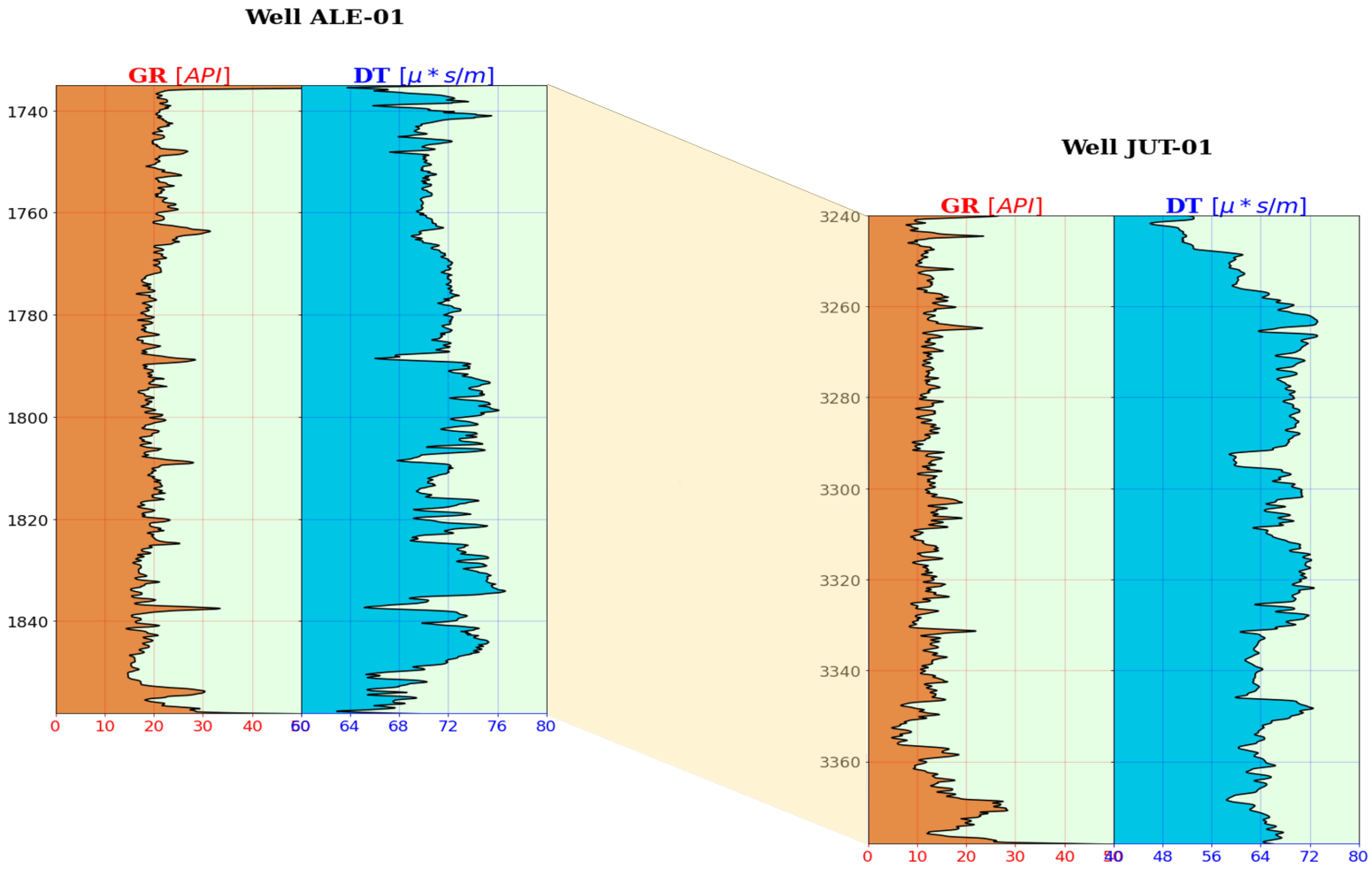

Figure 6: The well correlation analysis was conducted for wells ALE-01 and JUT-01, considering the inclusion of both GR and DT logs. The detailed correlation trajectory is available in Figure 56 (Appendix **A1**).

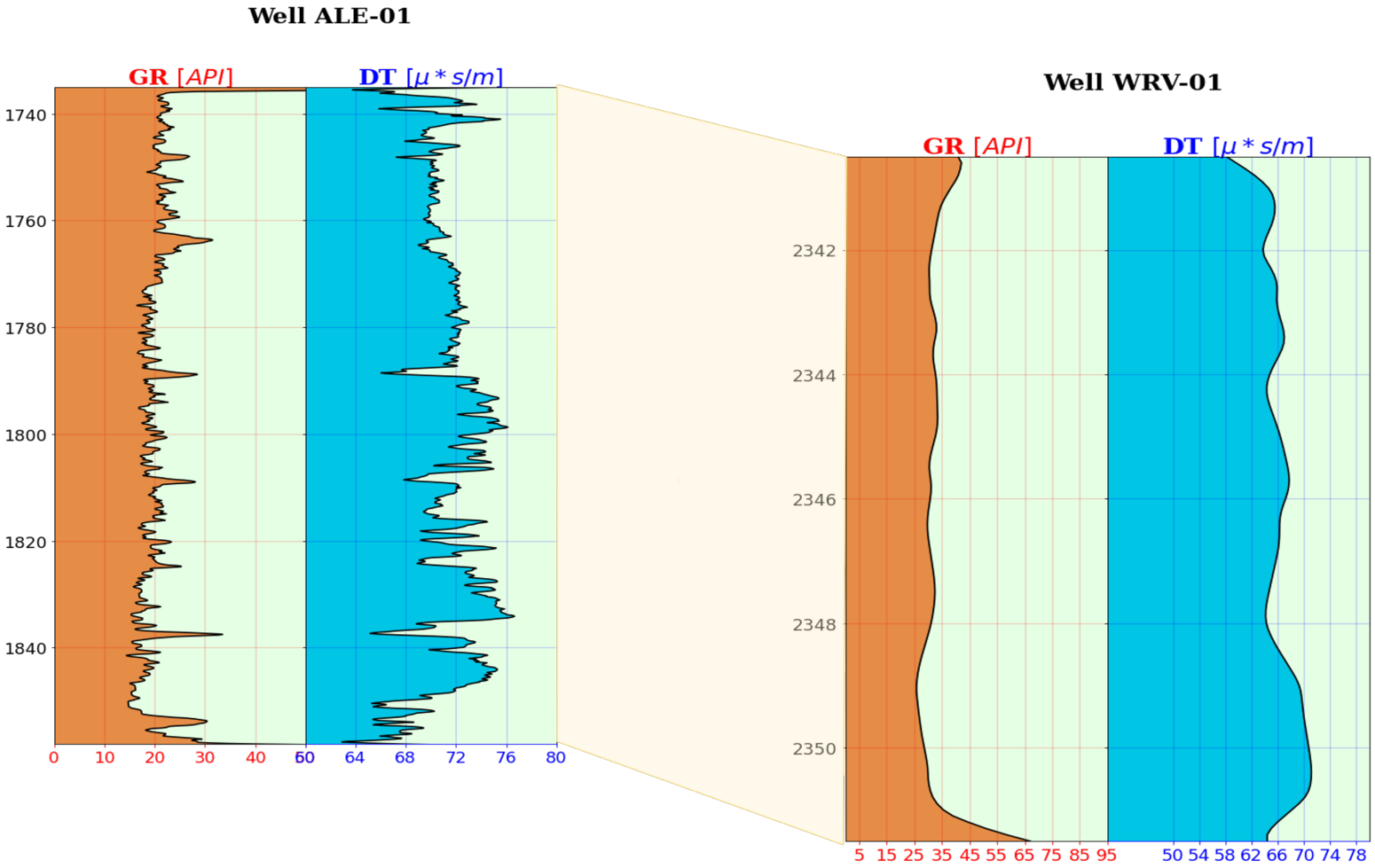

Figure 7: Additionally, a well correlation analysis was performed for wells WRV-01 and ALE-01, with the same logs (GR and DT) included. The comprehensive correlation trajectory is provided in Figure 57 (Appendix **A1**).

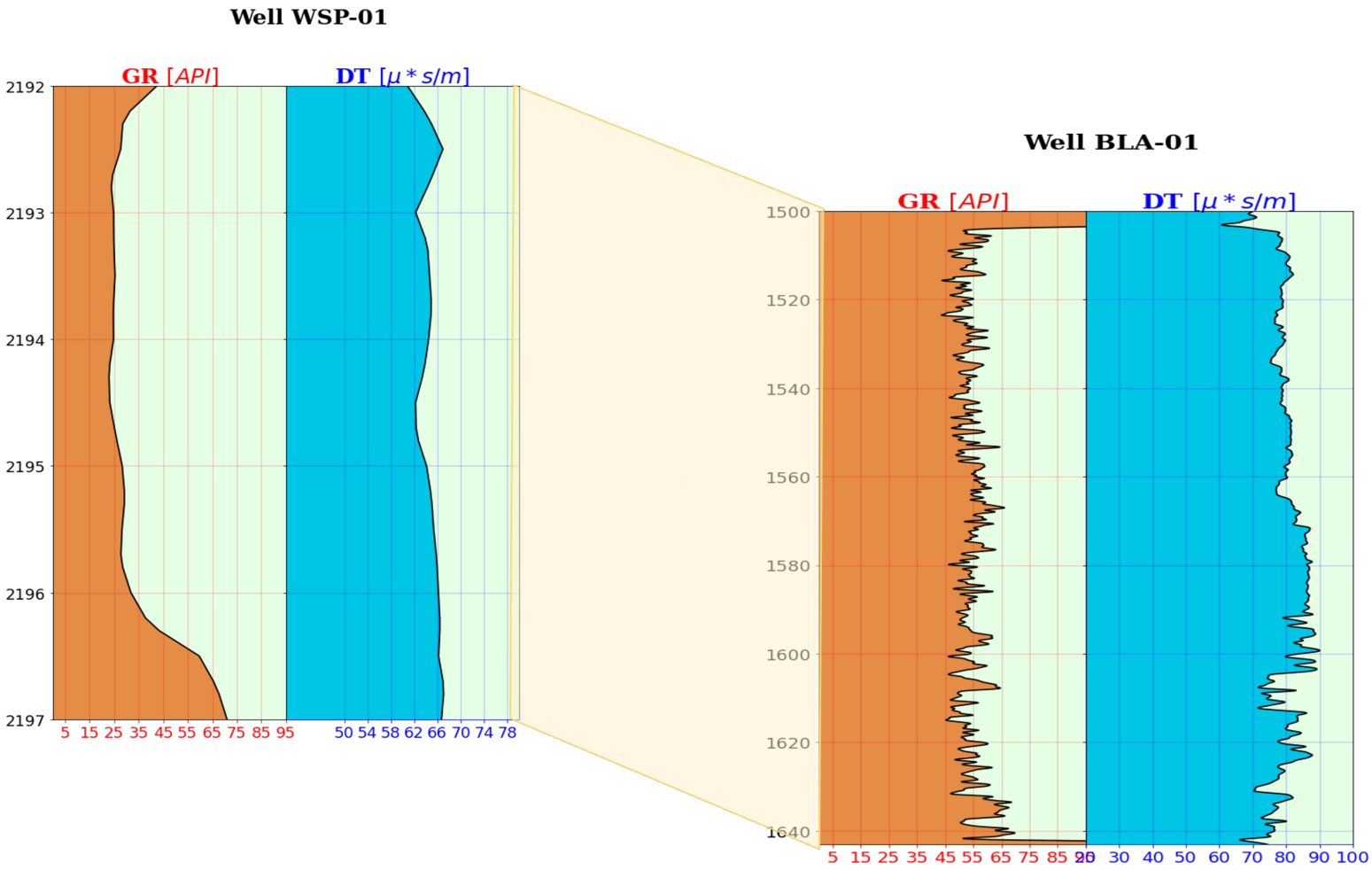

Figure 8: Furthermore, a well correlation study was carried out for wells WSP-01 and BLA-01, again incorporating the GR and DT logs. The complete correlation trajectory can be found in Figure 58(Appendix **A1**).

2.3. The Core Slab Analysis

As discussed in the preceding section, core slabs from various wells are available at Geological Core Management Locations. During the preparation of this thesis, facies and paleo-orientation analyses were conducted for core slabs from WSP-01, BNV-01, JUT-01, and ERM-01. These core slabs were interpreted for grain size and sorting distributions, sedimentation and bedding patterns, mineral composition, and bioturbation. The details can be referred to in the lithostratigraphic columns for these core slabs (Appendix **A.2**).

Based on these interpretations and similar facies identified in the study by Priddy, C. L., & Clarke, S. M. (2021) **[33]**, lithofacies and facies groupings were identified for these core slabs, detailed in facies tables (Appendix **A.3**). Additionally, the distributions of these facies and their corresponding occurrences in the core slabs were identified. Finally, depositional structures as recognized from the core slabs are identified and are evaluated, to ascertain both the wind and the river directions prevailing in the early Permian period. Chapter **3** further discusses the results of this core slab analysis for generating the facies distribution of the formation.

2.3.1. The Core Slab Observations

The core slab observations for ERM-01, WSP-01, BNV-01, and JUT-01 conducted on-site were digitally documented for their visible features.

The WSP-01 Core Slab

As noted in Table **2**, the core slab of WSP-01 spans a total length of 2.7 meters. It has a beige to dark gray color, characterized by moderate to severe structural features such as fractures and stylolites. The grain sorting ranges from moderately- to well-sorted, while the grain size distribution varies from fine-grained siltstones to medium-grained sandstones.

At the top of the WSP-01 core slab, starting at a depth of 2192.0 meters, the rock is characterized by cross-laminated fine-grained sandstones. That is transitioning at a depth of 2193.0 meters into undulating cross-laminated sandstones and finally into a 0.1-meter thick homogeneous medium-grained siltstone bed. Further down to a depth of 2193.6 meters, parallel-laminated fine-grained sandstones can be identified, transitioning to predominantly massive coarse-grained siltstones extending to a depth of 2194.7 meters to the bottom of the core slab. The WSP-01 core slab interpretations and the corresponding trends in grain size distributions are presented in Figures **10**, **11**, & **12**. The overall legend for core slab interpretation (see Figure **9**) applies for WSP-01 and the subsequent wells BNV-01, ERM-01, and JUT-01.

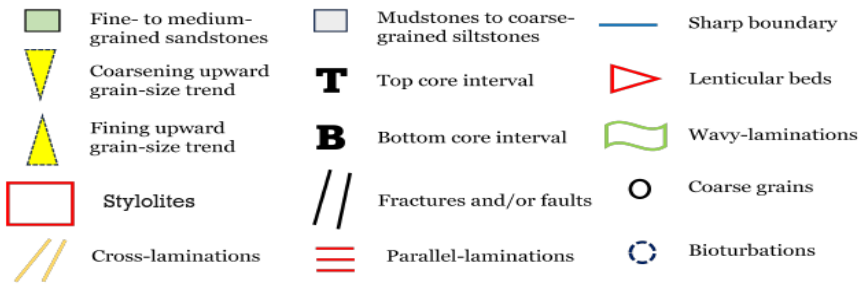

Figure 9: The legend shown above holds for the Figures **10** unto **22** as following below.

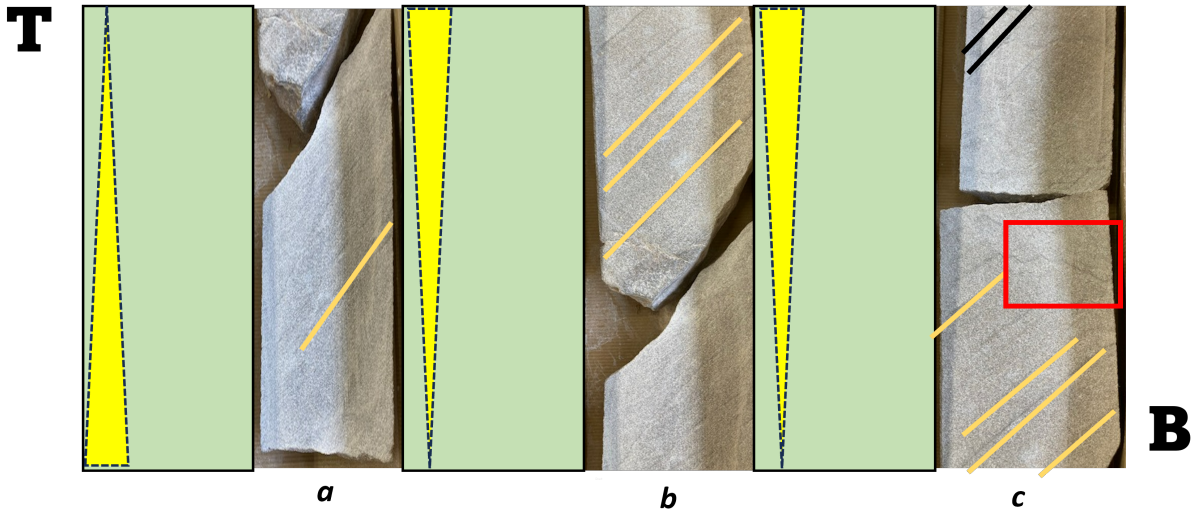

Figure 10: The letters denote the following depth intervals, from top to bottom along the WSP-01 core slab: **a**= 2192.3 [m] to 2192.0 [m], **b**= 2192.5 [m] to 2192.3 [m], and **c**= 2192.7 [m] to 2192.5 [m]. The symbols included within the image are defined according to the legend in figure **9**.

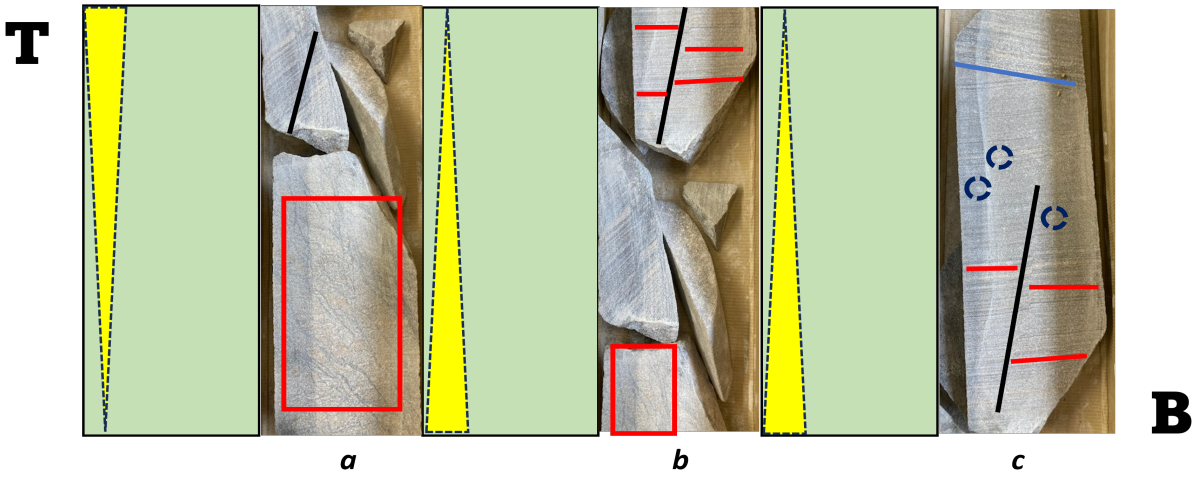

Figure 11: The letters denote the following depth intervals, from top to bottom along the WSP-01 core slab: **a**= 2192.7 [m] to 2192.9 [m], **b**= 2193.2 [m] to 2192.7 [m], and **c**= 2193.5 [m] to 2193.2 [m]. The symbols included within the image are defined according to the legend in figure **9**.

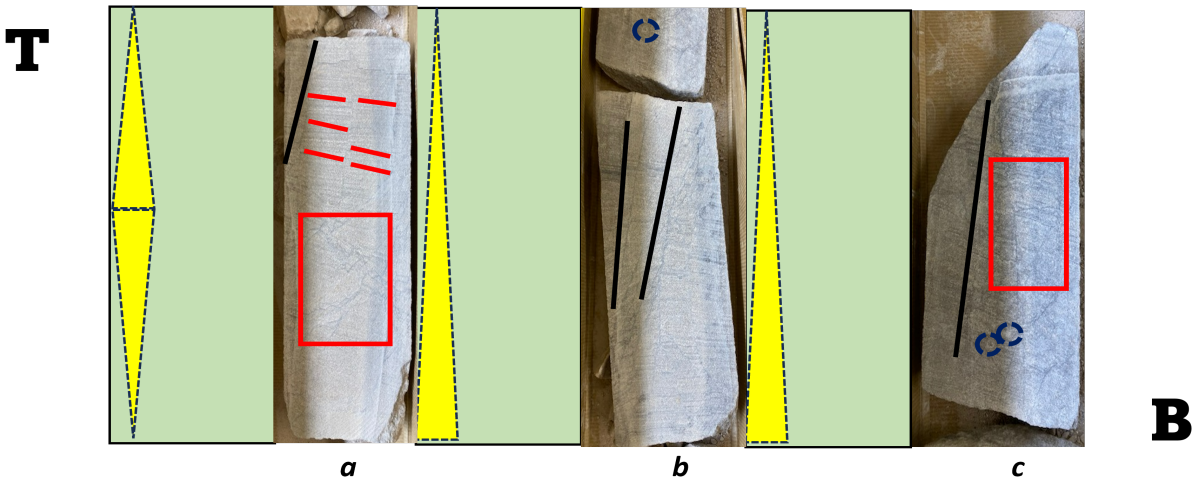

Figure 12: The letters denote the following depth intervals, from top to bottom along the WSP-01 core slab: **a**= 2193.7 $[m]$ to 2193.5 $[m]$, **b**= 2194.0 $[m]$ to 2193.7 $[m]$, and **c**= 2194.4 $[m]$ to 2194.0 $[m]$. The symbols included within the image are defined according to the legend in figure **9**.

2.3.2. The BNV-01 Core Slab

As previously identified, the BNV-01 core slab spans a total length of 3.3 meters (see Table **2**). The BNV-01 core slab is characterized by a light gray to light brown color, with sorting ranging from poorly sorted to very well-sorted. The grain size distribution and lithology fluctuate from fine-grained siltstones to medium-grained sandstones.

On the bottom of the BNV-01 core slab, at 3042.3 meters to 3041.6 meters depth, the rock is characterized by cross-laminated medium-grained sandstones. Subsequently, at a depth of 3040.7 meters, parallel-laminated fine-grained sandstones are dominating, transitioning further into massive medium-grained sandstones up to a depth of 3039.9 meters. The rock also features laminated fine-grained sandstones, transitioning into a 0.05-meter thick homogeneous fine-grained siltstone bed. Moving up to the top of the BNV-01 core slab, the rock is characterised by cross-laminated medium-grained sandstones. The BNV-01 core slab interpretations are presented in the following schematics (see Figures **13**, **14**, **15** & **16**).

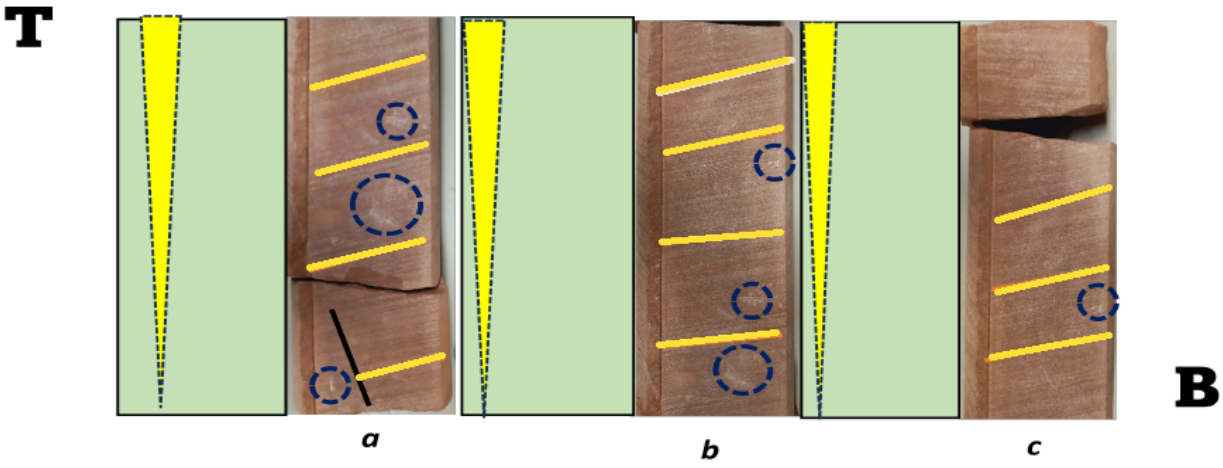

Figure 13: The letters denote the following depth intervals, from top to bottom along the BNV-01 core slab: **a**= 3039.3 $[m]$ to 3039.0 $[m]$, **b**= 3039.5 $[m]$ to 3039.3 $[m]$, and **c**= 3039.8 $[m]$ to 3039.5 $[m]$. The symbols included within the image are defined according to the legend in figure **9**.

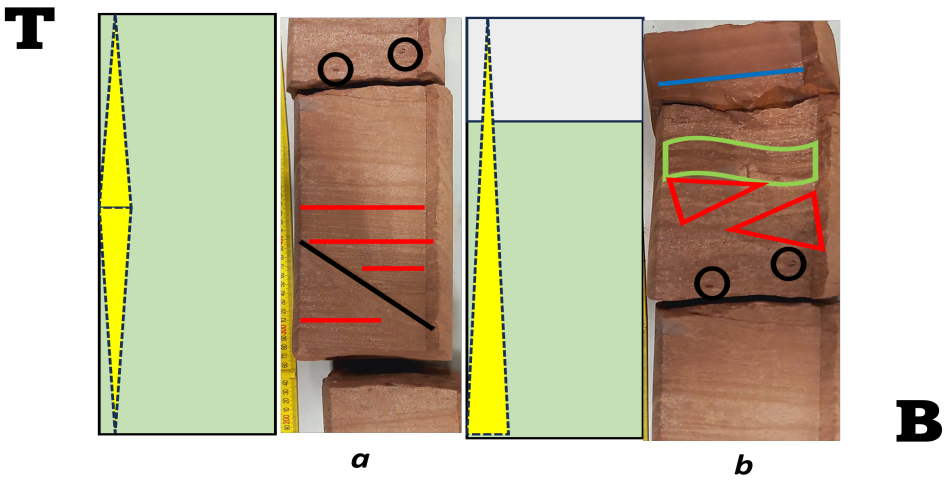

Figure 14: The letters denote the following depth intervals, from top to bottom along the BNV-01 core slab: **a**= 3040.1 $[m]$ to 3039.8 $[m]$, **b**= 3040.4 $[m]$ to 3040.1 $[m]$. The symbols within the image are presented according to the legend in figure **9**.

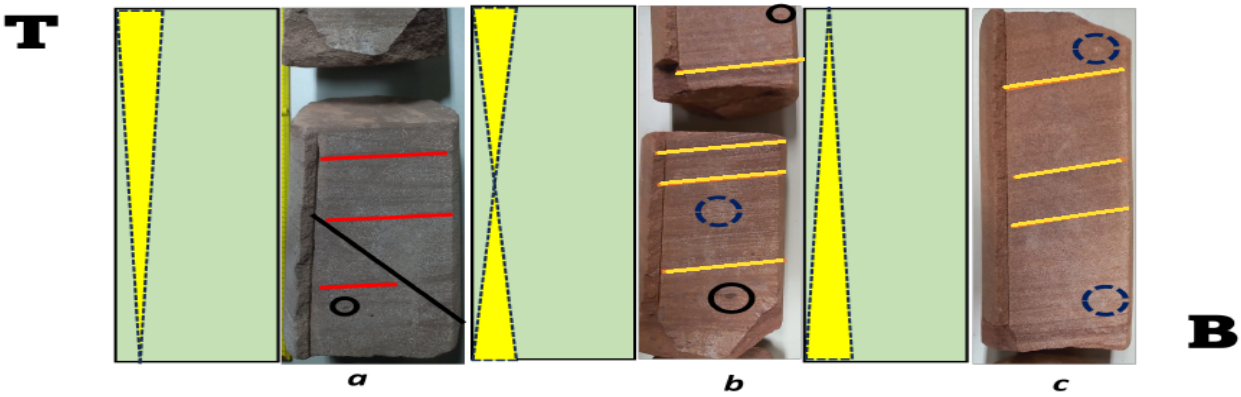

Figure 15: The letters denote the following depth intervals, from top to bottom along the BNV-01 core slab: **a**= 3040.7 $[m]$ to 3040.4 $[m]$, **b**= 3041.1 $[m]$ to 3040.7 $[m]$, and **c**= 3041.6 $[m]$ to 3041.1 $[m]$. The symbols included within the image are defined according to the legend in figure **9**.

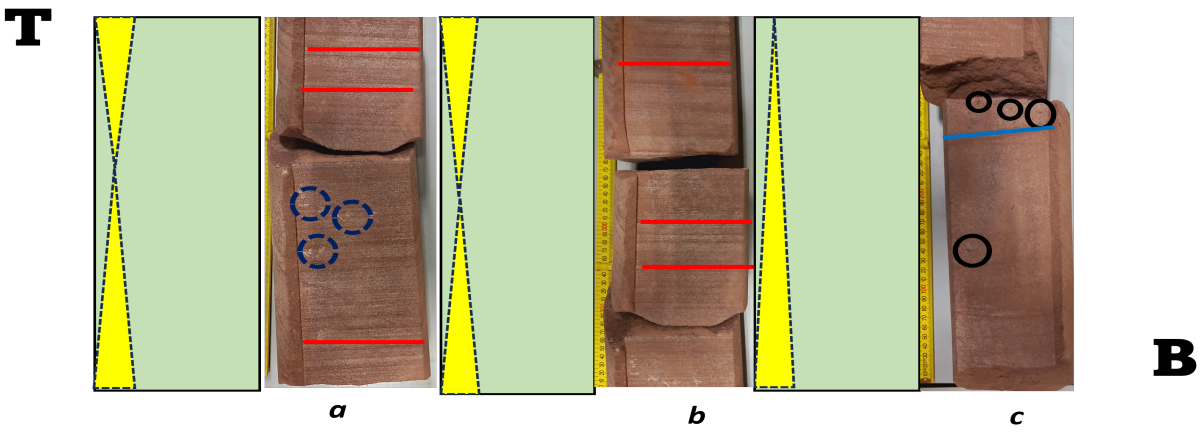

Figure 16: The letters denote the following depth intervals, from top to bottom along the BNV-01 core slab: **a**= 3041.8 $[m]$ to 3041.6 $[m]$, **b**= 3042.0 $[m]$ to 3041.8 $[m]$, and **c**= 3042.3 $[m]$ to 3042.0 $[m]$. The symbols within the image are presented according to the legend in figure **9**.

The ERM-01 Core Slab

As mentioned earlier, the ERM-01 core slab spans a total length of 6.5 meters (see Table **2**). The core slab ERM-01 is identified by an overall beige to light gray color, with a grain size distribution ranging from medium to coarse grain sandstones. The core slab's grain sorting is predominantly poorly.

For the bottom of the core slab, from 2647.0 meters to 2641.5 meters depth, the rock is characterized by massive coarse-grained sandstones. From 2641.5 meters, it transitions into cross-laminated medium-grained sandstones up to the top at 2640.5 meters. The core slab interpretations and the corresponding grain-size trends are presented in Figures **17** & **18**.

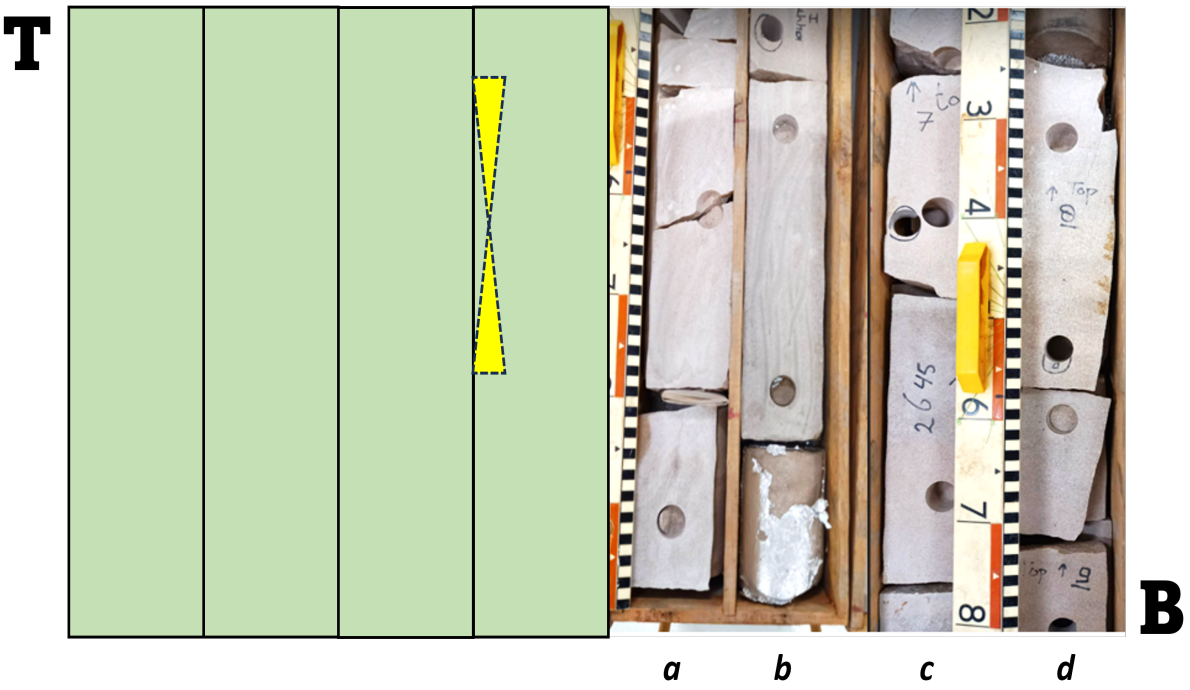

Figure 17: The letters denote the following depth intervals, from bottom to top along the ERM-01 core slab: **a**= 2646.8 [m] to 2647.5 [m], **b**= 2645.9 [m] to 2646.8 [m], **c**= 2645.0 [m] to 2645.9 [m], and **d**= 2644.0 [m] to 2645.0 [m]. The symbols included within the image are defined according to the legend in figure **9**.

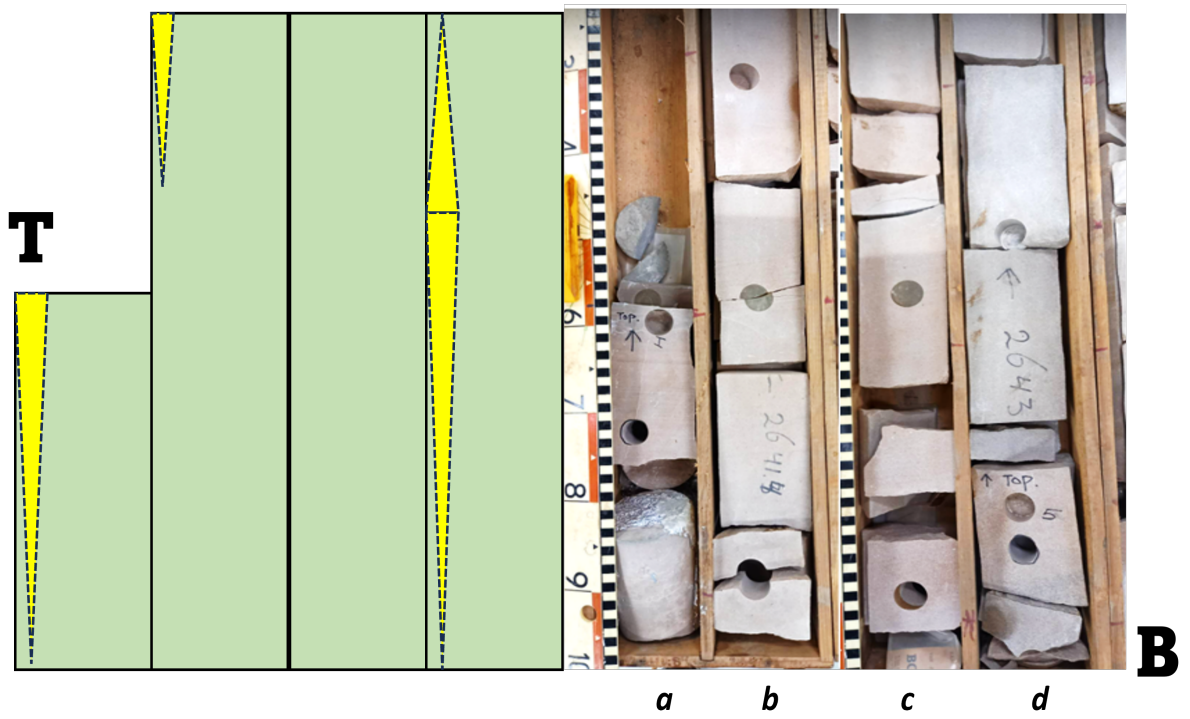

Figure 18: The letters denote the following depth intervals, from bottom to top along the ERM-01 core slab: **a**= 2643.5 [m] to 2644.0 [m], **b**= 2642.5 [m] to 2643.5 [m], **c**= 2641.5 [m] to 2642.5 [m], and **d**= 2640.5 [m] to 2641.5 [m]. The symbols within the image are presented according to the legend in figure **9**.

The JUT-01 Core Slab

As mentioned, the JUT-01 core slab covers a length of 18 meters, making it the longest core slab compared to WSP-01, BNV-01, and ERM-01. Relative to the other core slabs, the JUT-01 core slab also exhibits a greater variety of colors, ranging from brown beige to dark gray. The grain sorting distribution of the core slab varies from poorly sorted to well-sorted, while the grain size distribution fluctuates from claystones to medium-grained sandstones.

At the bottom of the JUT-01 core slab, from a depth of 3274.0 meters to 3272.0 meters, the rock is mainly characterized by cross-laminated medium-grained sandstones. Further down to 3265.0 meters depth, the rock predominantly features cross-laminated medium-grained sandstones, with intermittent cross-laminated coarse-grained siltstone beds. Subsequently, decreasing to 3263.0 meters depth, the rock is characterized by cross-laminated coarse-grained siltstone bed, alternating with cross-laminated fine-grained sandstones. These cross-laminated fine-grained sandstones continue down to 3259.0 meters depth, transitioning into medium-grained sandstones. For this depth, a 0.4-meter thick homogeneous claystone bed is found, sharply changing to massive medium-grained sandstones up to the top of the core slab at 3256.0 meters depth. The complete set of core interpretations for the JUT-01 core slab is presented in Figures **19**, **20**, **21** & **22**.

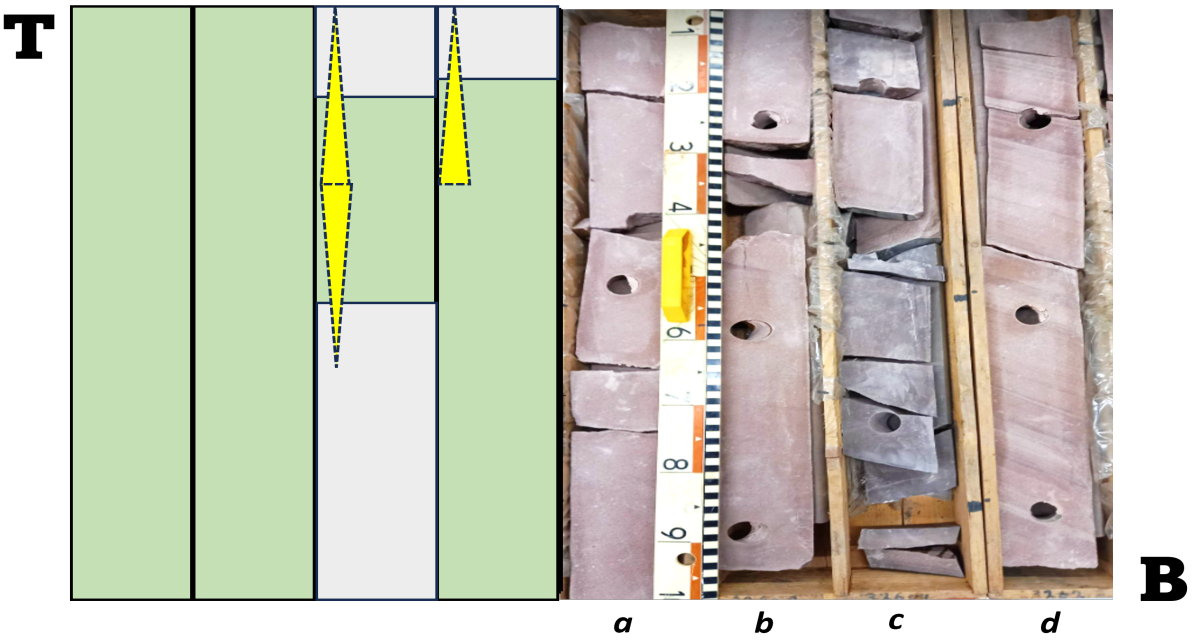

Figure 19: The letters denote the following depth intervals, from top to bottom along the JUT-01 core slab: **a**= 3257.8 $[m]$ to 3257.0 $[m]$, **b**= 3258.5 $[m]$ to 3257.8 $[m]$, **c**= 3259.3 $[m]$ to 3258.5 $[m]$, and **d**= 3260.0 $[m]$ to 3259.3 $[m]$. The symbols included within the image are defined according to the legend in figure **9**.

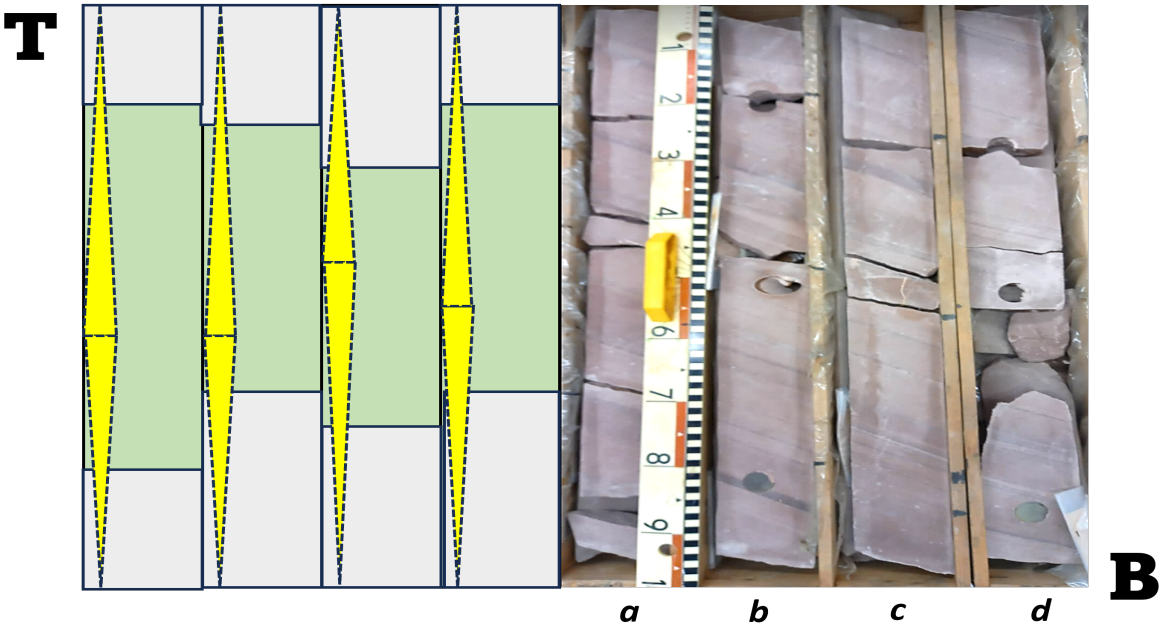

Figure 20: The letters denote the following depth intervals, from top to bottom along the JUT-01 core slab: **a**= 3260.8 [m] to 3260.0 [m], **b**= 3261.8 [m] to 3260.8 [m], **c**= 3262.4 [m] to 3261.8 [m], and **d**= 3262.4 [m] to 3263.2 [m]. The symbols within the image are presented according to the legend in figure **9**.

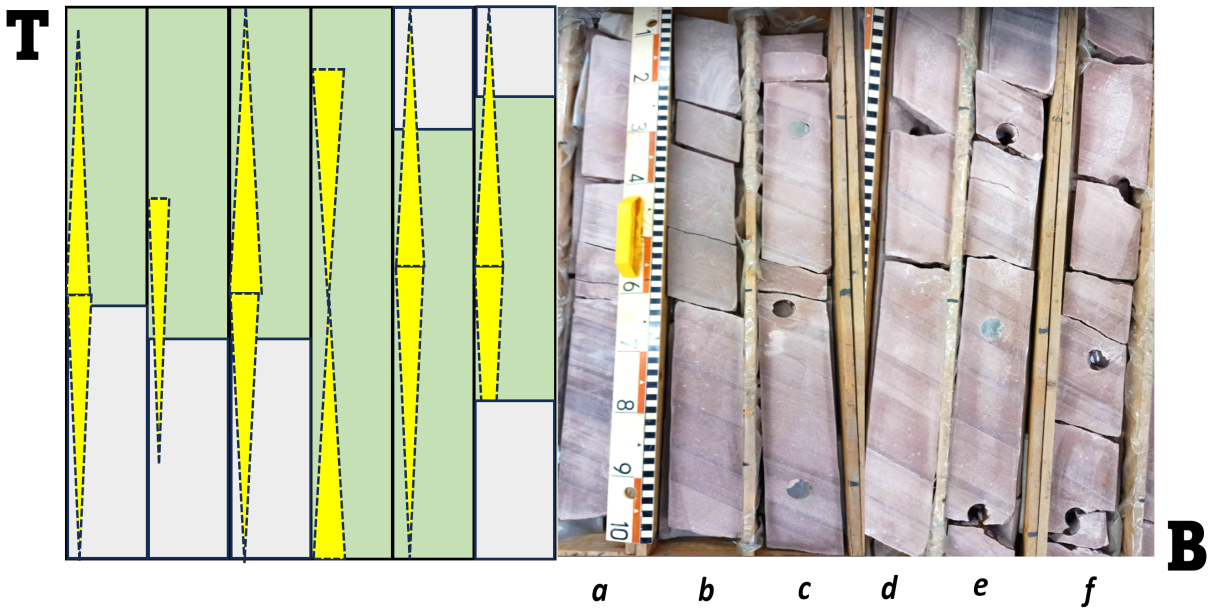

Figure 21: The letters denote the following depth intervals, from top to bottom along the JUT-01 core slab: **a**= 3264.0 [m] to 3263.2 [m], **b**= 3264.8 [m] to 3264.0 [m], **c**= 3265.6 [m] to 3264.8 [m], **d**= 3266.4 [m] to 3265.6 [m], **e**= 3267.2 [m] to 3266.4 [m], and **f**= 3268.0 [m] to 3267.2 [m]. The symbols included within the image are defined according to the legend in figure **9**.

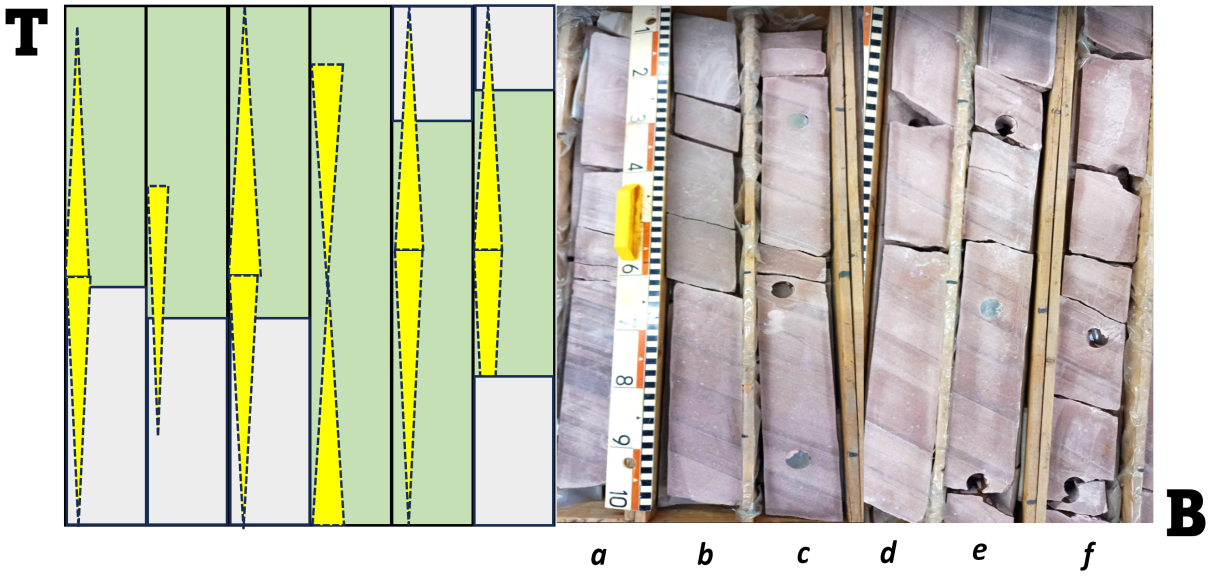

Figure 22: The letters denote the following depth intervals, from top to bottom along the JUT-01 core slab: **a**= 3269.0 $[m]$ to 3268.0 $[m]$, **b**= 3270.0 $[m]$ to 3269.0 $[m]$, **c**= 3271.2 $[m]$ to 3270.0 $[m]$, **d**= 3272.0 $[m]$ to 3271.2 $[m]$, **e**= 3273.1 $[m]$ to 3272.0 $[m]$, and **f**= 3274.0 $[m]$ to 3273.1 $[m]$. The symbols within the image are presented according to the legend in figure **9**.

2.3.3. Core Slab Facies Interpretations & Distributions

The descriptions of core slabs in the preceding subsection are utilized to designate lithofacies and subsequent facies groupings. Previously identified aeolian lithofacies and facies groupings from Priddy, C. L., & Clarke, S. M. (2021) **[33]** have been used for classification, as outlined in the corresponding tables (listed in Table **20** & **21** and presented in Appendix **A.3**).

The Lithofacies and Facies Classifications

To recognize and classify lithofacies and facies for the core slabs, the previously identified aeolian lithofacies and facies groupings from Priddy, C. L., & Clarke, S. M. (2021) **[33]** are included and listed in the corresponding tables (Appendix **A.4**). In addition to the information presented in these tables, the following facies descriptions are used for categorizing and classifying the different facies groupings:

- ***Aeolian Dune (AD):*** Encompasses lithofacies groups: flat-bedded cross-stratified sandstones (Smxb) and cross-laminated sandstones (Smtxb).
- ***Inter Dune (ID):*** Mainly consists of unstructured sandstones (Sm), parallel-laminated sandstones (Spl), and ripple-laminated sandstones (Sfrl).
- ***Sandy Sheet (SS):*** Comprises flat transverse sandstones (Smpb) and unstructured sandstones (Sm).
- ***Fluvial Channel (FC):*** Characterized by planar cross-bedded sandstones (Sxb), transverse cross-bedded sandstones (Stxb), and ripple cross-bedded sandstones (Srb).
- ***Sheet Flood (SF):*** Includes planar laminated sandstones (Spl), geosynclinal laminated sandstones (Smf), ripple cross-bedded sandstones (Sfrl), and conglomerate cross-bedded sandstones (Srb).

Based on the above categories, lithofacies and facies groupings have been classified for the core slabs of WSP-01, BNV-01, ERM-01, and JUT-01, as shown in the corresponding Tables (and presented in Appendix **D**).

The Core Slab Facies Distributions

As discussed earlier and outlined in the appendices, distributions for each core slab facies unit have been established and determined. The facies interpretation of the ERM-01 core slab has shown that it consists of 7.14%, of the sandy sheet facies unit and 92.86% of the sheet flood facies unit. In the case of the BNV-01 core slab, the facies distribution indicates 25% for the sheet flood facies unit, 40.62% for the aeolian dune facies unit, and 34.38% for the interdune facies unit. Similarly, for the WSP-01 core slab, the facies distribution indicates 30.4% for the aeolian dune facies unit, 33.4% for the interdune facies unit, and 36.2% for the sheet flood facies unit. The facies distribution for the JUT-01 core slab are 36.94% for the fluvial channel facies unit, 43.05% for the aeolian dune facies unit, 15% for the sandy sheet facies unit, and finally, 5.0% for the interdune facies unit.

In conclusion, for all core slabs, the following facies distribution is recognizable: 33.51% for the aeolian dune facies unit, 6.38% for the sandy sheet facies unit, 23.58% for the fluvial channel facies unit, 7.09% for the interdune facies unit, and finally, 29.43% for the sheet flood facies unit. The resulting facies distribution for all core slabs is depicted in the pie chart (Figure **23**). Additionally, according to the study by Priddy, C. L., & Clarke, S. M. (2021) **[33]**, the three facies groups—sandy sheet, aeolian dunes, and interdunes—correspond to an aeolian deposition environment, while the other two facies, fluvial channel and flood sheet, correspond to an ephemeral deposition environment. It was found that when the individual shares of facies units are summed up, 46.99% of the core slabs can be characterized by an aeolian deposition environment, and 53.01% of the core slabs are characterized by an ephemeral deposition environment.

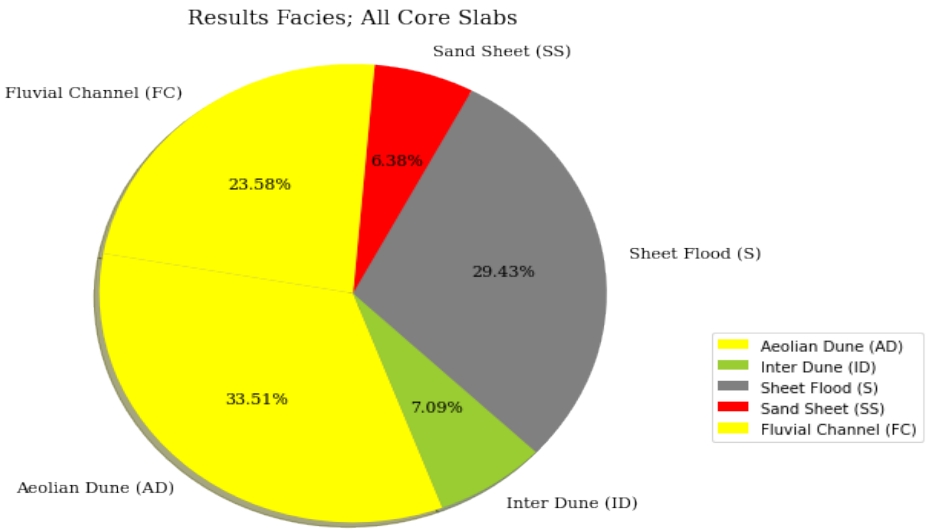

Figure 23: Pie chart: the facies unit proportions for the core slabs for boreholes JUT-01, WSP-01, ERM-01, and BNV-01.

2.3.4. The Paleo-current Orientations from the Core Slabs

As mentioned in the preceding section, the inclination (dip) angles of the cross-bedded sedimentary prints were measured for the core slabs (as shown in Figure **24**). Since there are no cross-bedded sedimentation prints present in the core slab of ERM-01, this core slab was excluded from this analysis.

The results from this analysis have shown that the cross-bedded sedimentary beds for the core slabs of WSP-01 and BNV-01 are predominantly oriented in the westward direction (270 [◦]). In contrast, for the core slab of JUT-01, it was found that the cross-bedded sedimentary beds are mainly oriented in the northwesterly direction (310 [◦]). These resulting findings are further discussed and elaborated in Chapter **3**.

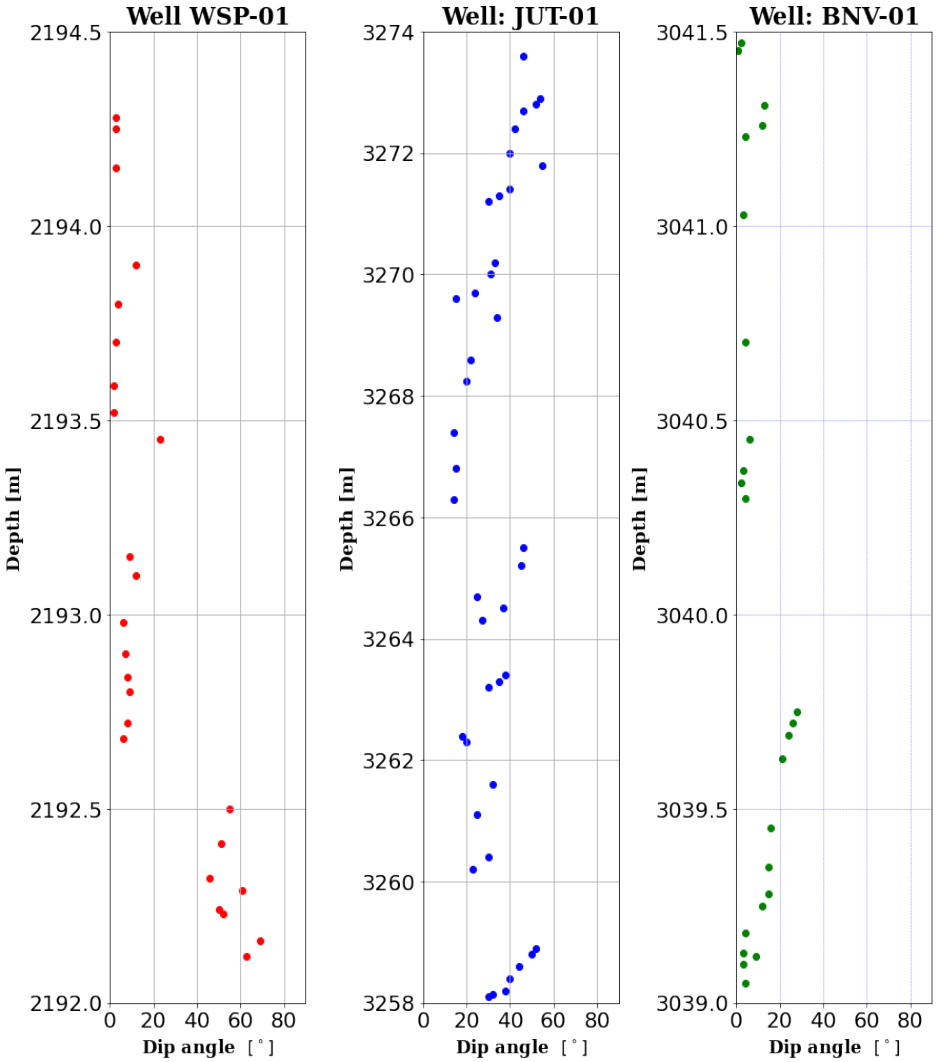

Figure 24: Coloured data points: the dip angles of the cross-bedded sedimentary layers for the core slabs of BNV-01, WSP-01 & JUT-01.

2.3.5. Discussion

The results from the preceding sections unveil both the facies units and their proportions in the Upper Slochteren Formation for the core slabs and the prevailing paleocurrent orientations during the Early Permian period. Although their facies units provide insights into the regional depositional environment and paleogeographic distribution, some discussion points arose during the analysis. These discussion points are listed and addressed below.

Due to the limited length of the total core slabs interpreted, there is uncertainty about whether the five different facies units classified represent all the facies units in the formation. Core slab analysis indicates the presence of ephemeral sediments alongside aeolian sediments in the study area, which demonstrates that the paleogeographic area did not consist entirely of aeolian sediments. Since core slabs also appear to be available for BLA-01, which could not be verified during writing this thesis, interpreting these core slabs could provide further insight into the potential presence of additional facies in the formation.

Because the facies groupings were primarily classified based on an individual study and were not validated against what other similar studies have shown, the performed facies classification for the core slabs in this thesis has limited reliability. Comparing core slab interpretations with facies classifications presented in other studies would decrease the uncertainty of the facies interpretations.

Assuming, based on sedimentary dip measurements from the JUT-01 core slab, that the paleo-orientation is related to the paleoflow orientation and not to the paleowind orientation, multiple sedimentary cross-bed measurements for future core slabs could support this evidence and provide more certainty about the orientation of paleoflow during the Early Permian.

2.3.6. Conclusions on the Geothermal Potential

As mentioned above, the core slab analysis reveals the facies units present in the Upper Slochteren Formation in the study area. Their sedimentary characteristics, such as grain sorting and grain size distributions interpreted from the core slabs, impact the geothermal potential of the formation. In this section, the effect of their properties on the geothermal potential of the formation is discussed and summarized in the following conclusion points.

From the core slab interpretations of BNV-01 and JUT-01, claystone beds with a thickness of up to 0.5 $[m]$ were identified. Due to these claystone beds, the vertical connectivity and, consequently, the vertical permeability of the reservoir formation are strongly influenced. Depending on both the lateral extent and vertical frequency of these claystone beds, this could have adverse consequences for reservoir properties and geothermal production.

Additionally, the core slab interpretations of WSP-01, BNV-01, and JUT-01 reveal that a significant portion of the sedimentary patterns found consists of cross-laminated sandstones or siltstones. Due to their morphological properties, the horizontal continuity, and thus the horizontal permeability of the formation are affected. This assumption implies that the overall horizontal flow could decrease and lead to a potential reduction in heat production in geothermal operations.

Finally, the core slab interpretation of ERM-01 indicates that the sediment is poorly sorted. This poorly sorted condition has a negative effect on both the vertical and horizontal permeability of the formation, which could result in poor or reduced geothermal output.

2.4. The Log Analysis

In order to evaluate the geothermal potential of the reservoir formation, reservoir properties such as porosity, permeability and net sand are analyzed based on well logs. A total of seven well bores are selected, for which their logs are analyzed. These boreholes were all drilled for hydrocarbon exploration within the research area during the past century.

Some of the boreholes were drilled by different drilling operators. As a consequence, not all sets of acquired logs were set equal for each of these wells. Therefore, not the same log analysis can be applied along each of these wells. Furthermore, no core plugs were retrieved or formation tests were performed along each of these wells.

This section describes both the log data and log methods used, to estimate the reservoir properties of the reservoir formation. The calculations were executed within Excel and then imported in Python, to visualize the results. The total workflow used to estimate the reservoir properties, such as volume of clay, porosity, and permeability is shown in Figure **25**.

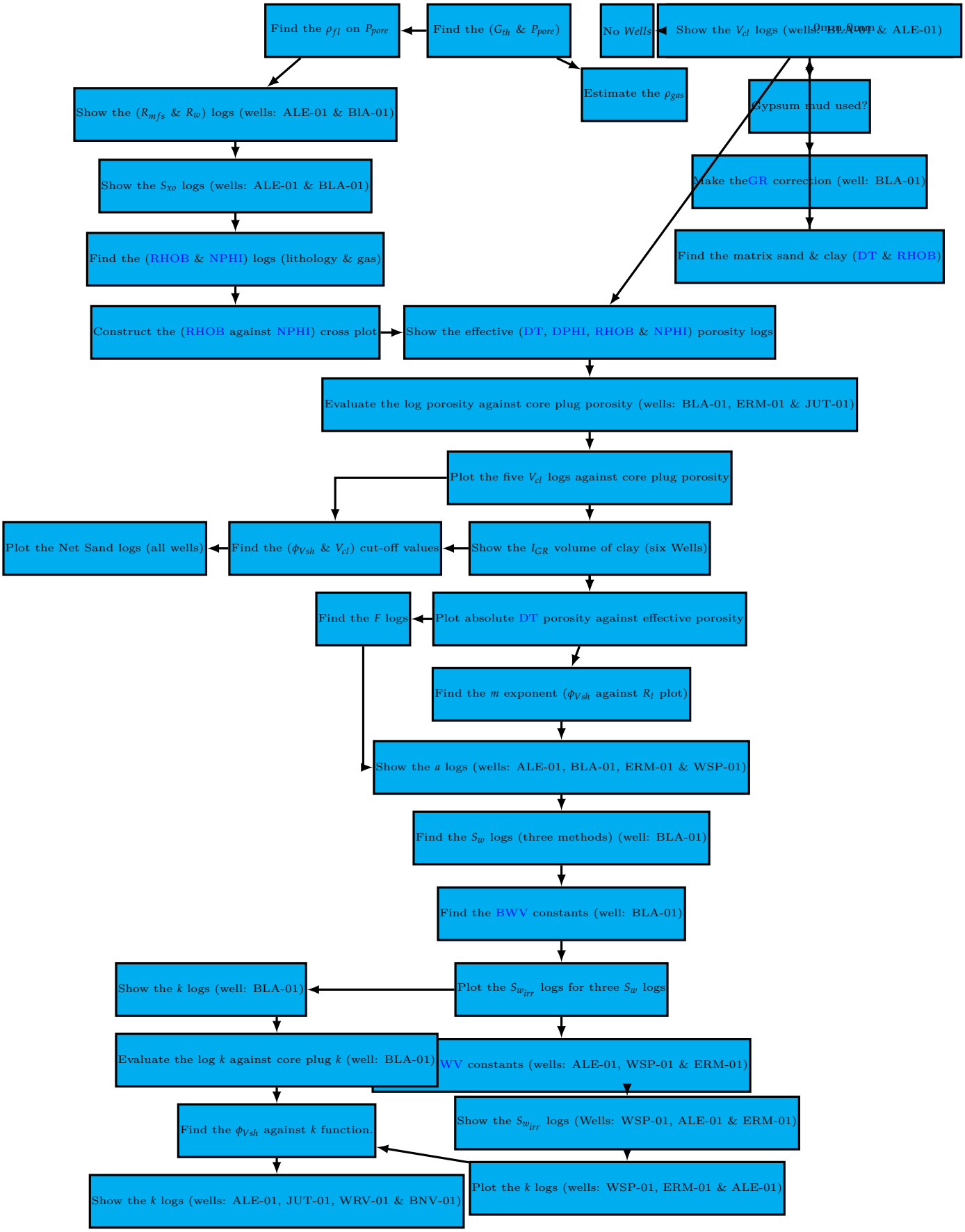

Figure 25: Work flow diagram as executed in Subsection **2.4**. Blue rectangles: Steps made to find or evaluate the reservoir property.

2.4.1. The Caliper Log Evaluation

To evaluate whether one of the boreholes is enlarged or narrowed along the reservoir formation, their diameters are determined by validating their caliper logs. Changes in borehole diameter can be introduced when excessive drilling mud is flushed into the formation (narrowed) or flushed out of the formation (enlargement) during the drilling operation.

The caliper logs were evaluated according to the criteria proposed by Zoback, M. D., et al. (1985). **[47]** & Bell, J.S. (1990) **[5]** The evaluation shows that none of the boreholes are enlarged or narrowed by more than 2 inch, such that the well logs are not significantly affected Zoback, M. D., et al. (1985). **[47]** & Bell, J.S. (1990) **[5]**. The caliper logs for these wells along the formation of the reservoir are presented in Appendix **A.5**.

2.4.2. The GR Log Correction

In the past century, drilling operators used in some occasions a potassium-rich composite in their drilling mud. This radioactive drilling composite influenced the acquired GR log of these wells. Looking at the well reports, the GR log of only one of the investigated boreholes (BLA-01) was found to contain a potassium-rich compound.

Therefore, it is important to correct that GR log for the additive response in radioactivity measured. To do so, the reference well ALE-01 was chosen, which is located closely to the corrected well BLA-01. Then, both the shale and the sand GR values were identified along each of the wells. In the end, a downscale correction factor GR, as presented in Table **5** was determined by using Equations **1** & **2**, to correct the original GR log along BLA-01. The GR logs along both the ALE-01 and BLA-01 wells are shown and presented in Figure **26**.

In Equations **1** and **2**, the following symbols are used: C_f correction downscaling factor, GR_{cor} corrected GR log in $[API]$, GR_{uncor} original GR log $[API]$, n the number of data points along the log, i the depth log point, $GR_{BLA,i}$ the GR log reader at depth for BLA-01 $[API]$, and $GR_{ALE,i}$ the GR log reader at depth for ALE-01 $[API]$.

$$\{C_f = \frac{(\sum_i^n \frac{1}{n} GR_{BLA,i} - \sum_i^n \frac{1}{n} GR_{ALE,i})}{\sum_i^n \frac{1}{n} GR_{BLA,i}} \tag{1}$$

$$\{GR_{cor} = GR_{uncor} * C_f \tag{2}$$

Table 5: GR log correction values for well BLA-01 as derived by comparison with ALE-01). NA: means the GR correction factor was not determined.

Well (code)	***Depth interval*** $[m]$	μ ***GR*** $[API]$	C_f $[-]$
BLA-01	1473.50 – 1503.50	167.82	0.58
BLA-01	1503.50 – 1542.50	54.53	0.62
ALE-01	1705.05 – 1735.05	70.56	NA
ALE-01	1735.05 – 1857.00	20.64	NA

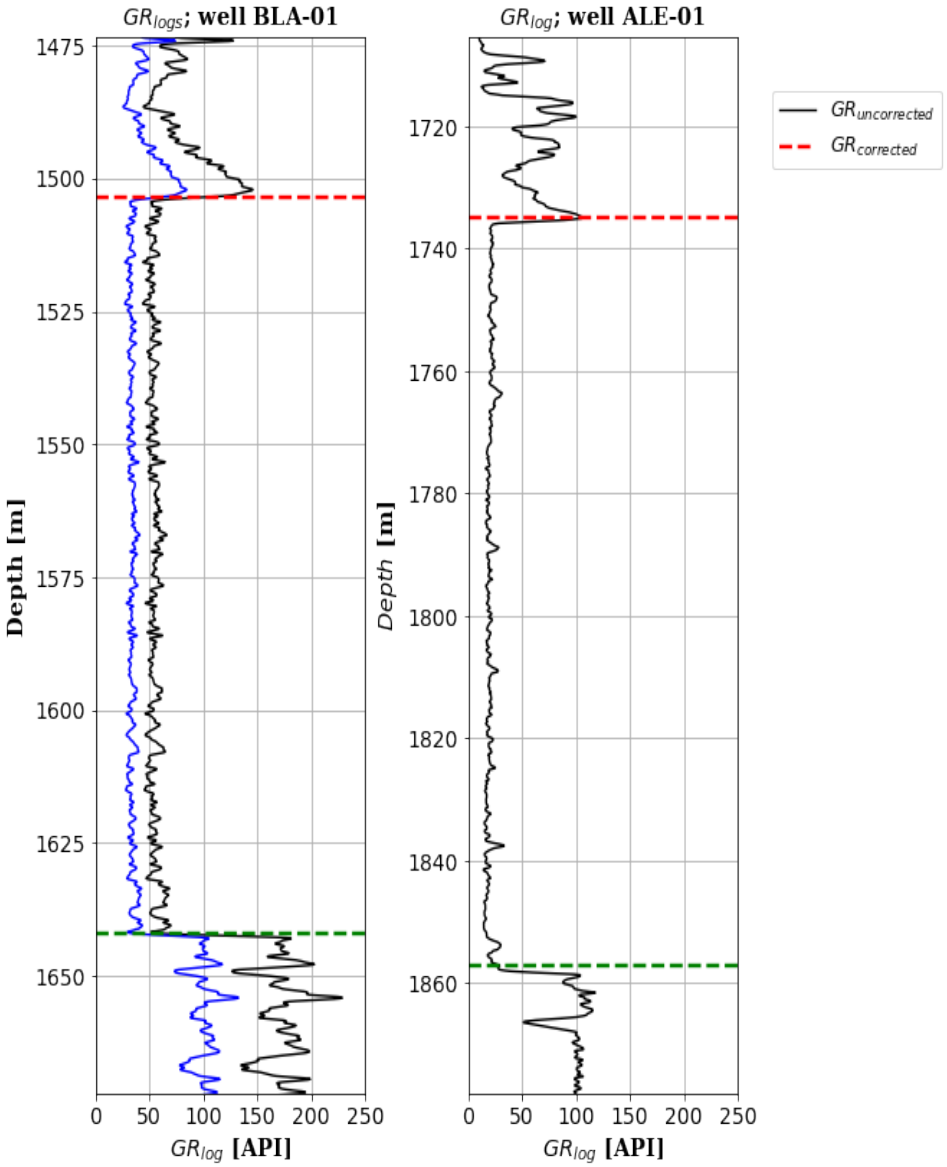

Figure 26: Left: original BLA-01 GR log (black curve), corrected BLA-01 GR log (blue curve), right: original ALE-01 GR log (black curve). Green dashed line: reservoir- to bottom rock boundary, and red dashed line: reservoir- to cap rock boundary.

2.4.3. The In-Situ P,V,T-conditions

To calculate the porosity of the reservoir formation, it is necessary to estimate the formation fluid density. This fluid formation density depends on and can be estimated based on both the reservoir pressure and temperature values.

The Geothermal Gradient

To estimate the reservoir formation temperature condition, the geothermal gradient is calculated. The regional geothermal gradient of 29.85 $[\frac{^\circ C}{km}]$ is estimated using Equation **3**, based on using a regional annual surface temperature and Bottom Hole Temperatures BHT. The regional annual surface temperature is determined based on data points from the Royal Netherlands Meteorological Institute (KNMI). Furthermore, the BHT data points are retrieved from the temperature database in NLOG. The geothermal gradient is estimated by plotting a line through the BHT data points (Figure **27**).

The symbols used in the equation are; $Z_{d,i}$ depth of temperature measurement in $[m]$, $T_{d,i}$ mud cake corrected temperature value in $[C^\circ]$, T_f the average surface temperature of 9.3 $[C^\circ]$, and G_{th} the geothermal gradient in $[\frac{C^\circ}{km}]$.

$$\{G_{th} = \frac{\sum_i^n \frac{1}{n}(T_{d,i} - T_f)}{\sum_i^n \frac{1}{n} Z_{d,i}} = 29.85 \qquad R^2 = 0.8937 \tag{3}$$

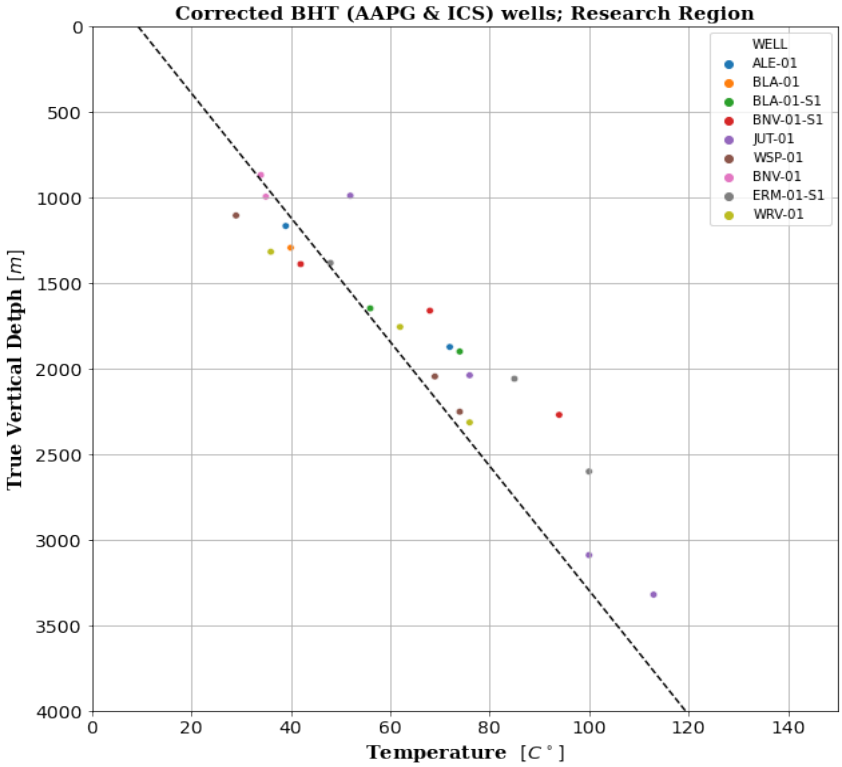

Figure 27: Colored dots: corrected BHT for wells with available BHT. Dashed black line; linear temperature with depth correlation.

The Pore Pressure Gradient

The pore pressure gradients of the formation along four wells were determined and are presented in Table **6** and shown in Figure **28**. The pore pressure gradients along these four wells are approximated based on hydro-static pressure data points, and taking the atmospheric pressure of 0.1 $[MPa]$ into consideration. The hydro-static-pressure points are retrieved from the Southern North Sea Basin SNS) pressure data base, which is available from the TNO website TNO.(2015) **[42]**. The linear correlation is calculated based on a linear correlation of the hydro-static pressure data points (Equation **4**). Lastly, the fluid densities of the formation along wells BLA-01 and ALE-01 were estimated using Equation **5** and are presented in Table **6**. The hydro-static pressure data-points for the four wells and their linear correlation are shown in Figure **28**.

In Equations **4** & **5** the following symbols are defined: Z represents the depth $[m]$, P_{pore} represents the pore pressure in $[MPa]$, a and b are the linear direction coefficient and slope $[-]$, ρ_{fl} denotes the formation fluid density $[\frac{g}{cm^3}]$, g represents the gravitational acceleration in $[\frac{m}{s^2}]$, Z_{avg} is the formation mid interval depth $[m]$, $P_{hydro,avg}$ denotes the average pore pressure $[MPa]$, $P_{hydro,T}$ is the pore pressure at formation top $[MPa]$, and $P_{hydro,B}$ is the pore pressure at formation bottom $[MPa]$

$$\{P_{pore} = \frac{(Z+b)}{a} = \frac{(Z+28.9068)}{97.8592} \qquad R^2 = 0.9884 \tag{4}$$

$$\{\rho_{fl} = \frac{P_{hydro,avg}}{(g \cdot Z_{\text{avg}})} = \frac{\frac{1}{2}\left(P_{hydro,T} + P_{hydro,B}\right)}{(g \cdot Z_{avg})} = \frac{\frac{1}{2}\left(\frac{Z_T+b}{a} + \frac{Z_B+b}{a}\right)}{(g \cdot Z_{avg})} = \frac{\frac{1}{2}\left(\frac{Z_T+2.891\cdot 10^1}{0.9785\cdot 10^1} + \frac{Z_B+2.891\cdot 10^1}{0.9785\cdot 10^1}\right)}{(g \cdot Z_{avg})} \tag{5}$$

Table 6: Formation fluid densities and pore pressures at their mid formation intervals. NA = not determined.

Well (code)	$\mu_{P_{pore}}$ $[Mpa]$	ρ_{fl} $[\frac{g}{cm^3}]$
BLA-01	16.37	1.0610
ALE-01	18.65	1.0580
$\mu_{\rho_{fl}}$	NA	1.0595

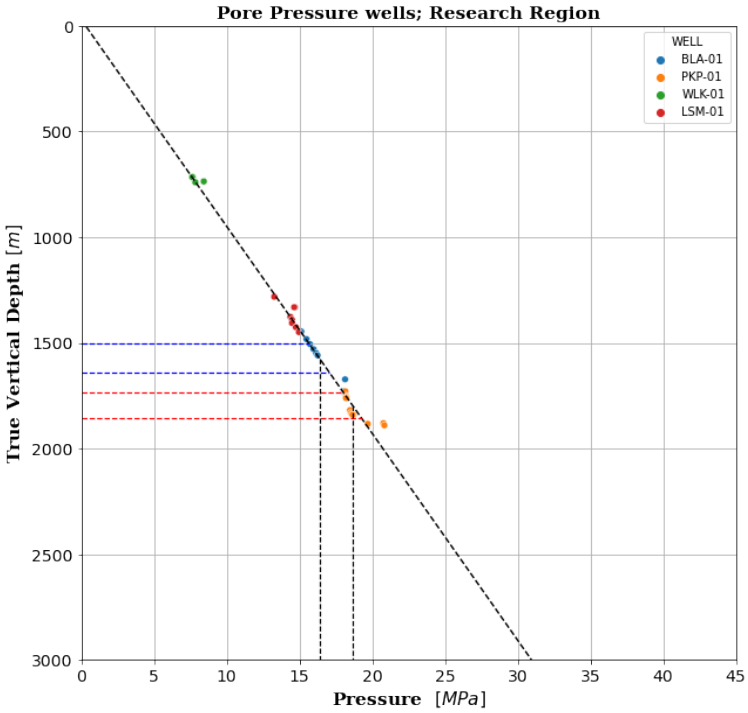

Figure 28: Colored dots: Hydro-static pressure data points along wells (BLA-01, PKP-01, WLK-01, and LSM-01), black dashed line: pore pressure correlation line, red dashed lines: top formation, blue dashed lines: bottom formation, and black dashed lines: average pore pressures.

2.4.4. The DT & RHOB Parameters

To estimate the formation porosity, constants for both the density and the sonic travel time are needed. Therefore, the density and the travel time values for both the fluid as well as the matrix within the rocks of the formation are approximated. The density and travel time of the rock matrix are calculated for both the sand and the dry clay.

The Sand Matrix & Pore Fluid DT & RHOB.

To estimate the constant density and travel time values for both the sand matrix and the pore fluid of the reservoir formation, the porosity core plug data points available for the boreholes BLA-01, ERM-01 and JUT-01 were retrieved from NLOG. The density RHOB log and the DT log for these wells are plotted against these core plug porosity data points. By plotting a linear line through the data points for the RHOB log readers and the DT log readers (Figure **29**), the constants for the fluid and the sand matrix of the density and the travel time of the reservoir formation were determined using the relations in equations **6** & **7**, and are listed in Table **7**.

In Equations **6** and **7**, the symbols used are: ρ_b bulk density log reader in $[\frac{g}{cm^3}]$, ΔT sonic time log reader in $[\frac{\mu s}{ft}]$, ϕ_{cp} core plug porosity retrieved from NLOG $[-]$, a for the linear coefficient $[-]$, and b the y-intercept $[-]$.

$$\{\rho_b = \frac{(\phi_{cp} + a)}{b} = \frac{(\phi_{cp} - 1.737)}{-0.644} \qquad R^2 = 0.533 \tag{6}$$

$$\{\Delta T = \frac{(\phi_{cp} + a)}{b} = \frac{(\phi_{cp} + 0.389)}{7.15 \cdot 10^{-03}} \qquad R^2 = 0.799 \tag{7}$$

Table 7: Sand matrix RHOB & DT and pore fluid RHOB & DT values. NA = the value is not defined.* means the value was estimated based on a correlation (as presented in Appendix **A.6**).

Component	ρ_{log} $[\frac{g}{cm^3}]$	DT_{log} $[\frac{\mu s}{ft}]$
Matrix	2.698	54.467
Fluid	NA	124.361*

The Dry Clay Matrix DT & RHOB Parameters

To estimate the RHOB and the DT values of the dry clay in the matrix of the rocks of the reservoir formation, core plug porosity data points along the Upper Röt Claystone and the Solling Claystone formations of the borehole JUT-01 were retrieved from blueNLOG. The RHOB log and the DT logs along this well are plotted against the core plug porosity data points and are shown in Figure **29**. The linear correlation line is plotted against the data points for the RHOB log as well as the DT log, calculated using the relations in Equations **8** & **9** respectively. Based on these linear correlation lines the dry clay matrix values for the RHOB and the DT were determined and are listed in Table **8**.

In Equations **8** and **9** the following symbols are used: ΔT_{sh} wet clay DT in $[\frac{\mu s}{ft}]$, ρ_{sh} wet clay RHOB in $[\frac{g}{cm^3}]$, ϕ_{cp} core plug porosity $[-]$, a direction coefficient $[-]$, and b slope factor $[-]$.

$$\{\rho_{sh} = \frac{(\phi_{cp} + a)}{b} = \frac{(\phi_{cp} - 0.438)}{-0.149} \qquad R^2 = 0.209 \tag{8}$$

$$\{\Delta T_{sh} = \frac{(\phi_{cp} + a)}{b} = \frac{(\phi_{cp} - 0.0716)}{-6.99 \cdot 10^{-04}} \qquad R^2 = 0.201 \tag{9}$$

Table 8: Dry clay matrix RHOB & DT values

Parameter	*Value*
DT_{log} $[\frac{\mu s}{ft}]$	102.328
ρ_{log} $[\frac{g}{cm^3}]$	2.946

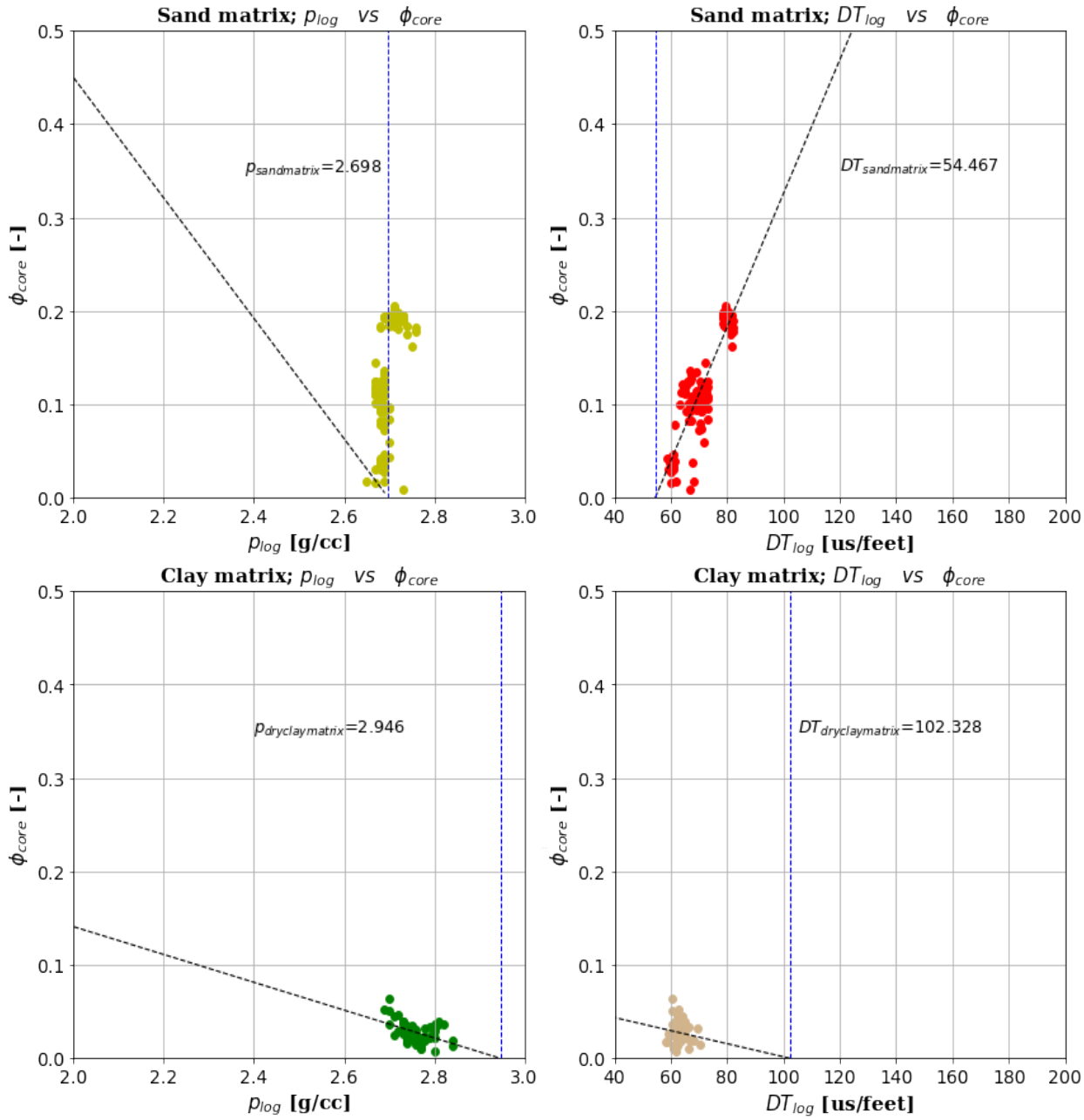

Figure 29: Top left: Cross-plot of ϕ_{core} versus ρ_{log} for the formation (sand matrix), top right: Cross-plot of ϕ_{core} versus DT_{log} for the formation (sand matrix), bottom left: Cross-plot of ϕ_{core} versus ρ_{log} for the dry clay matrix of the Triassic, and bottom right: Cross-plot of ϕ_{core} versus DT_{log} for the dry clay matrix of the Triassic

2.4.5. The Near Wellbore Zonation

If there is gas present within the reservoir formation, the porosity calculations need a correction. The presence of gas in the formation is determined and the logs that are affected by this gas are corrected. The amount of gas along the wells is estimated based on the flushed zone saturation.

In this subsection, first, the flushed zone gas saturation is determined and second, the density of the gas is determined.

The Saturation of the Flushed zone

To estimate the flushed zone gas saturation, the flushed zone water saturation is determined. To estimate the flushed zone water saturation along the well-bores of the formation, both the drilling mud resistivity log as well as the water resistivity log for boreholes ALE-01 and BLA-01 were calculated.

To estimate the drilling mud resistivity log along the two boreholes, the surface mud resistivity values for each of these wells were determined. The surface resistivity values were taken from the well reports, which are available on NLOG and are presented in Table **9**. The relation of Arps, J. J. (1953) **[2]** is used to convert the surface drilling mud resistivity values to formation drilling mud resistivity values.

To estimate the water resistivity logs along the two wells, ionic concentrations reported for water samples were retrieved from NLOG and are used to determine the summed ionic conductivity of the formation. The ionic concentrations obtained from each sample are multiplied to their ionic weight multiplier, as presented in Equation **10**. The resulting NaCl summed ionic conductivity is then converted by the correlation as shown in Equation **10** as attained from Catinat, M., et al. (2023) **[13]**, to their surface resistivity values. Based on the ionic concentration values as retrieved from the reports, the corresponding average surface resistivity along both wells are estimated and listed in Table **10**.

In Equation **10** the symbol is defined as: $R_{w75,w}$ is the brine resistivity in $[\Omega * m]$, M_α is the individual weighted ionic multiplier in $[\frac{S \cdot m^2}{mol}]$, $C_{\alpha \cdot i}$ is the concentration of the specific ion in the solution of the water sample in $[\frac{mol}{L}]$, and C_{sum} is the summed ionic conductivity in $[\frac{S}{m}]$.

$$C_{sum} = \sum_{\alpha=1}^{n} M_\alpha \cdot C_{\alpha \cdot i} \quad if R_{w75,w} = \frac{1}{C} \longrightarrow R_{w75,w} = (2.74 \times 10^{-4} C_{sum})^{-1} + 0.0123 \qquad (10)$$

To determine the flushed zone water saturation logs along these wells, the resistivity ratio formula is used (Equations **11** & **12**), retrieved from Gonzalez, O. (2012) **[19]**. Lastly, the surface salinity values were converted as well with Arps, J. J. (1953) **[2]** relation, as presented within Equation **13** to water resistivity logs of the formation reservoir.

In Equations **11** and **12** symbols used are as follows: S_{xo} flushed zone mud filtrate saturation $[-]$, R_t uninvaded zone resistivity from the Induction Deep (ILD) log or the Laterlog Deep (LLD) log (as listed in Table **4**) in $[\Omega \cdot m]$, R_{xo} flushed zone mud filtrate resistivity as measured by the Micro Spherically Focused (MSFL) log $[\Omega \cdot m]$, R_w resistivity of formation brine in the uninvated zone $[\Omega \cdot m]$, R_{mf} resistivity of the mud filtrate $[\Omega \cdot m]$,

$$S_{xo} = \left[\frac{\frac{R_{xo}}{R_t}}{\frac{R_{mf}}{R_w}} \right]^{[\alpha^{def}]} \tag{11}$$

Where for α^{def} holds:

$$\alpha^{def} = \frac{1}{n(1-\beta)} = \frac{5}{8} \quad \longrightarrow \beta = 0.2 \tag{12}$$

where n is the saturation exponent set to be 2 $[-]$.

In Equation **13**, the symbols used are; $R_{mf,wi}$ mud filtrate resistivity at formation temperature $[\Omega \cdot m]$, $R_{mfs,w}$ mud resistivity at surface conditions $[\Omega \cdot m]$, $T_{1,w}$ surface completion mud temperature $[C^\circ]$, $R_{wT2,w}$ brine resistivity at formation temperature $[\Omega \cdot m]$, $R_{w75,w}$ brine resistivity at 24 $[C^\circ]$ in $[\Omega \cdot m]$, and $T_{2,iw}$ formation temperature based on the geothermal gradient of 29.85 $\frac{C^\circ}{km}$.

$$R_{mf,wi} = R_{mfs,w}\left(\frac{T_{1,w} + 6.77}{T_{2,iw} + 6.77}\right) \qquad R_{wT2,w} = R_{w75,w}\left(\frac{81.77}{T_{2,iw} + 6.77}\right) \tag{13}$$

Table 9: Completion mud density and resistivity values at surface condition. NA means no value was estimated. * means averaged value along (ALE-01 & BLA-01).

Well (code)	ρ_{mud} $[\frac{g}{cc}]$	R_{mud} $[\Omega \cdot m]$	T_{surf} $[C^\circ]$
BLA-01	1.26	0.073	35
ALE-01	0.95	0.100	24
μ	1.105*	NA	NA

Table 10: Surface water resistivity values at surface condition (as funtion of temperature)

Well (code)	T_{surf} $[F^\circ]$	$R_{water,surface}$ $[\Omega \cdot m]$
ALE-01	75.2	$6.443 \cdot 10^{-2}$
BLA-01	71.6	$4.271 \cdot 10^{-2}$

The Density of the Gas Mixture

To calculate the porosity of the formation, both the Neutron Porosity NPHI log and the RHOB log need to be corrected for the presence of gas. For this purpose, the density of the gas in the reservoir formation needs to be estimated. To estimate the gas density of the gas within the formation of the reservoir, the average molar composition of the gas 84.3% CH_4, 14.4% C_2H_8, 0.5% CO_2, & 0.8% N_2 is used as retrieved from Kay, W. (1936) **[21]** The gas gravity is estimated based on this gas composition with the relation presented in Equation **14** as retrieved from Kay, W. (1936) **[21]**. Together with the average formation reservoir temperature and pressure along the BLA-01 and ALE-01 wells (Table **6**), the gas density of 0.197 $[\frac{g}{cm^3}]$ was approximated using gas correlation charts as shown in Appendix **A.6**.

In Equation **14**, the symbols used are: γ_i the partial molecular factor for molar component i $[-]$, $M_{w,i}$ the molecular mass for molar component i $[\frac{g}{mol}]$, G the estimated gas weight $[\frac{g}{mol}]$, and n the number of molecular components $[-]$.

$$G = \frac{\sum_i^n \gamma_i \cdot M_{w,i}}{29.00} \tag{14}$$

2.4.6. The Volume of Clay Calibration

To approximate the right volume of clay distribution within the formation of the reservoir, various volumes of clay logs along the combined wells ALE-01 and BLA-01 were validated against a range of clay cut-off values, as shown in Subsection **2.4.12**. The nonlinear volume of clay method from Clavier, et al. (1971) **[12]** shows to have the most suitable approximation of the volume of clay distribution of the reservoir formation. The linear volume of clay method as described by Bush, R. E., & Mardock, E. S. (1951) [10] and calculated by equation **15**, overestimates the volume of clay of the reservoir formation. The other nonlinear volume of clay methods such as Larionov, V.V. (1969) **[25]**, Larionov Paleozoic rocks (1969) **[25]**, and Stieber, S. J. (1970) **[37]** as retrieved from Gonzalez, O. (2012) **[19]**. all wrongly estimate the volume of clay content of the formation. The final volume of clay distributions along the wells with an available GR log are estimated and are presented in Figure **39** (subsection **2.4.12**).

In the Old Rock Equation **15**, the following symbols are used: I_{GR} the Linear GR Index, GR_{cor} the corrected GR log (as presented in Subsection **2.4.2**) $[API]$, GR_{min} the minimum GR value, i.e., pure sandstone estimated to be 132.51 $[API]$, and GR_{max} the maximum, or pure shale GR value estimated to be 9.51 $[API]$.

$$\{I_{GR} = \frac{(GR_{cor} - GR_{min})}{(GR_{max} - GR_{min})} \tag{15}$$

2.4.7. The Gas & Lithology NPHI & RHOB log Corrections

To estimate correct porosity values for reservoir formation, it is important to first correct the DRHO log and the NPHI log for the presence of gas and clay within the reservoir formation. This subsection first describes the corrections made for the DRHO log and hereafter the corrections made for the NPHI log.

The RHOB log Corrections

Along most of the wells a log is available on NLOG to estimate the porosity of reservoir formation. It is needed to correct the log readers for the presence of clay and gas within the reservoir formation. To do so, the density log readers are first corrected for the presence of clay in the formation. This is done by using the relationship presented in Equation **16** as retrieved from Peters, E. J. (2012) **[31]**. When the density log readers have been corrected for the presence of clay, they are corrected for the presence of gas within the formation. For this purpose, the chart from Tittman, J., & Wahl, J. S. (1965) **[39]** was used to determine the gas density correction factor, to correct the density log readers for the presence of formation gas. The chart is presented in Appendix **A.6** and the density gas correction factors as determined along wells ALE-01 and BLA-01 are listed in Table **11**.

In Equation **16** the following symbols are used: ρ_{bc} the shale-corrected RHOB log $[\frac{g}{cm^3}]$, ρ_b the RHOB log reader $[\frac{g}{cm^3}]$, ρ_{ma} the density of the sand matrix $[\frac{g}{cm^3}]$ (as listed in Table **7** in Subsection **2.4.4**), ρ_{sh} the density of the dry shale $[\frac{g}{cm^3}]$ (as listed in Table **8**), and V_{sh} the Clavier, et al. (1971) **[12]**based volume of clay distribution $[-]$.

$$\{\rho_{bc} = \rho_b + V_{sh}(\rho_{ma} - \rho_{sh}) \tag{16}$$

Table 11: Apparent density correction values along boreholes (ALE-01 & BLA-01). NA: not applicable; * value utilized to correct the RHOB logs for the remaining wells.

Borehole	*BLA-01*	*ALE-01*
ρ_b - ρ_{log}	0.09	0.055
$\Delta\mu$	0.0725*	NA

The NPHI log Corrections

Since the formation consists primarily of sandstones, and the NPHI log is calibrated with respect to limestones, the NPHI log readers are corrected for sandstone, by usage of the relation retrieved from Glover, P. (2024) **[18]** and presented in Equation **17**. Hereafter, the log readers are corrected for the presence of formation gas in the reservoir, for which the relation from Peters, E. J. (2012) **[31]** is used, which is presented in Equations **18** and **19**. In the calculations, the Hydrogen Index HI of the drilling mud is set equal to that of oil, as the well reports from ALE-01 and BLA-01 both showed that the drilling mud used was oil-based.

In Equations **17**, **18** & **19**, the following symbols are defined: ρ_{ma} the density of the matrix sandstone $[\frac{g}{cm^3}]$ (as retrieved from Table **7**), $\rho_{ma,l}$ the density of the limestone matrix of 2.71 $[\frac{g}{cm^3}]$ as retrieved from Berger, D. L. (1992) **[6]**, ϕ_N the original NPHI log $[-]$, HI_{mf} the mud filtrate HI of 1.003 $[-]$ (as retrieved from Glover, P. (2024) **[18]**)), HI_{HC} is the HI of oil set as 1.000 $[-]$ (as retrieved from Glover, P. (2024) **[18]**), ρ_{gas} the density of the gas mixture $[\frac{g}{cm^3}]$ (as discussed in Subsection **2.4.5**), S_{xo} the approximated flushed zone mud saturation $[-]$ (as described in Subsection **2.4.5**), $\phi_{N_{lithology}}$ the sandstone corrected NPHI log $[-]$, and $\phi_{N_{gaslithology}}$ the gas and sandstone corrected NPHI log $[-]$.

$$\phi_{N;lithology} = \phi_N \cdot \frac{\rho_{ma}}{\rho_{ma,l}} \tag{17}$$

$$\phi_{N;gas\&lithology} = \phi_{N;lithology} \cdot (HI_{mf} \cdot S_{xo} + (HI_{hc} \cdot (1 - S_{xo}))) \tag{18}$$

If $HI_{hc} = 2.25 * \rho_{gas}$, then Equation **18** converts into Equation **19**:

$$\phi_{N;gas\&lithology} = \phi_{N;lithology} \cdot (HI_{mf} \cdot S_{xo} + ((2.25 * \rho_{gas}) \cdot (1 - S_{xo}))) \tag{19}$$

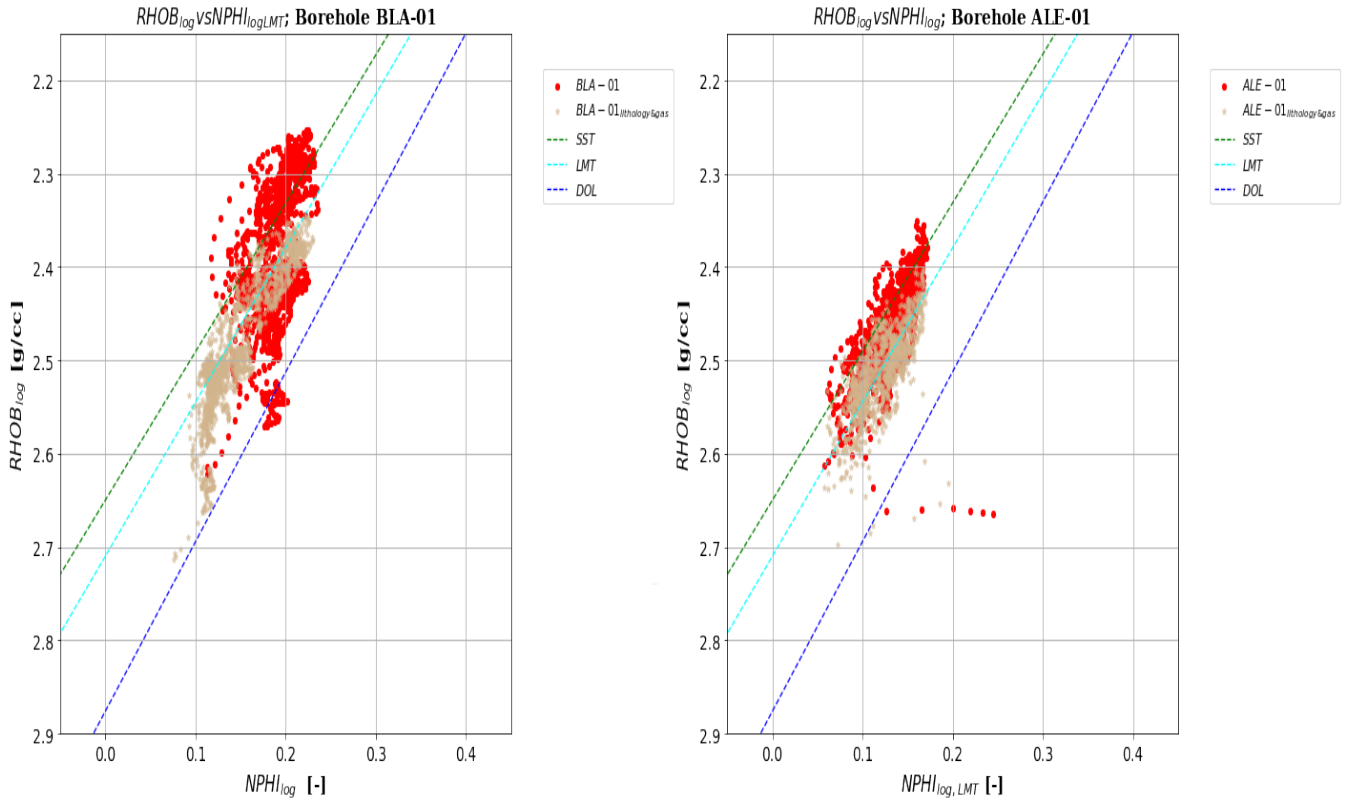

Figure 30: Left; the formations RHOB against NPHI cross plot along borehole BLA-01, right; the formations RHOB against NPHI cross plot along borehole ALE-01. Red data points: original logs; brown data points: lithology and gas corrected logs; dotted lines; Sandstone line (SST), Limestone line (LST), and Dolomite Line (DOL).

2.4.8. Log Porosity Validations

To estimate the effective porosity along the wells in this work, several porosity logs are validated against core plug porosity data points.

This subsection, first describes the porosity log against the core plug data points, to validate the best porosity log. Hereafter, the best porosity log is varied based on various volume of clay logs, to validate which volume of clay log gives the best effective porosity log. Lastly, the absolute porosity against effective porosity correlation is approximated, to estimate the effective porosity logs along the wells, for which only absolute porosity was calculated.

The Log against Core Plug Porosity Validation

To choose which porosity log best fits the core plug porosity data points retrieved from NLOG, the porosity logs from the various porosity methods used, (as described in Appendix **A.9**) along the wells BLA-01, JUT-01 and ERM-01 are validated against their acquired core plug porosity data points. To validate these core plug porosity data points, they were adjusted for the effect of core plug volume increase with a reduction factor of 0.95, which was retrieved from Nieto, A.J., et al. (n.d.) **[30]**). The porosity logs along these wells against their corrected core plug data points are presented in Figure **31**.

To evaluate which porosity log gives the best fit, the porosity logs are validated against their core plug data points by determining their Sum of Squared Residuals SSR using Equation **20**, retrieved from Baker, O. R, et al.(2015) **[3]**). The porosity log with the lowest SSR of 2.87 $\cdot 10^{-01}$ (Table **12**) is the NPHI log followed by the DT log with a SSR value of 3.64 $\cdot 10^{-01}$). Since the DT porosity log is estimated along all the three wells, and the NPHI porosity log is only estimated along the well BLA-01, the DT porosity logs are selected for further analysis as described in the proceeding Sub-subsections.

In Equation **20**, the following symbols are used: SSR the SSR value $[-]$, ϕ_{avg} the average effective (DT-, DPHI-, NPHI, or RHOB) log porosity $[-]$, $\phi_{cp,i}$ the surface corrected core plug porosity data point $[-]$, n the number of core plug porosity data points $[-]$, and i the core plug porosity data point $[-]$.

$$SSR = \sum_{i}^{n} (\phi_{avg} - \phi_{cp,i})^2 \tag{20}$$

Table 12: Below the resulting SSR and the porosity means along boreholes (BLA-01, ERM-01 & JUT-01) for the effective DT porosity, RHOB porosity, DPHI porosity, and NPHI porosity log distributions. NA: means the log wasn't estimated (as identified in Table **4**).

Well	***BLA-01***	***ERM-01***	***JUT-01***	*mean* $[SSR]$
ϕ_{DT} $[mean]$	$2.03 \cdot 10^{-01}$	$\cdot 10^{-02}$	$1.07 \cdot 10^{-01}$	NA
ϕ_{RHOB} $[mean]$	$9.81 \cdot 10^{-02}$	$\cdot 10^{-02}$	$7.44 \cdot 10^{-02}$	NA
$\phi_{e,DPHI}$ $[mean]$	$2.15 \cdot 10^{-01}$	NA	NA	NA
$\phi_{e,NPHI}$ $[mean]$	$1.66 \cdot 10^{-01}$	NA	NA	NA
ϕ_{DT} $[SSR]$	$6.33 \cdot 10^{-01}$	$6.29 \cdot 10^{-02}$	$3.96 \cdot 10^{-01}$	$3.64 \cdot 10^{-01}$
ϕ_{RHOB} $[SSR]$	$8.84 \cdot 10^{-00}$	$5.55 \cdot 10^{-02}$	$1.82 \cdot 10^{-00}$	$3.57 \cdot 10^{-00}$
$\phi_{e,DPHI}$ $[SSR]$	$1.51 \cdot 10^{-00}$	NA	NA	$1.51 \cdot 10^{-00}$
$\phi_{e,NPHI}$ $[SSR]$	$2.87 \cdot 10^{-01}$	NA	NA	$2.87 \cdot 10^{-01}$

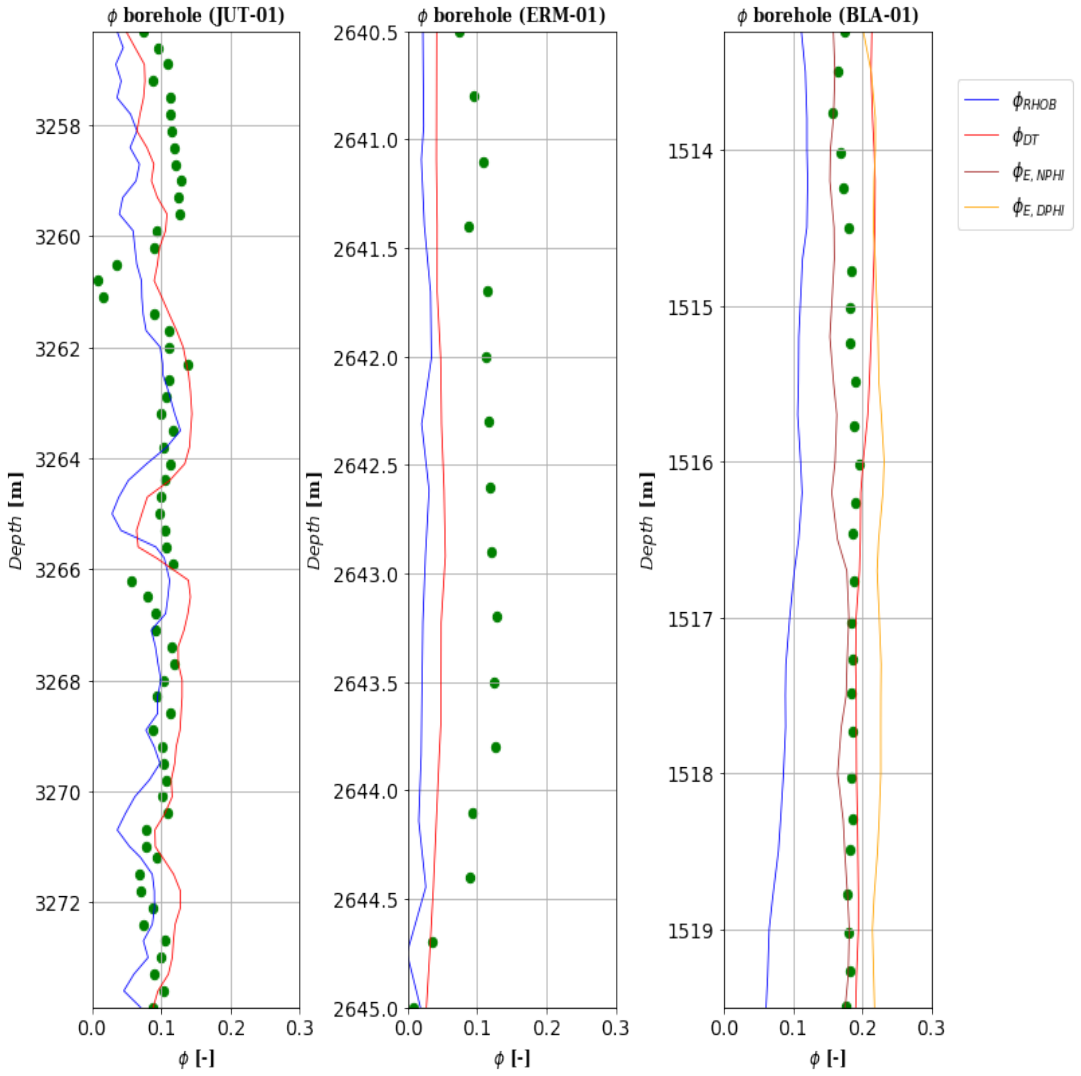

Figure 31: Green points: The retrieved core plug porosity data points. Coloured curves: the estimated effective porosity distributions (as discussed in Appendix **A.4**). Applicable to the core plug intervals along boreholes (JUT-01, ERM-01 & BLA-01).

The Volume of Clay Method Validation

In the previous Sub-subsection it was shown that the DT log porosity gives the overall best fit of the effective porosity log with core plug porosity data points along wells BLA-01, JUT-01 and ERM-01. To validate this result, effective DT porosity logs were computed with five different methods: Clavier Clavier, et al. (1971) **[12]**, Stieber, S. J. (1970) **[37]**, Larionov Paleozoic Rocks **[25]**, Larionov Tertiary Rocks (1969) **[25]** and the linear GR index defined as I_{GR}. These logs were then validated against their core plug porosity data points along these wells, as shown in Figure **32**. The SSR values are estimated for each of these five effective porosity logs, and are listed in Table **13**. The lowest SSR value of 2.28 $\cdot 10^{-01}$ is estimated for the DT effective porosity computed based on the I_{GR} volume of clay log. Therefore, the DT method in combination with the I_{GR} volume of clay method is shown to give the best effective porosity fit with core plug porosity data points. For the remaining wells WSP-01 and ALE-01, for which both a GR log and a DT log are available, the effective porosity logs were calculated.

Table 13: Computed SSR and their mean values along boreholes (BLA-01, ERM-01 & JUT-01) for the effective DT porosity as function of volume of shale distribution.

Well	***BLA-01***	***ERM-01***	***JUT-01***	*mean [SSR]*
$\phi_{DT(CLAVIER)}$ $[mean]$	$2.03 \cdot 10^{-01}$	$4.36 \cdot 10^{-02}$	$1.08 \cdot 10^{-01}$	
$\phi_{DT(STIEBER)}$ $[mean]$	$1.96 \cdot 10^{-01}$	$3.63 \cdot 10^{-02}$	$1.18 \cdot 10^{-01}$	
$\phi_{DT(LARIONOVN)}$ $[mean]$	$1.90 \cdot 10^{-01}$	$4.25 \cdot 10^{-02}$	$1.16 \cdot 10^{-01}$	
$\phi_{DT(LARIONOVO)}$ $[mean]$	$2.00 \cdot 10^{-01}$	$4.58 \cdot 10^{-02}$	$1.07 \cdot 10^{-01}$	
$\phi_{DT(IGR)}$ $[mean]$	$1.72 \cdot 10^{-01}$	$3.58 \cdot 10^{-02}$	$1.08 \cdot 10^{-01}$	
$\phi_{DT(CLAVIER)}$ $[SSR]$	$6.69 \cdot 10^{-01}$	$6.85 \cdot 10^{-02}$	$4.77 \cdot 10^{-01}$	$4.05 \cdot 10^{-01}$
$\phi_{DT(STIEBER)}$ $[SSR]$	$3.05 \cdot 10^{-01}$	$7.71 \cdot 10^{-03}$	$1.76 \cdot 10^{-00}$	$6.91 \cdot 10^{-01}$
$\phi_{DT(LARIONOVN)}$ $[SSR]$	$1.03 \cdot 10^{-01}$	$5.59 \cdot 10^{-02}$	$1.48 \cdot 10^{-00}$	$5.47 \cdot 10^{-01}$
$\phi_{DT(LARIONOVO)}$ $[SSR]$	$4.72 \cdot 10^{-01}$	$9.99 \cdot 10^{-02}$	$1.58 \cdot 10^{-00}$	$7.16 \cdot 10^{-01}$
$\phi_{DT(IGR)}$ $[SSR]$	$8.68 \cdot 10^{-02}$	$5.87 \cdot 10^{-03}$	$5.90 \cdot 10^{-01}$	$2.28 \cdot 10^{-01}$

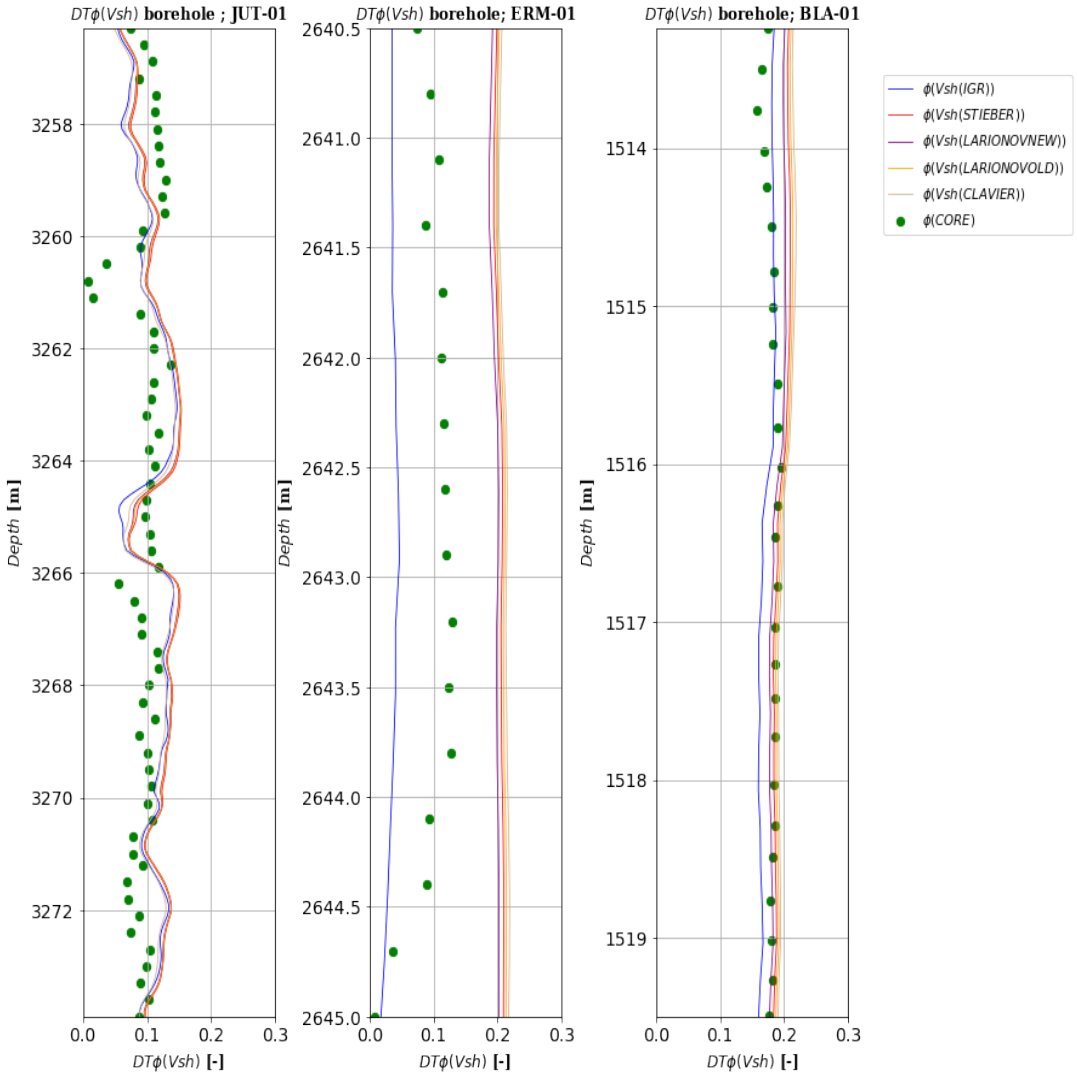

Figure 32: Green points: the retrieved core plug porosity data points; coloured curves: the effective DT porosity distributions as function of the five volume of clay methods. The illustration is applicable to the core plug intervals for boreholes JUT-01, ERM-01 & BLA-01.

2.4.9. The effective DT against absolute DT Porosity Correlation

There is no available DT porosity log for well WRV-01 and JUT-01 in NLOG and for well BNV-01 there is no GR log available to compute the effective porosity log. Therefore, along the other wells BLA-01, ALE-01, ERM-01 and WSP-01 their effective DT porosity logs were plotted against their absolute DT porosity logs, as shown in Figure **33**. Based on a linear regression line through their data points, a linear relationship was determined and presented in Equation **21**. This linear correlation was used to convert the absolute DT porosity logs along wells BNV-01, JUT-01 and WRV-01 to effective DT porosity logs.

In Equation **21**, the following symbols are used: $DT\phi_{gas,sh}$ the gas and shale corrected DT porosity $[-]$, $DT\phi$ the uncorrected (gas & shale) DT porosity $[-]$, a the slope coefficient $[-]$, and b the y-intercept $[-]$.

$$DT\phi_{gas,sh} = a \cdot DT\phi + b \quad \longrightarrow \quad DT\phi_{gas,sh} = 1.000 \cdot DT\phi + 0.0445 \qquad R^2 = 0.999 \tag{21}$$

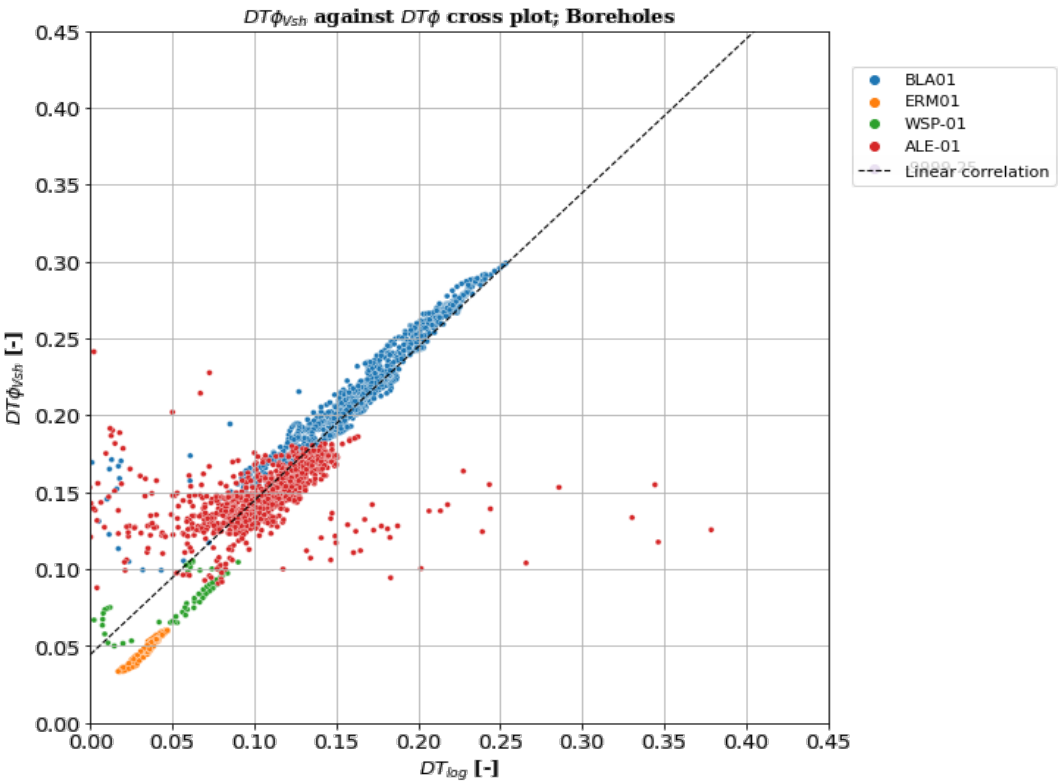

Figure 33: Coloured points: effective $DT\phi_{sh,gas}$ data points against absolute $DT\phi$ data points along wells ALE-01, BLA-01, WSP-01 & ERM-01 black dotted line: linear correlation line.

2.4.10. The Water Saturation Analysis

To estimate the permeability of the reservoir formation, the irreducible water saturation within the formation has to be known. To approximate the irreducible water saturation, the water saturation in the formation has to be calculated. Therefore, first the water saturation logs were computed. This subsection, first discusses the methods used to compute the water saturation logs along the wells, hereafter the estimation of the irreducible water saturation logs are described, and lastly the validation and calculations of the permeability are discussed.

The Water Saturation & Permeability Sensitivity Analysis

To estimate the water saturation logs along the boreholes, the Archies constants are approximated, which is described and discussed in Appendix **A.10**. Three methods are used, retrieved from Gonzalez, O. (2012) **[19]**, to compute the water saturation logs along the borehole BLA-01: Simondoux Gonzalez, O. (2012) **[19]**, Leveaux, J., & Poupon, A. (1971) **[26]**, and Fertl, W. H. (1975) **[15]**. The water saturation logs are plotted against the previously estimated effective DT porosity log for this well in a Buckles Diagram, following the procedure from Buckles, R.S. (1965) **[8]**, and are presented in Figure **34**. The lowest water saturation corresponding with the lowest effective porosity data points situated left in the Buckles diagram are selected and used to approximate the irreducible water saturation logs, using the relation from Buckles, R.S. (1965) **[8]** as presented in Equation **22**. The irreducible Bulk Water Volume BWV values are determined and listed in Table **15**.

The irreducible water saturation for the three water saturation logs is estimated based on the Buckles diagrams along well BLA-01. Hereafter, the three irreducible water saturation logs are used as input to estimate the permeability profiles along the well BLA-01, by usage of the using the relationship, as retrieved from Wyllie, M. R. J., & Rose, W. D. (1950) **[46]** and presented in Equation **23**. The three permeability logs are validated against core plug permeability data points that were retrieved from NLOG and are shown in the figure **75** within Appendix **A.11**. For each permeability log the SSR is computed and presented in Table **14**. The permeability log based on the Leveaux, J., & Poupon, A. (1971) **[26]** irreducible water saturation log has the lowest SSR value of 1.26 $\cdot 10^{+00}$. Therefore, this water saturation method for computing the water saturation log is selected to have the best permeability results of the reservoir formation.

In Equations **22** & **23**, the following symbols are defined: k the log permeability $[mD]$, ϕ_{Vsh} the effective DT porosity based on the I_{GR} distribution in $[\frac{m^3}{m^3}]$, $S_{w,irr}$ the irreducible water saturation distribution $[\frac{m^3}{m^3}]$, and c the retrieved irreducible BWV constant $[-]$.

$$S_{w,irr} = \frac{c}{\phi_{Vsh}} \tag{22}$$

$$k = (100 \cdot \phi_{VSH}^2 \cdot \frac{(1 - S_{w,irr})^2}{S_{w,irr}} \tag{23}$$

Table 14: The log permeability means μ and the SSR values along the borehole BLA-01

S_w Method	$k_{Wyllie\&Rose}$ *(Fertl, W. H. (1975) [15])*	$k_{Wyllie\&Rose}$ *(Simondoux Gonzalez, O. (2012) [19])*	$k_{Wyllie\&Rose}$ *(Leveaux, J., & Poupon, A. (1971) [26])*
μ *[mD]*	$8.27 \cdot 10^{+02}$	$1.45 \cdot 10^{+02}$	$1.60 \cdot 10^{+02}$
SSR [Darcy]	$6.66 \cdot 10^{+02}$	$3.33 \cdot 10^{+01}$	$1.26 \cdot 10^{+00}$

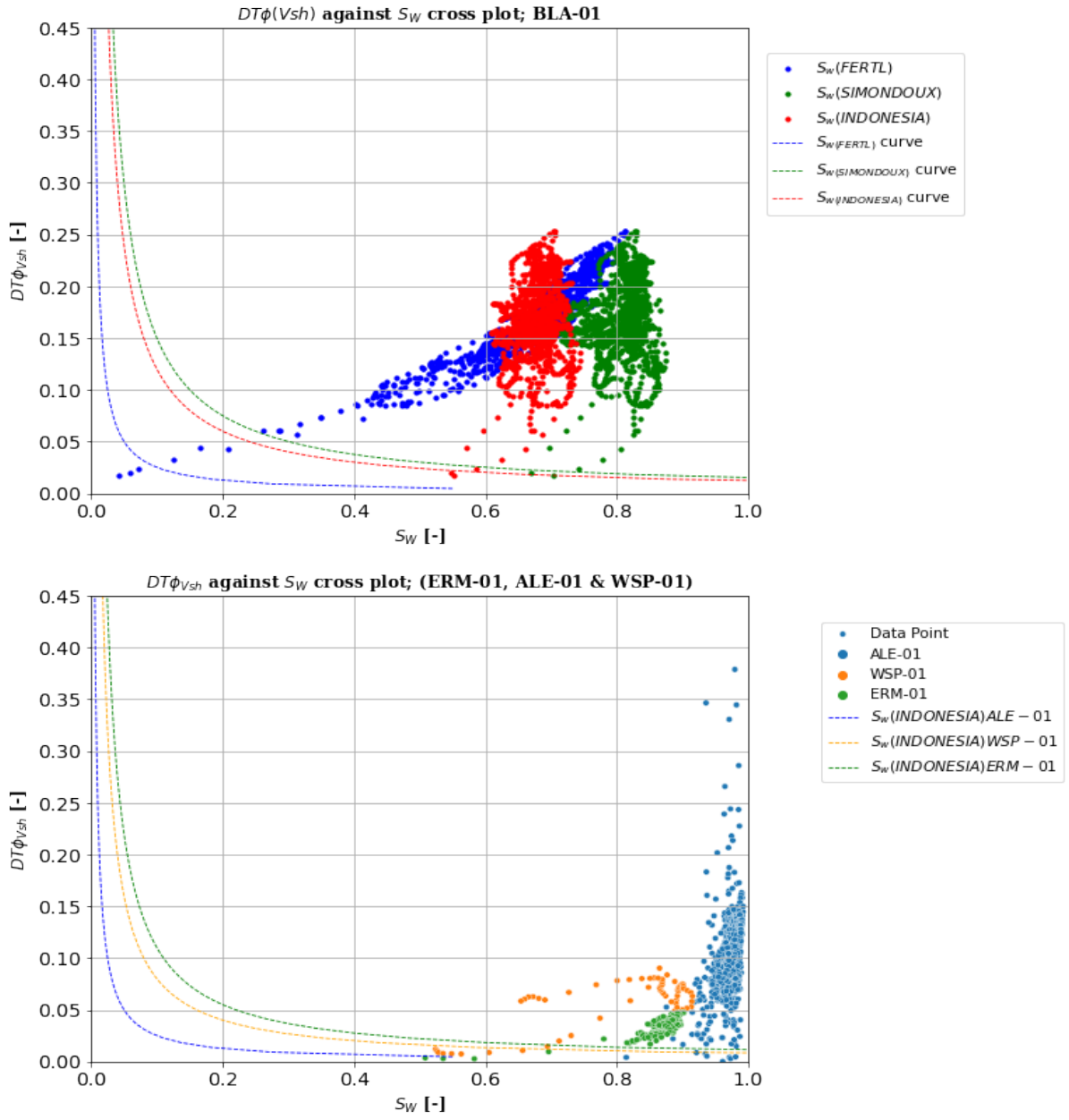

Figure 34: Upper plot: Buckles diagram for well BLA-01, with three irreducible water saturation logs plotted against the effective porosity logs. Lower plot: Buckles diagram for wells WSP-01, ERM-01 and ALE-01, with the Leveaux, J., & Poupon, A. (1971) [**26**] irreducible water saturation logs plotted against the effective porosity logs along these wells.

The Water Saturation & Permeability for the Remaining Wells

To estimate the permeability logs along the remaining wells in this study, water saturation logs based on the Leveaux, J., & Poupon, A. (1971) **[26]** approach for the boreholes ALE-01, WSP-01 and ERM-01 with available resistivity logs are approximated. In addition, their irreducible water saturation logs are determined by constructing their Buckles diagrams, shown in Figure **34** and approximating their BWV constants which are listed in Table **15**. The corresponding Leveaux, J., & Poupon, A. (1971) **[26]** water saturation logs and their irreducible water saturation logs along the wells ALE-01, WSP-01 and ERM-01 are plotted and shown in Figure **35**. Their permeability logs are estimated as well as on the relationship of Wyllie, M. R. J., & Rose, W. D. (1950) **[46]**.

The permeability logs along these ALE-01, WSP-01 and ERM-01 wells are plotted against their corresponding porosity logs, as presented in figure **75** in Appendix **A.12**. Based on this cross-plot and using exponential regression, an exponential porosity-permeability correlation is approximated, and is presented in Equation **24**. The other wells BNV-01, JUT-01, and WRV-01 do not have resistivity logs to approximate their water saturation logs. Their permeability logs are estimated on the basis of using the exponential porosity against permeability function and their previously estimated porosity logs.

In Equation **24**, the following symbols were utilized: k the permeability in $[mD]$, ϕ_{Vsh} the effective DT porosity based on the I_{GR} volume of clay method $[-]$, a, b, c exponential regression coefficients $[-]$.

$$k = ae^{b \cdot \phi_{Vsh}} - c \quad \longrightarrow \quad k = 229.57e^{3.56 \cdot \phi_{Vsh}} - 229.55 \qquad R^2 = 0.698 \tag{24}$$

Table 15: Irreducible BWV constants as function of the water saturation method for the boreholes ALE-01, WSP-01, ERM-01 & BLA-01. *NA*: BWV constant not determined.

Borehole	**BLA-01**	**ERM-01**	**WSP-01**	**ALE-01**
c_{VMB} *Poupon & Levandoux (1971) [?]*	$1.20 \cdot 10^{-02}$	$1.10 \cdot 10^{-02}$	$8.00 \cdot 10^{-03}$	$2.50 \cdot 10^{-03}$
c_{VMB} *Simondoux (1970) [?]*	$1.50 \cdot 10^{-02}$	NA	NA	NA
c_{VMB} *Fertl (1975) [?]*	$2.50 \cdot 10^{-03}$	NA	NA	NA

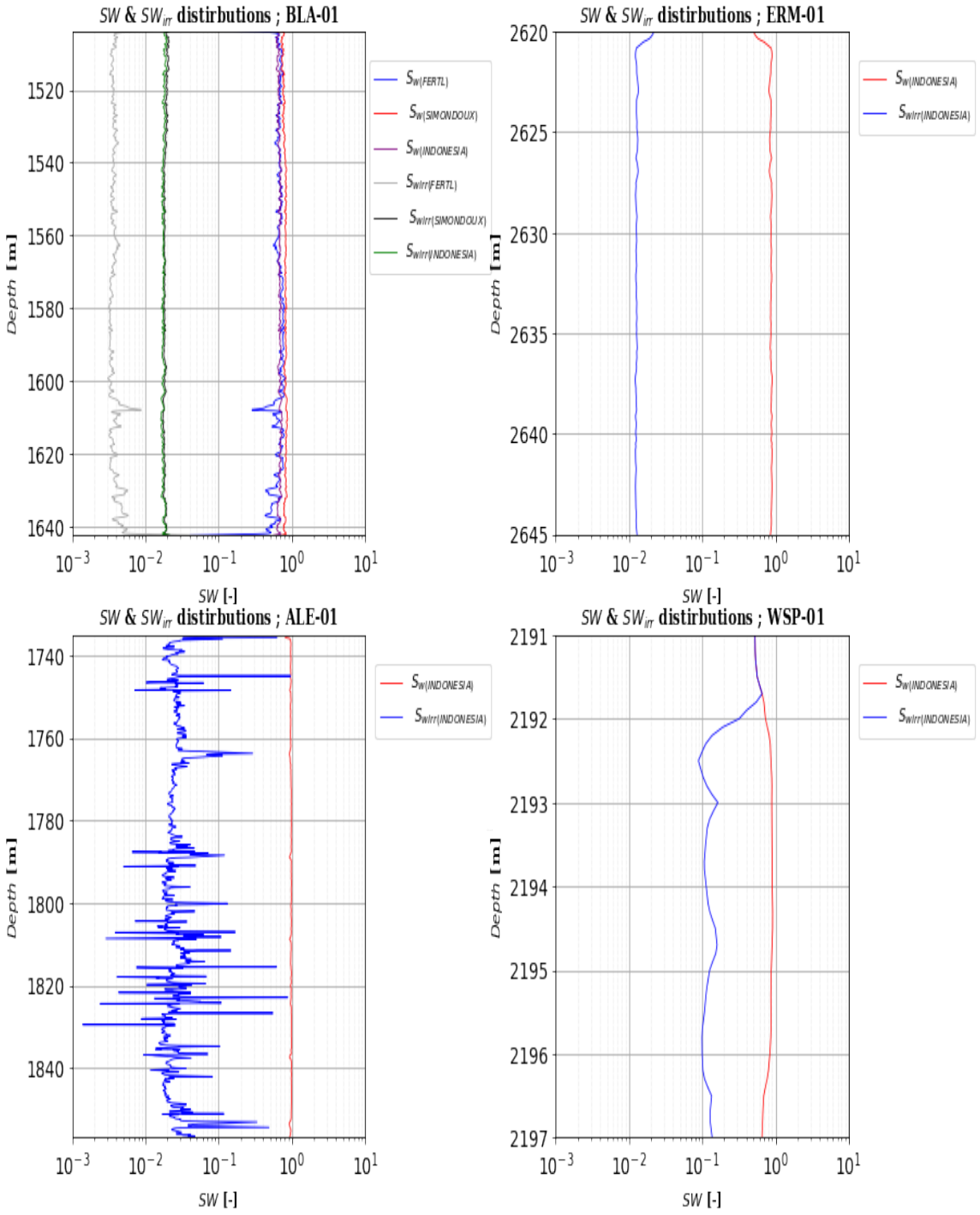

Figure 35: Diagram showing within the two lower plots and the upper right plot their Leveaux, J., & Poupon, A. (1971) [**26**] water saturation distribution and their irreducible water saturation distributions along respectively the three boreholes ALE-01, WSP-01 and ERM-01. The upper left plot shows both the three mentioned water saturation logs and irreducible water saturation logs along borehole BLA-01.

2.4.11. The Facies Porosity Cut-off Values

The facies determined in section **2.3** of this chapter need to be scaled up from the core slab intervals towards the log intervals. To scale-up these facies groups, porosity as well as permeability cut off values are estimated, based on the range of porosity and permeability data values categorized for each facies group. The average and the standard deviations for both porosity and permeability are approximated. Since it is shown that the standard deviations for the permeability are too large for each facies group, the usage of the permeability as cut-off value is not considered. To scale up the facies based on the porosity cut-off, bounds are formulated as defined by the following relations Catinat, M., et al. (2023) **[11]** ($\phi_{min} = \phi_{\mu_{facies}} + (0.1 \cdot \phi_{\sigma_{facies}})$ & $\phi_{max} = \phi_{\mu_{facies}} - (0.1 \cdot \phi_{\sigma_{facies}})$). For the facies groups with the lowest and highest porosity averages, their values are set to be equal to the lowest and the highest porosity values along their porosity data range respectively.

Table 16: Facies groups and their characteristic porosity and permeability ranges, including standard deviations. μ stands for the mean value, standard deviation is denoted by σ. Values used as input to calculate porosity cut-off values

Facies unit	***Porosity*** $[-]$				***Permeability*** $[mD]$	
Statistics	μ	σ	$\mu - (0.1 \cdot \sigma)$	$\mu + (0.1 \cdot \sigma)$	μ	σ
FC	0.1129	0.0203	0.1109	ϕ_{max}	24.43	26.68
AD	0.1030	0.0439	0.0986	0.11088	25.66	28.95
SS	0.0986	0.0353	0.0629	0.0986	31.52	31.01
ID	0.0608	0.0211	0.0365	0.0629	56.03	27.13
SF	0.0360	0.0422	ϕ_{min}	0.0365	13.79	12.72

2.4.12. Results

First, the volume of clay data ranges approximated and described in Sub-subsection **2.4.6** are presented. The results of the calculation show that the volume of clay log of the I_{GR} methodology has the highest cut-off value point, namely above the 20%, while the volume of clay logs from the Stieber, S. J. (1970) **[37]** and Larionov Tertiary Rocks (1969) **[25]** methods have the lowest volume of clay cut-off points of below the 10%. The Clavier, et al. (1971) **[12]** methodology shows to have an volume of clay cut-off point of 12.8%. Since it was determined that most of the core slabs in section **2.3** are composed of eolian facies units and due that the volume of clay content within eolian formations is generally between the 10% and 20%, the facies cut-off point of 12.8% from the Clavier, et al. (1971) **[12]** method was selected to be the most appropriate facies cut-off value. The volume of clay logs and their cut-off values are presented in Figure **36**.

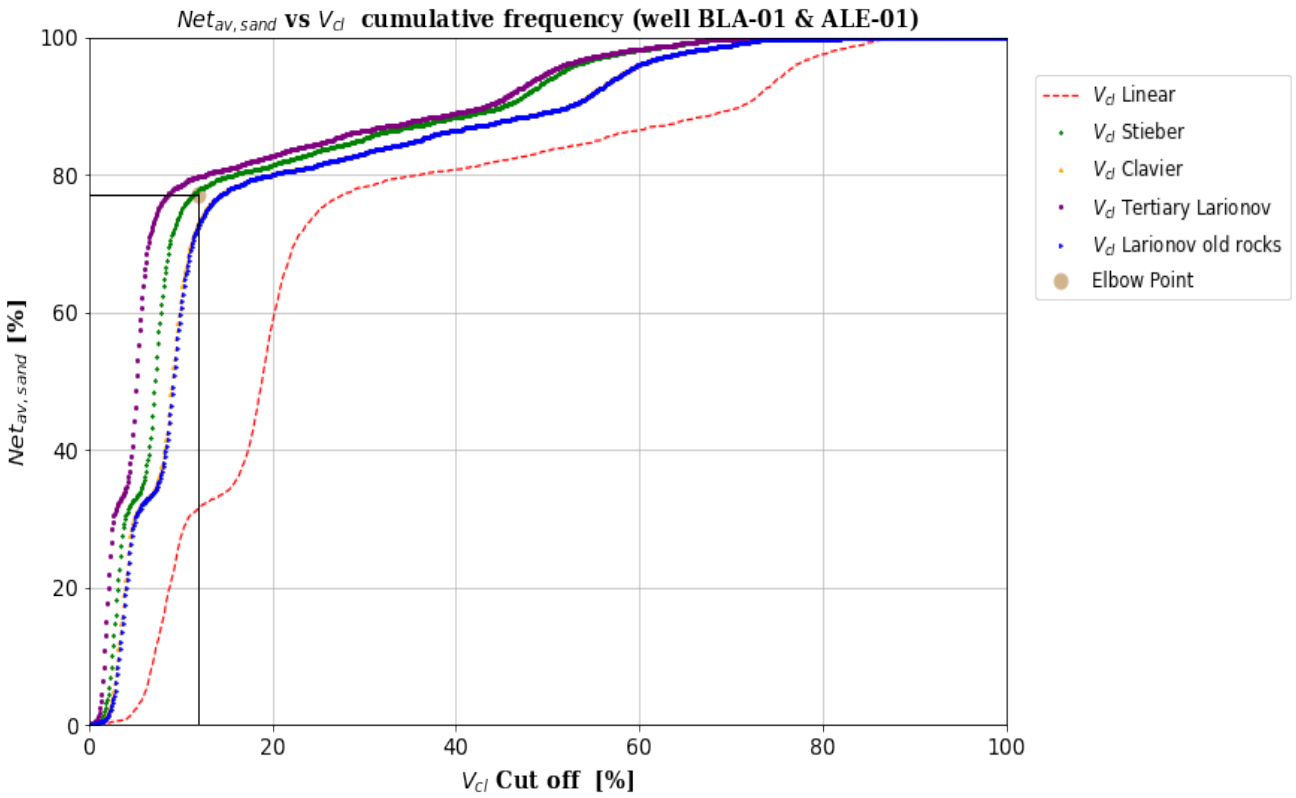

Figure 36: Coloured curves: the non-linear volume of clay models and linear volume of clay model cumulative frequency histograms. The brown point: the V_{cl} Clavier, et al. (1971) [**12**] cut-off elbow point.

To estimate the net sand logs of the reservoir formation, the effective porosity cut-off value was determined. The effective porosity cut-off value is determined based on plotting the effective porosity logs of all wells against a porosity cut-off value range from 0% to 45%, a shown in Figure **37**. The deflection point of the curve in the diagram is selected and determined to have a porosity cut-off value of 2.5 %.

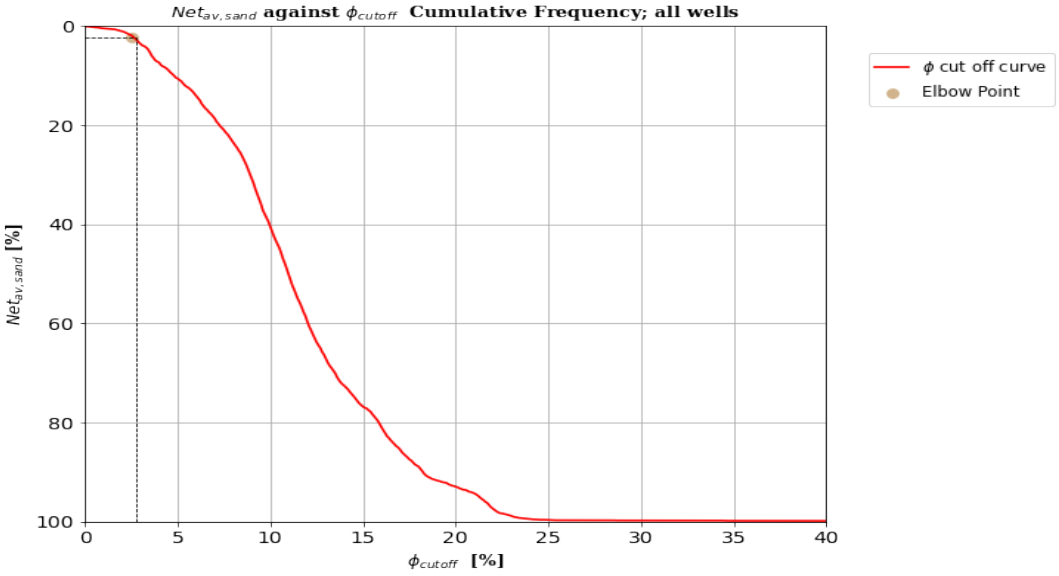

Figure 37: Red curve: the DT ϕ_{IGR} cumulative frequency diagram. Brown point: the DT $\phi_{D(IGR)}$ elbow cut-off value.

As well as for the volume of clay the cut-off value is estimated, all the volume of clay logs along the wells are plotted against a volume of clay cut-off data range, which is presented in Figure **38**. The volume of clay deflection point of the curve in the diagram is determined, for having an volume of clay cut-off point of 42%.

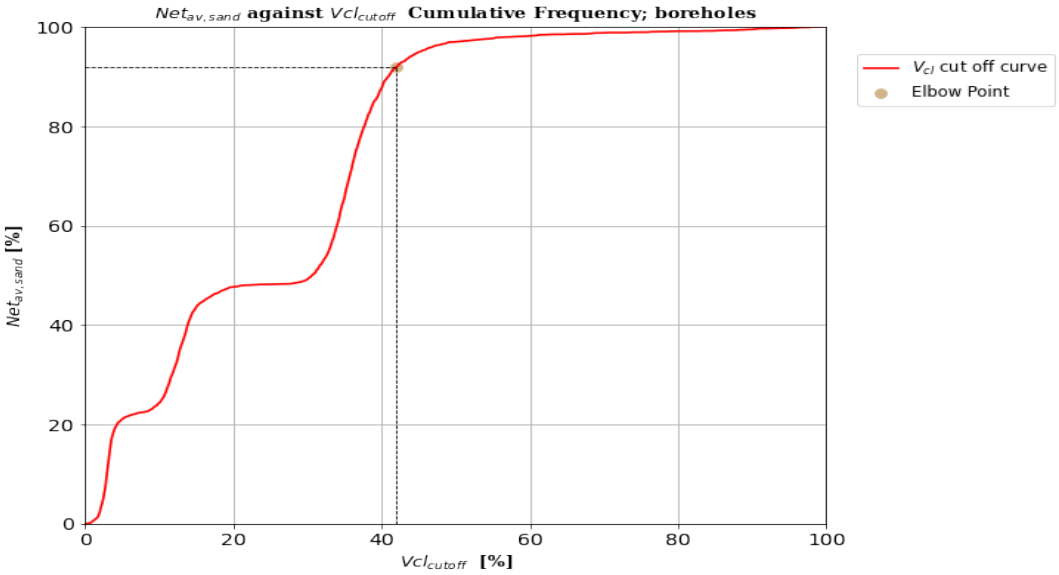

Figure 38: Red curve: the I_{GR} volume of clay cumulative frequency diagram. Brown point: the I_{GR} volume of clay cut-off elbow point.

The resulting volume of clay distributions along the wells with available GR logs based on the linear I_{GR} method are presented within Figure **39**.

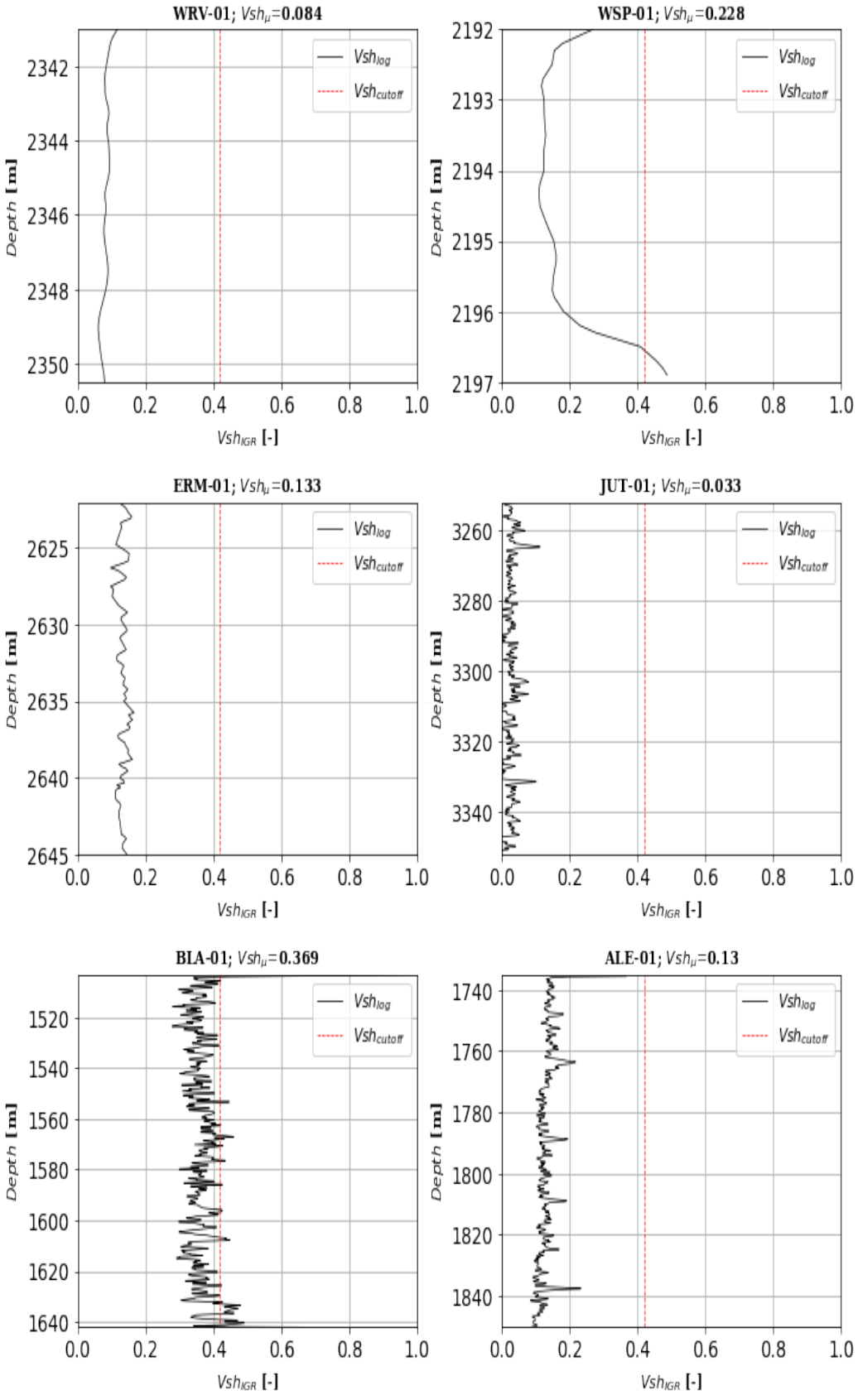

Figure 39: The I_{GR} volume of clay distributions along the six boreholes with an available GR log (as shown in Table 4).

Both the effective porosity cut-off value of 2.5% and the volume of clay cut-off value of 45% are used to estimate the net sand logs along the wells in this study. Since the borehole BNV-01 has no available GR log the volume of clay log can't be calculated, so that the net sand log for this well only is estimated on the porosity log. The average net sand is computed along all the wells in this study and is estimated to be 0.909 $[-]$. The resulted net sand distributions based on both the used porosity and volume of clay cut off points are plotted and presented in Figure **40**.

The effective DT porosity logs along all wells, which are estimated based on the porosity validation method described in Subsection **2.4.7**, are presented in Figure **41**. The resulting permeability logs along the wells that are used as input in Petrel to generate the permeability geological model as described in chapter **3** are presented in Figure **42**.

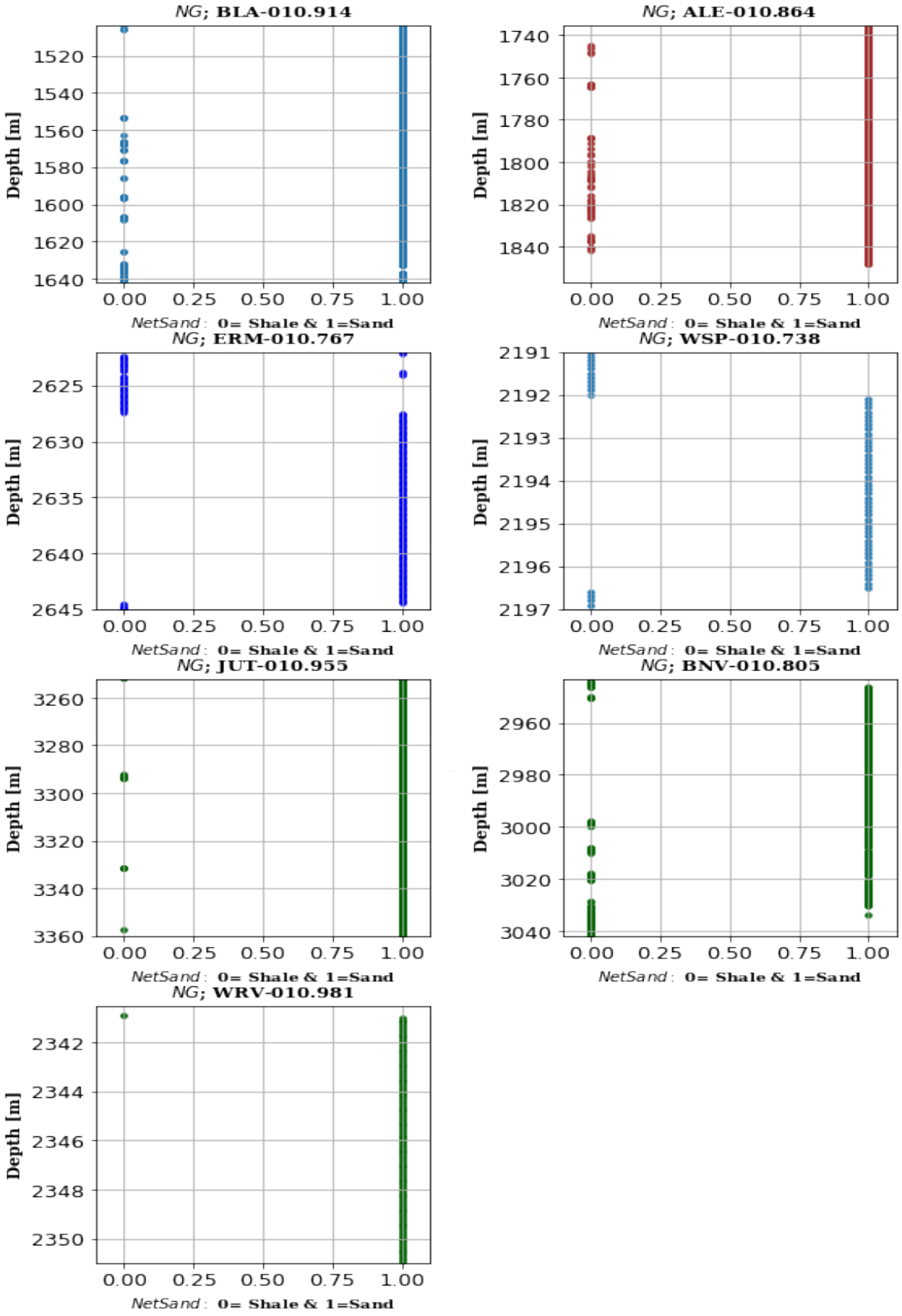

Figure 40: Coloured points: the net sand (*clay* = zero & *sand* = one) distributions along all the boreholes.

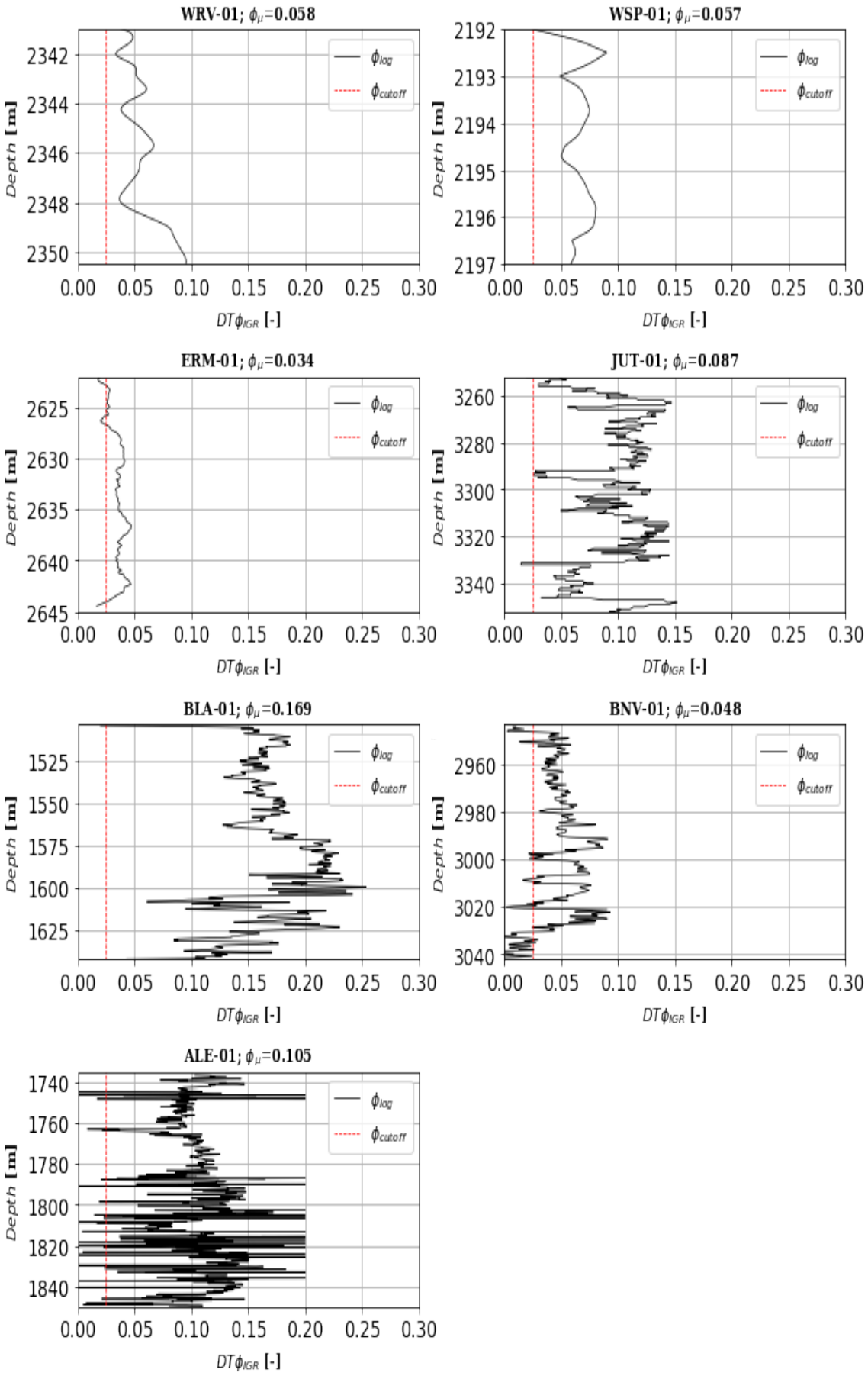

Figure 41: The effective DT porosity based on the I_{GR} volume of clay method distributions (logs) along all the boreholes.

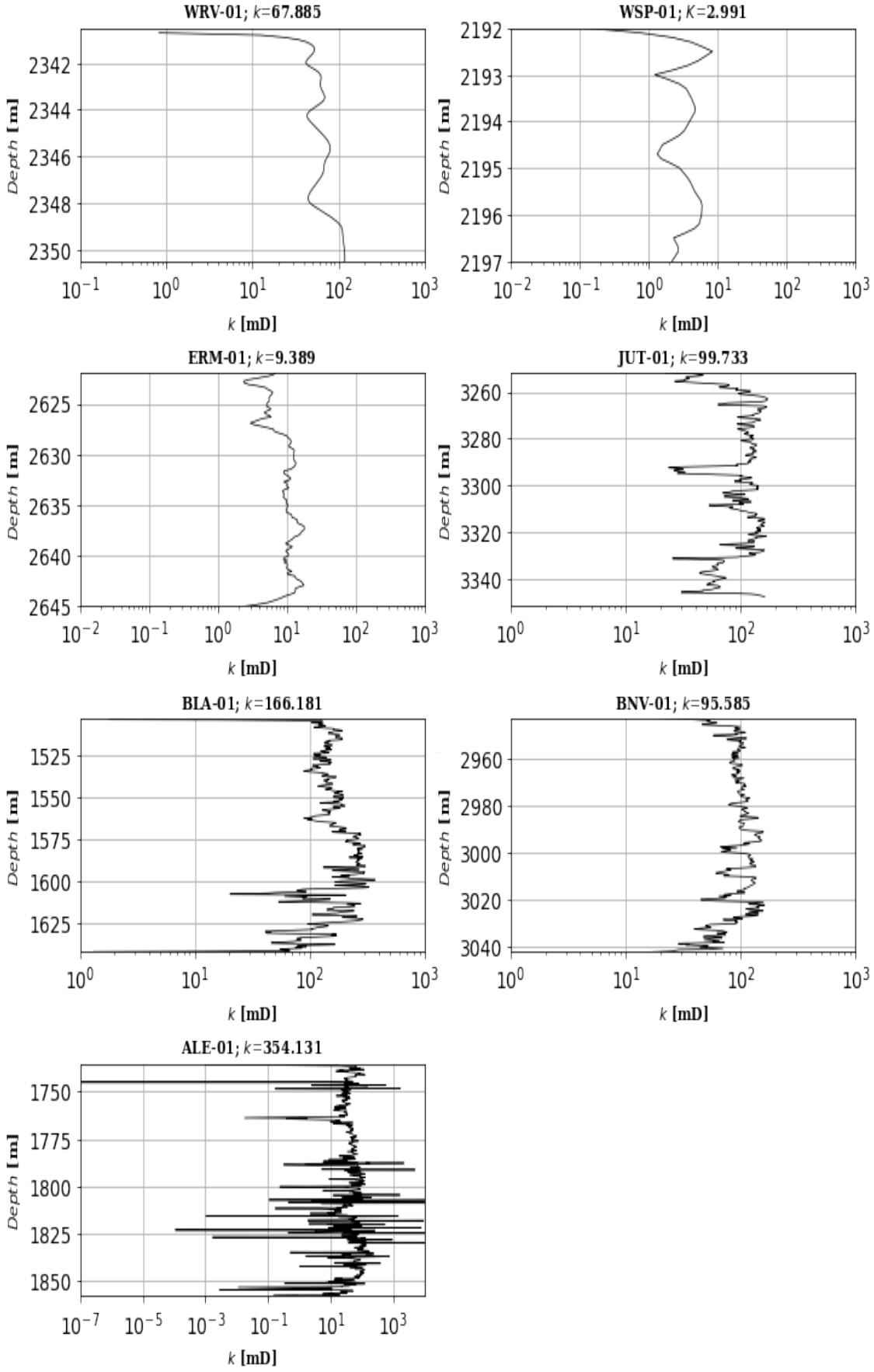

Figure 42: The estimated permeability distributions (logs) along all the wells.

2.4.13. Discussion & Conclusion

Throughout the previous discussed subsection, both the methods and data are described to estimate the reservoir properties of the reservoir formation. This work resulted in the estimation of the volume of clay, effective porosity, permeability and net sand logs along all wells in this study. However, some points of uncertainty arose while executing the work, which are discussed in the following description.

For the GR correction described in Subsection **2.4.3**, it is assumed that the GR log along the well ALE-01 can be used as reference for the GR log of the well BLA-01. However, the approximated GR correction factor, and therefore the corrected GR log along the borehole BLA-01 could be limited in accuracy, as it is not known or estimated to what extent there exist heterogeneities of the lithology in the reservoir formation, between each of the boreholes BLA-01 and ALE-01.

The gas density presented in subsection **2.4.6** is estimated based on a constant gas composition in the reservoir formation. However, the gas composition is rarely constant throughout the reservoir formation, and therefore varies from well to well. The variable gas density implies that the results of the porosity calculations, which are dependent on this gas density, may just be as variable within their data ranges.

For the pore volume reduction factor of the pore plug porosity data points correction, described in subsection **2,4.7**, a general factor is assumed. To correct their core plug porosity data points much more accurately, it is possible to use a method that estimates this porosity reduction factor much more accurately, however the method requires a large number of analyses, which was beyond the scope of this thesis project.

For the water saturation estimations described in section **2.4.9**, both the cementation exponent and the saturation exponent are set as constants. Since both exponents have a large impact on the resulting saturation logs, it could be useful to set the exponents as variables, instead of constants. That way, when using these data arrays instead of their constants for the Archies exponents, as a result their water saturation distributions are approximated to a higher accuracy, since the solution is less based on assumptions for when single constants were used.

For the permeability of the reservoir formation only the horizontal permeability is estimated, the vertical permeability is not considered and therefore estimated. Since the vertical permeability can give information about the geothermal potential of the reservoir formation, for instance if there is vertical connectivity between the various layers within the formation, it could be of importance to estimate vertical permeability logs along the wells.

3

Geological Modelling

As mentioned earlier, one of the main objectives of this thesis is to create facies distribution maps for the Upper Slochteren Formation in the study region. In this chapter, both methods and results for generating 3D geological maps of the formation and 3D facies maps are discussed to evaluate the geothermal potential of the formation. Based on the resulting porosity, net sand, and permeability from borehole logs, the distributions were modeled across the study area using Petrel.

Following the generation of distributions, the focus was on a case study area where the formation exhibited suitable geological properties for the utilization and further exploration of DGE. Subsequently, key insights from geological modeling are discussed, and the results are summarized in a concluding section. The entire methodology used in this chapter for generating the resulting maps is illustrated in a flow diagram (Figure **43**).

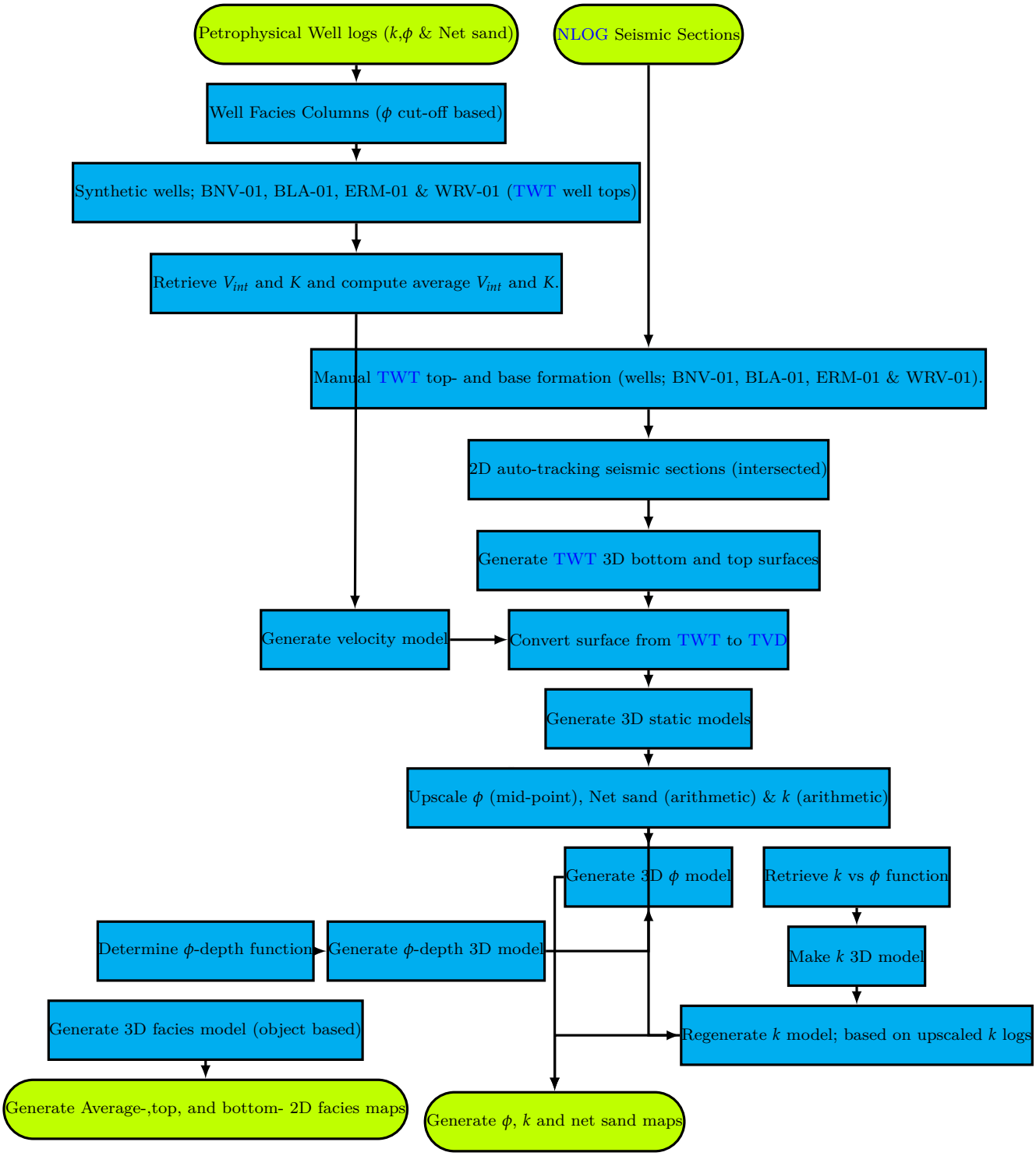

Figure 43: The workflow for the chapter: the individual methods (blue rectangles), the inputs & outputs (lime rounded rectangles), and the relationships of the individual methods (black arrows).

3.1. The 2D Seismic Interpretations

The depth and thickness maps of the Upper Slochteren Formation were generated using the DGM v5.0 model developed by Vrijlandt, M. A. W., et al. (2019) **[43]**, which is available on NLOG. The model is based on 120 borehole data points, as described on NLOG, no seismic interpretations are included in the formation depth maps and thickness maps generated.

To increase the reliability of the formation depth and thickness distributions, this thesis profits from the now available SCAN 2D seismic sections, which were used in combination with subsequently processed 2D seismic sections (see Table **4** as presented in Section **2.1**). The stacked seismic lines of this seismic data set were obtained from NLOG and imported into Petrel. Since their depths are measured in Two-Way Travel Time (TWT), a velocity model was generated to convert travel times to True Vertical Depth (TVD).

To generate the 3D velocity model, synthetic well logs were generated along the borehole profiles BLA-01, WRV-01, BNV-01, and ERM-01, which intersect existing 2D seismic sections (see corresponding logs in Appendix **A.16**). Based on their resulting interval velocity well logs, their corresponding velocity gradients were calculated and plotted against each other for the formation in a cross-plot (as shown in Figure **45**). From this cross-plot, their average values were determined, which were then put into the velocity-corrected compaction equation of Van Dalfsen, W., et al. (2006) **[13]** (as presented in Equation **25**). After generating the 3D velocity model in Petrel, the TWT interpretations were then converted into TVD interpretations.

In Equation **25**, the symbols are defined as follows: V_O the model velocity in $[\frac{m}{s}]$, Z the depth of the formation $[m]$, V_{int} the interval velocity in $[\frac{m}{s}]$, and K the velocity gradient in $[\frac{m}{s \cdot m}]$.

$$V_O = V_{int} + (K * Z) \quad \Longrightarrow \quad V_O = 4179.80 + (0.2419 * Z) \tag{25}$$

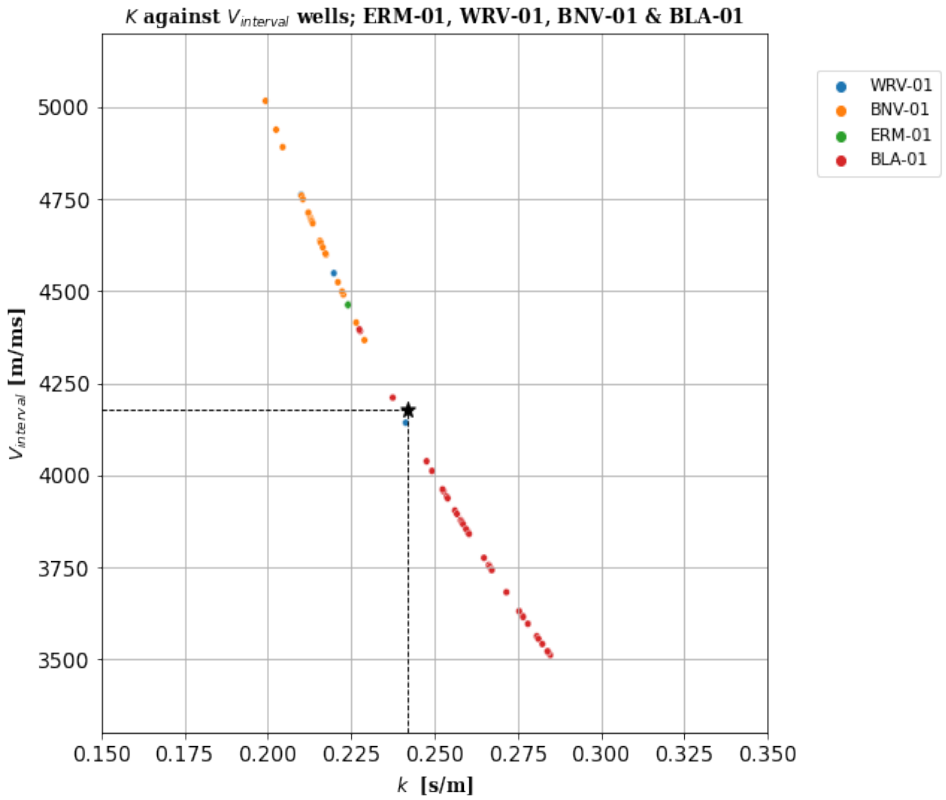

Figure 44: Coloured points: the interval velocity against the velocity gradient data points for wells ERM-01, BNV-01, and BLA-01. Black dotted lines: the average velocity gradient and average interval velocity.

Due to the decreasing resolution of seismic data with increasing subsurface depth, the current DGM model does not interpret the top and bottom of the formation, namely the Base ZE and BPU. In this thesis, the Base ZE and BPU reflectors were interpreted along the 2D seismic sections as follows: first, both the formation top and bottom along the borehole profiles were merged with the formation's top and bottom reflectors. Next, the reflectors were manually interpreted near the borehole trajectories. Reflectors further away from the wells were interpreted using a confidence level of 70% and 2D autotracking. Finally, seismic interpretations were conducted along intersected 2D seismic lines.

After interpreting the reflectors for all 2D seismic sections, 3D surface maps of both the formation top and bottom were generated in terms of TWT. These maps were then converted to 3D TVD maps by utilizing the 3D velocity model. Due to the large extent of the study area and the low well density, a considerable large grid dimension of 100 by 100 m was chosen for map generation. Additionally, the simple kriging method was employed, utilizing the global well adjustment operator with a point weighting of the inverse distance squared to create the residual depth surface. In addition, a well influence radius of 50 km was used.

Since some of the seismic sections were interpreted outside the borders of the study area, a polygon was created in Petrel to omit the areas outside the study domain, and generate trustworthy surfaces.

After generating both top and bottom formation depth maps, the bottom map was subtracted from the top map using the TST algorithm to create the 3D TST map of the formation. The top, bottom, and TST distributions of the formation are displayed in the maps (Figures **46**, **47**, and **48**.

3.2. The Static Modeling Methods

The resulting property logs from the log analysis were utilized and upscaled within the adjacent grid cells. The method employed to populate the porosity, permeability, net sand, and facies logs in the reservoir grid is discussed in this section.

This section is divided into the following subsections: first, the well logs of the formation are populated in adjacent grid cells (Subsection **3.3.1**). Next, a depth versus porosity log correlation is addressed (Subsection **3.3.2**). Finally, the upscaled grid cells are distributed over the entire 3D reservoir grid (Subsection **3.3.3**).

3.2.1. The Well Log Upscaling Procedure

Because the number of data points during upscaling from the well log towards the grid cell has degraded considerably, a large portion of detail is lost. For that reason the favorable 'simple' upscaling approach was selected. To further reduce the loss of detail during upscaling, all the data points within the well log interval were grouped to a total number of twenty data points before they were populated.
Subsequently, all the geological well logs were populated utilizing the 'arithmetic average method', as it provides greater accuracy than the midpoint, random point, harmonic average, and most other upscaling techniques.

3.2.2. The Depth against Porosity Correlation

As the magnitude of formation porosity depends not only on lithological and sedimentary rock properties but also on the degree of rock compaction, a Medium Depth (MD) versus porosity function was derived based on all well log porosity borehole profiles (Equation **26** and Figure **45**). This function was derived in Petrel by resolving all the porosity well log intervals against their corresponding MD points. By utilizing this correlation in the original 3D depth model, an ancillary 3D porosity correction model was generated, improving the primary 3D porosity model for variations due to compaction and burial depth.

In Equation **26**, the following symbols are used: Z the well log MD $[m]$, ϕ_e the clay-corrected well log porosity $[-]$, a the porosity slope coefficient $[-]$, and b the depth-intercept coefficient $[m]$.

$$Z = a \cdot \log \phi_e + b \quad \longrightarrow \quad Z = -1417.87 \cdot \log \phi_e + 744.57 \qquad R^2 = 0.646 \qquad (26)$$

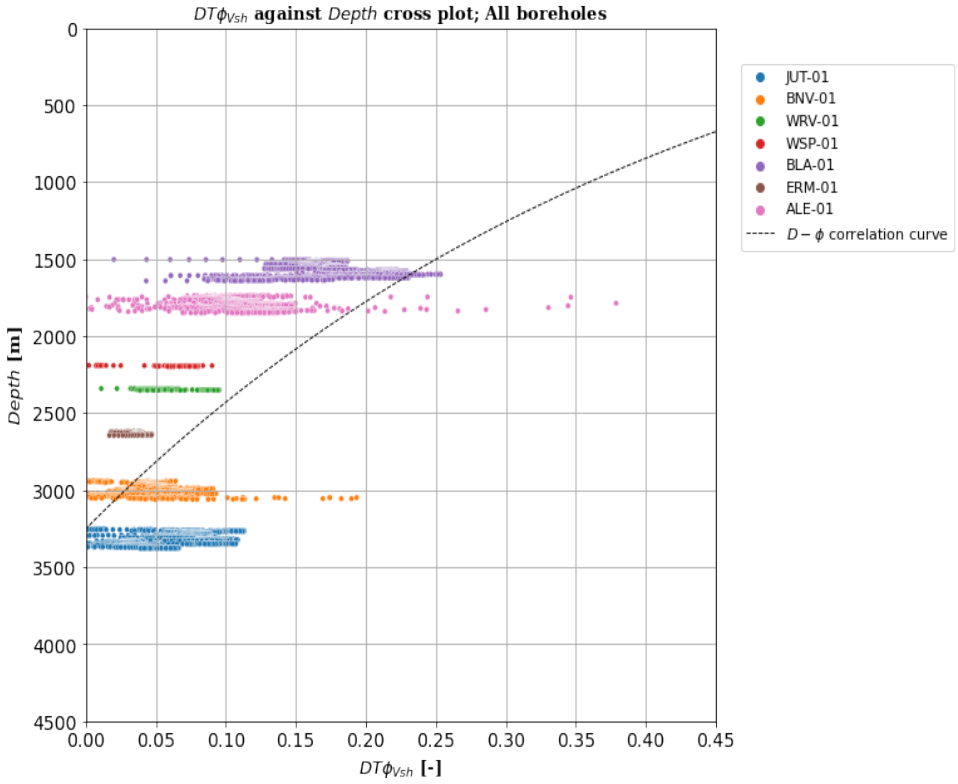

Figure 45: Coloured points: The validated effective porosity log data points along all boreholes. Black dotted curve: the porosity against depth exponential correlation.

3.2.3. The Well Log 3D-Grid Interpolation Approaches

The upscaled cells of the borehole profiles across the entire 3D reservoir grid were interpolated by utilizing the Gaussian Random Simulation interpolation method. The advantage of using this algorithm is that it preserves the original borehole log distribution as much as possible during interpolation. Due to the limited borehole log information across the entire study area, a 'Normal' distribution was chosen for interpolating the upscaled porosity cells, assigning extra weight to the original well log distributions. The 3D porosity correction model, as previously mentioned, was used to correct the porosity distribution during interpolation for compaction variation across the study area.

For interpolating the upscaled permeability cells, another method was used. Due to the dependency of permeability on porosity, the upscaled permeability cells were interpolated assuming a bi-variate distribution based on the previous 3D porosity model. Additionally, a porosity-permeability trend relationship was used, derived from the resulting 3D porosity model, to align the permeability distribution with the porosity distribution.

The sequential indicator methodology was employed for interpolating the upscaled net sand grid cells, aiming to maintain the original borehole log net sand distribution as much as possible. Additionally, the original net sand proportions from the well logs were utilized, instead of the upscaled net sand cells. The interpolated net sand distribution was used as a background model for the net sand distribution. The 3D average surface maps for the resulting porosity, permeability, and net sand models were then generated (Figures **46**, **47**, & **48**).

3.3. The 3D Facies Model Approach

Facies logs were generated based on porosity cutoff values along wellbore profiles. The resulting facies columns for boreholes ALE-01, BLA-01, WSP-01, WRV-01 & ERM-01 match well with corresponding columns using interpretations of cuttings for these wells, retrieved from NLOG (as presented in Appendix **A.14**). These facies logs were then upscaled into the 3D grid cells.

Because the facies bodies are defined by their proper wide and height dimensions, their modeled widths and heights may not be truly correspondent with their actual dimensions, when these facies bodies were deposited. A stochastic object-based methodology was selected for distributing their facies units throughout the 3D grid. The advantage of using this algorithm is that it preserves the morphological properties of the facies units, resulting in a realistic facies distribution.

Specific thickness and width ratios from the study by Priddy, C. L., & Clarke, S. M. (2021) **[33]** were used, along with minimum and maximum facies unit thicknesses determined from facies well logs. Using these thickness and width ratios, minimum and maximum widths of facies units were determined. In addition to the dimensions of the facies units, their dominant paleo-orientations were utilized as input, determined from the core slab analysis (Section **2.3**). Both their thickness and width values and paleo-orientations were modeled based on a triangular distribution (as presented in Appendix **A.15**).

The highest weight was assigned to preserving the original facies log distributions, and the background of the 3D facies model was selected based on the resulting facies distribution. For the resulting 3D facies model, both the formation bottom and top facies maps were generated, which are further compared and described in Subsection **3.4.3**.

3.4. The Results

The resulting top and bottom depths, TST, facies, porosity, permeability, and porosity maps are all described in this section. Also, as mentioned in chapter **1** both the bottom and top formation it's facies distributions are discussed.

3.4.1. The Depth and TST Distributions

The formation top and bottom depth maps from the DGM model show that the shallowest top and bottom depths are presented in the southeast (Figures **46** & **47**). On the basis of the work for this thesis, the shallowest top and bottom depths are found in the northwest and not in the southeast. Also, both maps in this thesis show maximum top and bottom depths of more than 4000 m in the northeast , which are on both maps of the DGM model only found in the southwest.

The TST map of the formation shows significant differences with the DGM model (as illustrated in Figure **48**). The DGM model indicates a clear trend of increased TST values towards the North-East region and toward the Southwest, and shows the lowest in the northwest region. Based on the work performed for this thesis, the maximum thickness is in the southwest but not in the northeast. Also the map from this thesis shows regionally maximum thicknesses above 200 meters in the southern part of the map. The pronounced minimum in the DGM model cannot be confirmed.

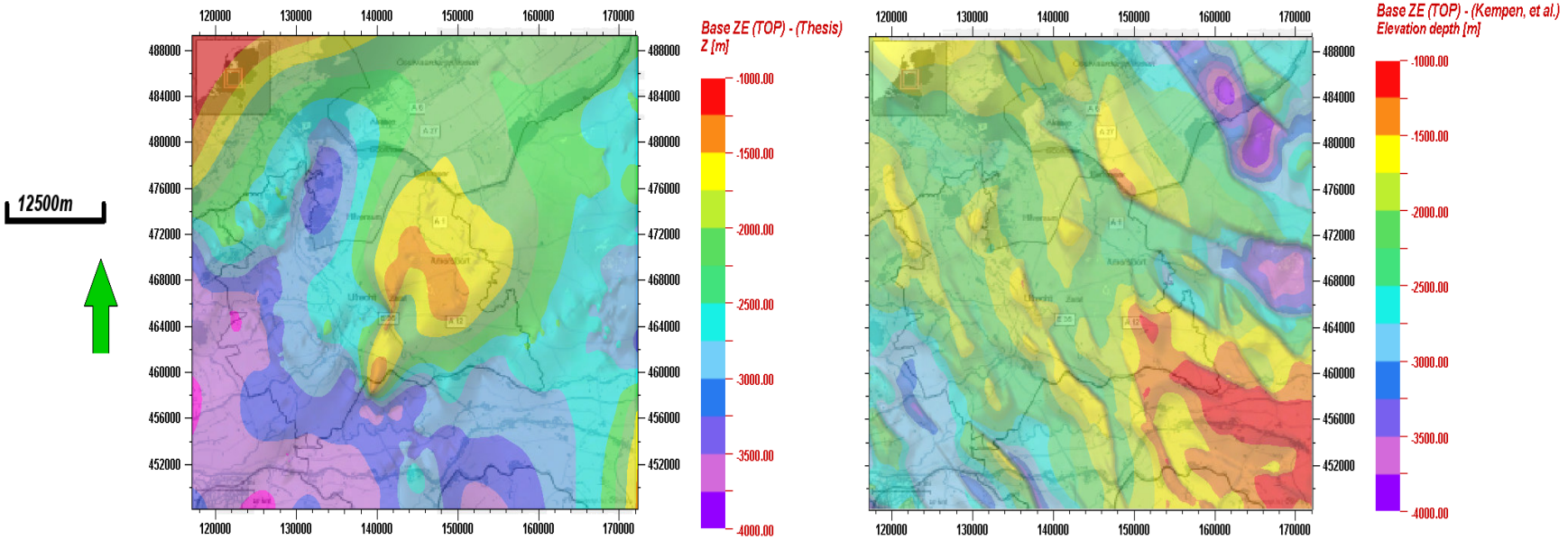

Figure 46: Right: The DGM v5.0 formation top depth map as retrieved from Kombrink, H., et al. (2012) [**22**], and left: Formation top depth map resulting from this thesis.

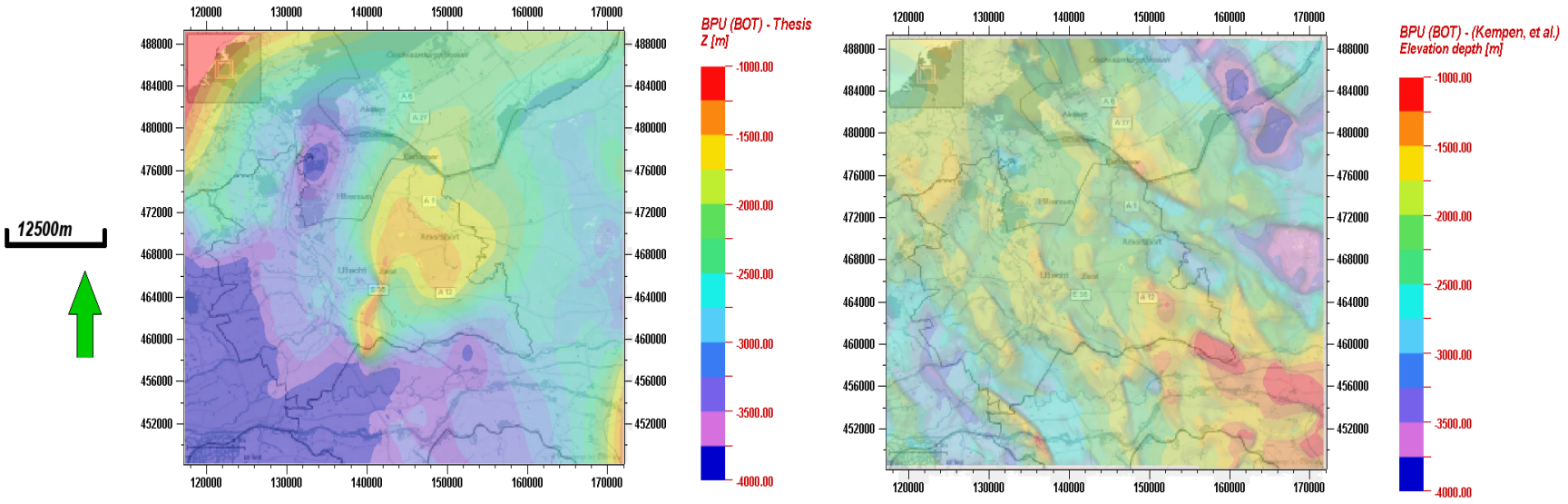

Figure 47: Right: the DGM v5.0 formation bottom depth map as retrieved from Kombrink, H., et al. (2012) [**22**], and left: Formation bottom depth map resulting from this thesis.

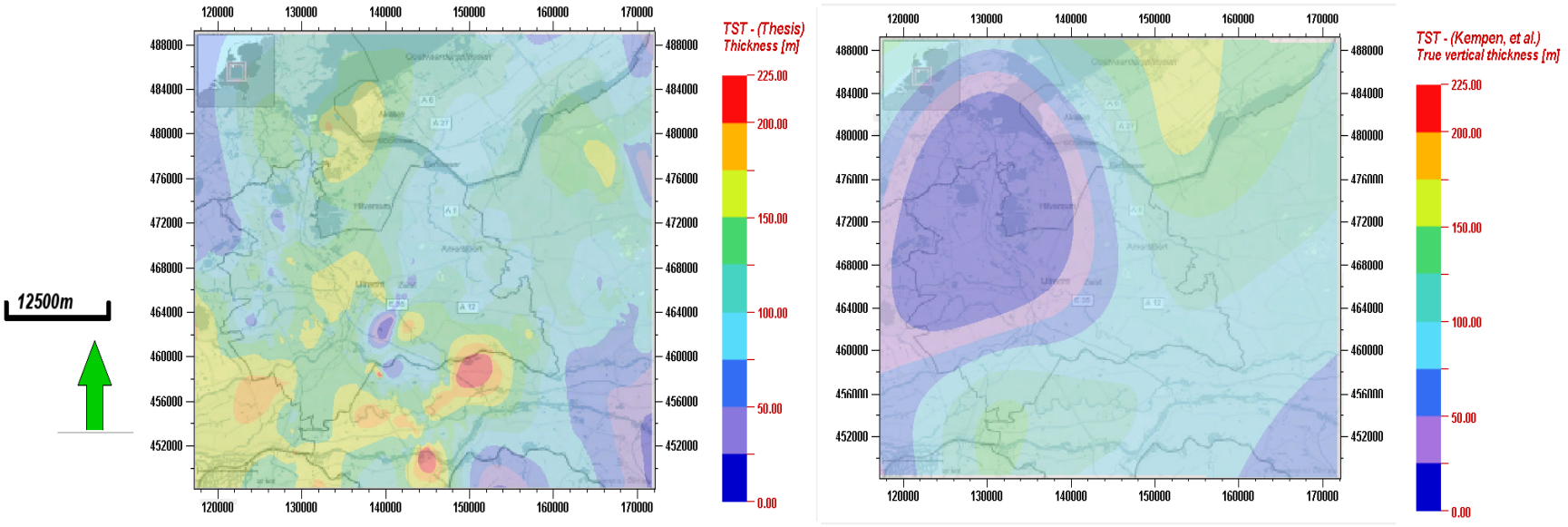

Figure 48: Right: the DGM v5.0 formation thicknesses map as retireved from Kombrink, H., et al. (2012) [**22**], and left: Formation thicknesses map resulting from this thesis.

3.4.2. The Geological Property Distributions

The porosity map from ThermoGIS shows that maximum porosities up to 0.19 are followed by a trend from the southeast towards the northwest within the research area (Figure **49**). Also, the map shows porosities lower than 0.10 within the extreme southwest and across the east of the research area. The map based on this thesis shows maximum porosities between 0.16 and 0.19 throughout the central, extreme northwest, and southeastern areas of the research domain. The lower porosities between 0.10 and 0.13 are found within the remaining parts of the research area.

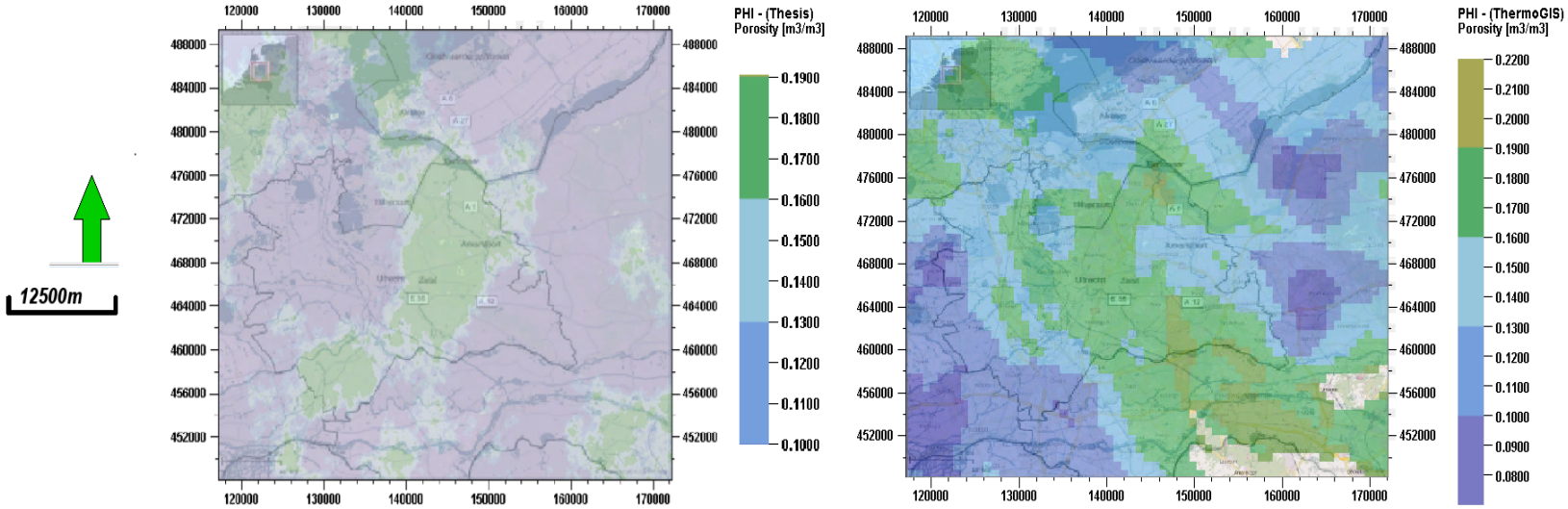

Figure 49: Right: the DGM v5.0 formation porosity map as retrieved from Kombrink, H., et al. (2012) [**22**], and left: Formation porosity map resulting from this thesis.

The permeability map from ThermoGIS shows that the highest permeabilities between 200 mD and 500 mD follow a trend from the southeast towards the northwest (Figure **50**). Also, the map from ThermoGIS shows permeabilities lower than 1 mD in the extreme southwest and in the east of the research region. The permeability map based on the work of this thesis, shows the lowest permeabilities between 2 mD and 5 mD across the areas with coordinates between (longitude= [126000, 140000], latitude= [46800, 48400]) and (longitude= [16000, 17200], latitude= [468000, 480000]). The maximum permeabilities are presented throughout the extreme southeast and northward with their corresponding coordinates of (longitude= [11800, 12600], latitude= [450000, 456000]) and (longitude= [13400, 15800], latitude= [488000, 480000]).

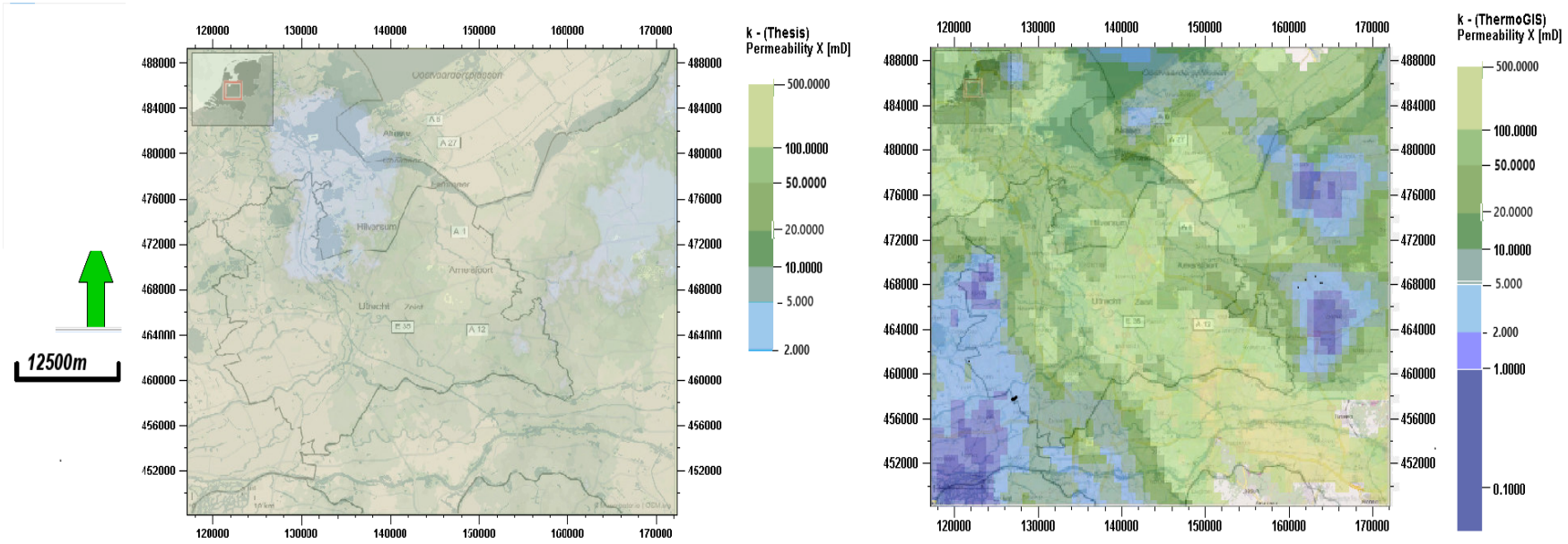

Figure 50: Right: the DGM v5.0 formation permeability map as retrieved from Kombrink, H., et al. (2012) [**22**], and left: Permeability map resulting from this thesis.

The NG map from the DGM model shows that the Upper Slochteren Formation is both sand and shale bearing across the northeastern and in the extreme southwest of the research area, while it is primarily sand bearing throughout the remaining area of the research domain (Figure **51**). The NG map based on this thesis shows that the formation is only both shale and sand bearing within the extreme northeast of the research area, elsewhere, the formation primarily sand bearing.

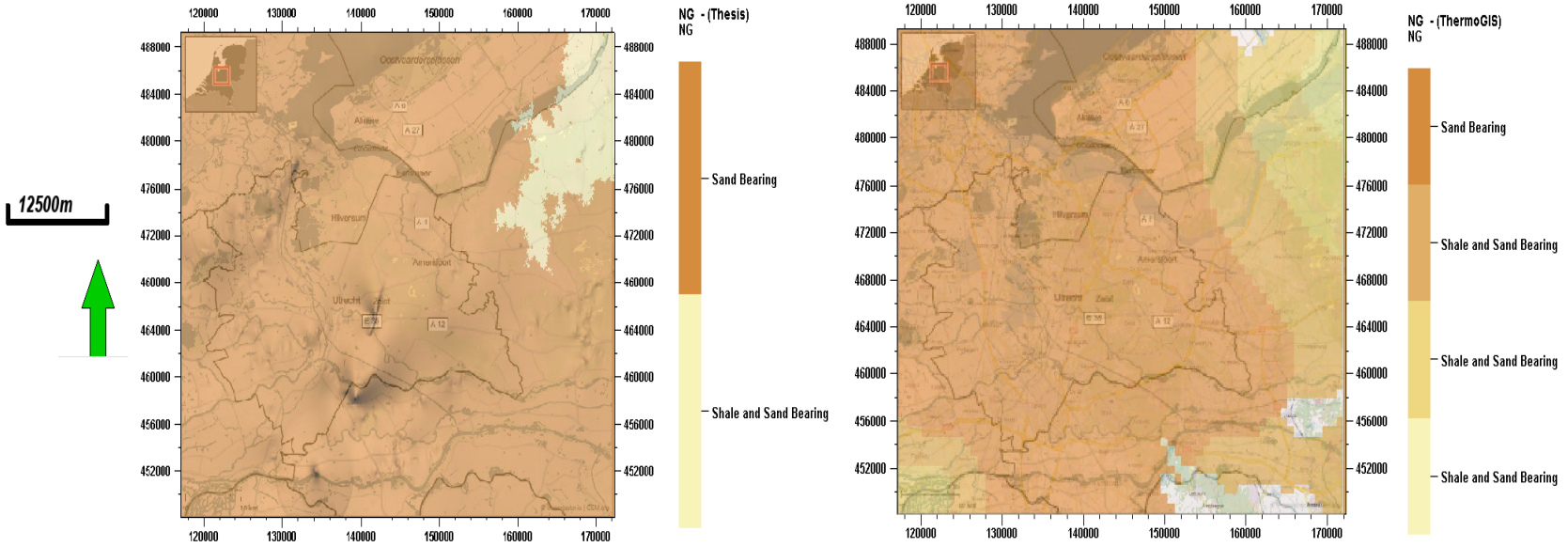

Figure 51: Right: the DGM model based NG map, and left: the NG map based on this thesis.

3.4.3. Facies Top & Bottom Formation Distributions

The facies map of Kortekaas, M. (2023) [**23]** shows that both the fluvial channel and the aeolian dune facies are present within the research area (Figure **52**). The fluvial channel facies are found across the southeast of the research area, while the aeolian dune facies occupy the remaining part of the research area. The facies top map based on this thesis shows that fluvial channel-, sand sheet-, and aeolian dune facies are present across the research area. The sand sheet facies are only found in the extreme northeast and locally in the west. The aeolian dune facies and the fluvial channel facies both follow a trend from the southeast towards the northwest of the research area.

The facies bottom map based on the work of this thesis shows that the bottom of the Upper Slochteren Formation is formed by inter dune-, fluvial channel-, and aeolian dune facies across the study area (Figure **53**). The inter dune facies are only found in the northeast of the research area, the fluvial channel facies is present in the southwest and follows southeastern towards northern trend. The aeolian dune facies follow a southeastern to northwestern trend throughout the research domain.

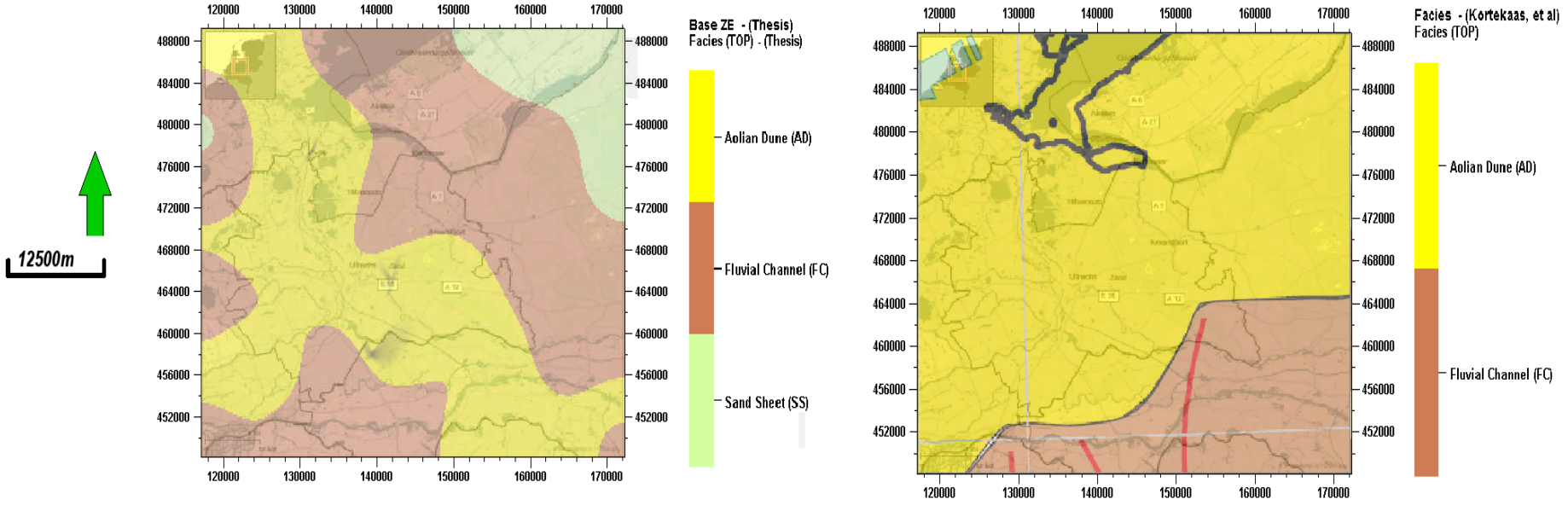

Figure 52: Right: The facies map as retrieved from Kortekaas, M. (2023) [**23**], left: The map based on this thesis of the formation it's top facies map.

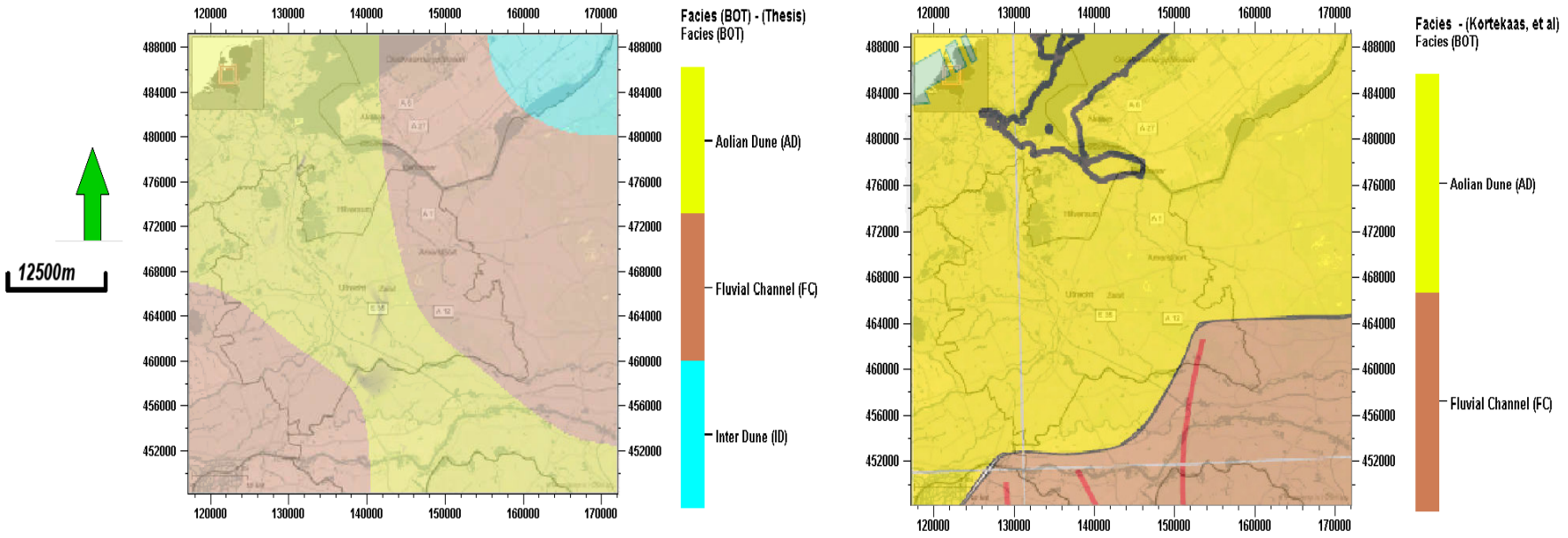

Figure 53: Right: the facies map as retrieved from Kortekaas, M. (2023) [**23**], and right: The map based on this thesis of the formation it's bottom facies map.

Analysis of facies unit proportions indicates a decrease in the proportion of flood sheet facies units from 38.60 % to 38.00 % from the lower to upper Slochteren, while the proportion of sand sheet facies units increased from 47.40 % to 47.90 % (Figure **54**). Furthermore, during the facies upscaling process from borehole logs to adjacent grid cells, there was a loss in aeolian dune facies unit proportions and an increase in fluvial channel facies unit proportions.

In general, it has to be noted that a significant portion of facies resolution is lost in the upscaling and subsequent stochastic interpolation processes, particularly for aeolian dune, interdune, and fluvial channel facies units.

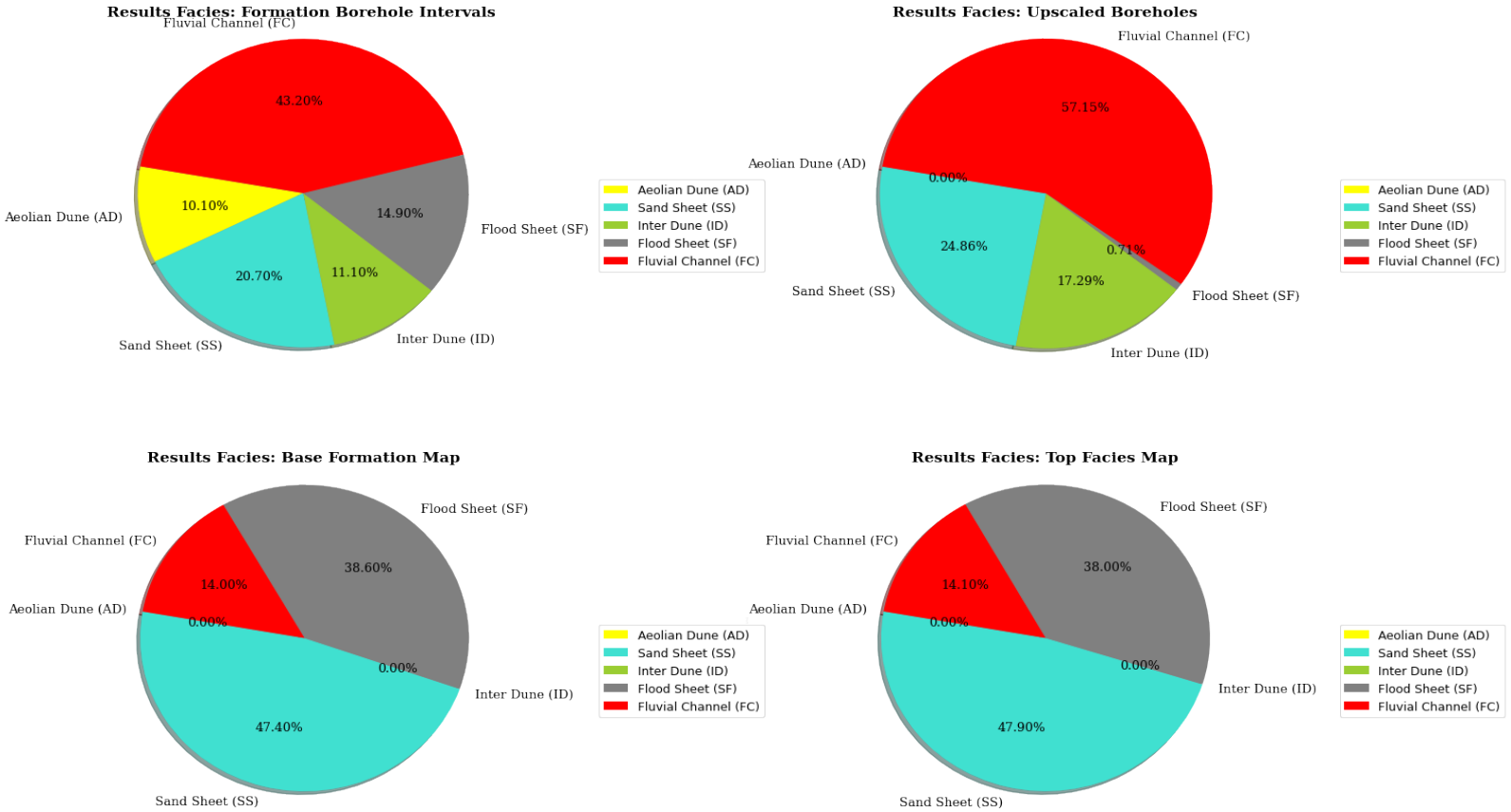

Figure 54: Upper left: pie chart showing the well log facies proportions, upper right: pie chart showing the up-scaled well log facies proportions, lower left: the pie chart showing the bottom formation facies proportions, and lower right: the pie chart showing the top formation facies proportions.

3.5. The High Potential Case Study

Based on the resulting depth, thickness, permeability, and facies distributions of the Upper Slochteren Formation, a high-potential case study area can be identified, for future geothermal development. This area is characterized by favorable surface and geological properties (as illustrated in Figure **55**). The delineated case study area is located north of Amersfoort and covers an area of 12 by 10 km2. The following advantageous surface and geological features are characteristic of this case study area:

Geological Features

- A high average permeability of 149.73 mD.
- A relatively deep average formation top depth of 1791.18 m providing high temperatures suitable for DGE installation.
- An average formation TST of 66.07 m, which is a good reservoir thickness.

Surface Features

- Previously demonstrated heightened interest from the geothermal industry in exploiting and installing DGE.
- The northern district Statdshorst in Amersfoort already has existing heat network infrastructure.
- Multiple renewable energy sources, such as solar- and wind parks, are already installed.
- The city of Amersfoort has a substantial heat demand that DGE can fulfill.

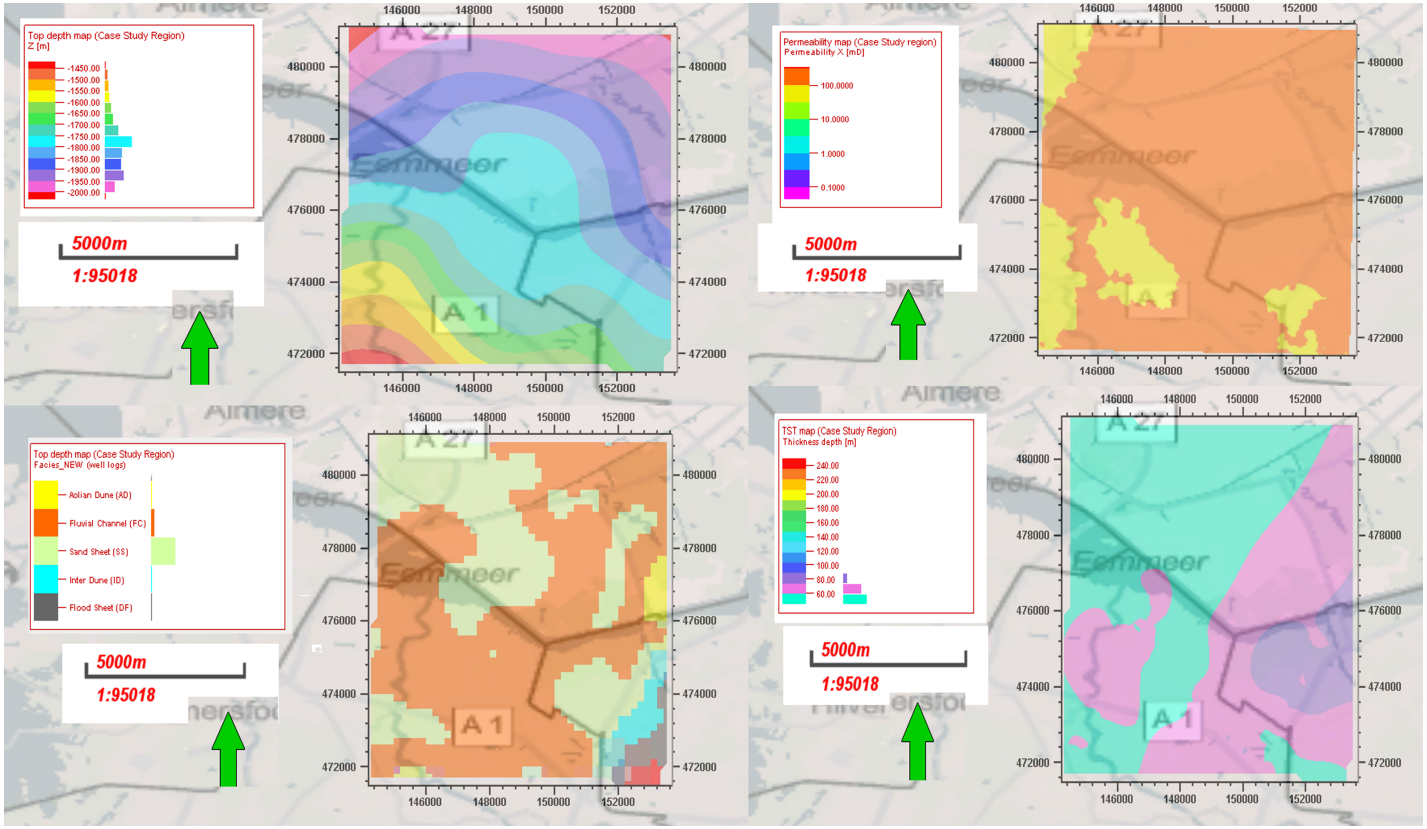

Figure 55: The geothermal high potential case study covers a total surface area of 120 square kilometers. Top left: Top depth map for the Slochteren Formation the case study region. Top right: the formation permeability map for the case study region. Bottom left: Facies map of the Upper Slochteren formation for the case study region Bottom right: TST map for the case study region. white rectangular area: the boundaries of the case study region.

3.6. Limitations of the Geological Model

While writing this chapter, I have identified several uncertainties affecting the accuracy of the generated geological and facies maps for the Slochteren formation. These points of uncertainty are discussed below:

Uncertainty in the 3D Surface Maps
As a consequence of the limited seismic resolution, the BPU and the base Zechstein reflectors couldn't be traced throughout all the seismic 2D sections. Because of these gaps in the seismic sections some uncertainty about the final formation depth and thickness remains. To mitigate this underlying seismic uncertainty from the surface results, it would be helpful to acquire more 2D seismic sections across the study region.

Uncertainty in Upscaling and Distribution of Well Logs
Because of the low well density throughout the research area and the relatively great surface of the research area, a coarse modelled grid cell size was used in the Petrel model. Due to this larger grid cell size, formation data presented along the well logs are not represented when these well logs were up-scaled towards the modelled grid cells. To minimize this reduction in well log information within the geological model results, it would be advisable to attain more well log data from additonal boreholes and a higher resolution model, requiring substantial computing power.

Uncertainty in the Facies Distributions
The facies identified in section **2.3** were determined on the basis of available core material from four wells outside the target area. It may well be that more facies groups exist within the formation. To constrain the dristribution of these different facies, it would be advisable to acquire more core slabs from boreholes.

Uncertainty in the Structural evaluation
Because 3D seismic data are missing across the research area, and the 2D seismic section density is currently still low across the area, it was almost impossible to trace faults and other structural features across the investigated area. For this reason, it was decided not to make a regional structural model of the formation. Large-scale faults were identified and included in the geological model by offset of seismic layers from the existing 2D seismic sections. To better constrain regional structures and to construct a structural model of the Upper Slochteren in the region, it would be helpful to acquire more seismic data across the research area.

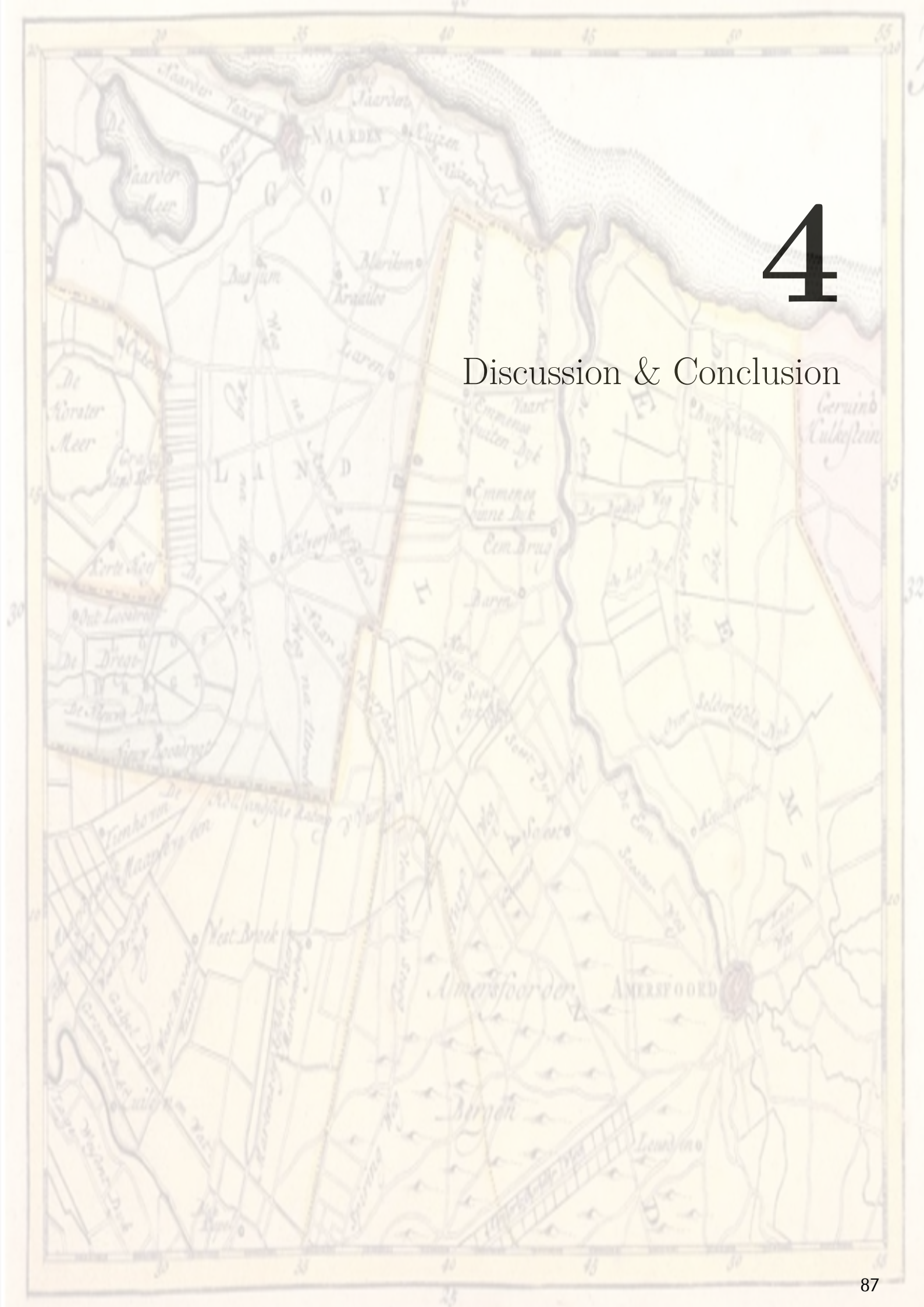

4

Discussion & Conclusion

The analyses and results discussed in the preceding chapters are used to answer the research questions formulated at the beginning of this thesis.

1. WHICH FACIES ARE PRESENT, AND HOW ARE THEY DISTRIBUTED ACROSS THE RESEARCH AREA?

   (a) *What was the paleogeographic distribution at the time of sediment deposition?*

   (b) *How are the reservoir properties of the rock related to the depositional environment?*

WHICH FACIES ARE PRESENT, AND HOW ARE THEY DISTRIBUTED ACROSS THE RESEARCH AREA?
The following facies are presented within the Upper Slochteren Formation across the research area: Flood Sheet (FS), Inter Dune (ID), Aeolian Dune (AD), Fluvial Channel (FC), and Sand Sheets (SS). For the facies distribution at the bottom of the formation as presented from the facies map in subsection **3.3.4**, the inter dune facies are presented in the northeast of the research region. Also, both fluvial channel and aeolian facies are followed by a southeastern towards northwestern trend across the map, and are presented within the remaining part of the study area. For the facies distribution at the top of the formation, the sand sheet facies are presented within the northwest and west of the research area. In addition, the fluvial channel and aeolian facies are followed by a southeastern to northwestern trend throughout the study area.

To better understand the distribution of regional facies in the research area, it would be helpful to study multiple outcrops of the Upper Slochteren Formation. However, since the available outcrops of the formation are sparse and not present in the Netherlands, only some in Polen and/or Germany are presented and can be used.

How did the paleogeographic distribution look at the time of sediment deposition?
At the time of the Early Permian, due to a warm and arid climate, a low supply of Slochteren Sediment from the Southern Variscan Orogenic Belt was accommodated Northward within the SPB. The coarser less sorted sediment is deposited near the Variscan Orogenic Belt at the southern edge of the research area, whereas finer well sorted sediment is deposited further north within the research area. These heavier coarser sediments with less sorting were carried through fluvial channels into the region SPB, which were reworked as needed, further carried north by wind and deposited as dunes towards the northern part of the research domain.

How are the reservoir properties of the rock related to the depositional environment?
Since these facies are related to their reservoir rock properties, however, some limitations arise when linking their properties to the regional depositional environment. Because, these facies are characterized by these reservoir properties, as well as by their original depositional environment at the Upper Permian. However, during the burial phase of these sediments alternations of reservoir properties may occur and therefore alternations within reservoir properties due to these burial events. Which implies that the reservoir properties are only partly related to the regional Upper Permian depositional environment.

5

Recommendations

During the preparation of this script, various topics were not further investigated and were disregarded due to a lack of time and available data. Consequently, these subjects remain unexplored and serve as avenues for future research in geothermal exploration in the Province of Utrecht. These topics are described below:

Future Seismic Acquisition Strategies

Because of the portrayed gaps alongside the seismic horizon interpretations as previously pointed out, the kriging algorithm didn't manage to harness the full attainable array of interpreted data points on behalf of the formed surfaces. Consequently, discrepancies are institute across these surfaces, which subsequently diminishes the accuracy of the emanated maps (see Section **3.4**). To mitigate this uncertainty, foreseen seismic acquisitions across prospected geothermal sites could provide a suggestion to address this concern. Employing this above-mentioned strategy along with the attainment of a three-dimensional seismic cube is poised to refine our understanding of the region's geothermal feasibility.

Future Geological Data Acquisitions

Given the limited number of core slabs and core plugs available and considered in this script for the Upper Slochteren Formation throughout the study area, resulting in uncertainty in porosity and permeability distributions, it is recommended to acquire a large number of core plugs and a significant core slab interval during future geothermal exploration drilling in the area. Additionally, as uncertainty remains about the distribution of the Hellevoetsluis Formation throughout the study area and the permeability of its formation top interval, it is advisable to acquire core plugs and core slab intervals from this formation during these exploration drillings.

Prospective Core & Log Assessments

Due to the limited availability of water samples of the formation and because these samples provide information about the fluid's salt content and the formation's water resistivity, it is recommended to collect multiple water samples during future exploration drillings to determine the water saturation distributions of the target formation with increased accuracy. Additionally, to gain more knowledge about the effects of burial on the reservoir properties of the Upper Slochteren sediment, it is advised to take a quantity of thin section samples from both the current formation core slabs and the future core slabs and subsequently examine them.

Besides the aforementioned, it's imperative to place significant emphasis on the realized geological attribute divisions, as well as to assess the three-dimensional fracture configuration of the reservoir. Hence, it could be appropriate to conduct borehole image logs along with flowmeter logs as integral parts of subsequent geothermal drilling efforts. This will allow for the existing subsurface model to be supplemented by a fracture pattern in conjunction with an upgraded permeability evaluation, which serving as indicators for improved surveying of the area's prospected geothermal resource site.

Future Geothermal Infrastructure

To fully meet the heat demand of the built environment around and in Amersfoort with DGE, it is recommended to provide both the industrial and built environments with a heat network infrastructure in the early stages of the future geothermal project.

During the winter seasons, when the demand for heat is higher compared to the summer seasons when the heat demand is lower, a peak heat supply from the geothermal source will be necessary. This supply might be lower than the peak heat demand during extreme winter days. To bridge this gap between demand and supply, a secondary geothermal storage source would be required. This would allow the excess heat produced during summer to be stored and utilized during these extremely cold winter days.

Future Energy and Economic Analyses

To further elaborate on the results and the formation's geothermal potential based on this thesis and the 3D reservoir model, it is recommended to investigate both energy and economic scenarios using a dynamic simulation program. With the assistance of these simulation results, investors can select the most efficient geothermal setup, which would represent the most promising geothermal energy system for the Province of Utrecht.

Biography

[1] Archie, G. E. (1942). 'The electrical resistivity log as an aid in determining some reservoir characteristics'.*Transactions of the AIME, 146*(01), 54-62, DOI: https://doi.org/10.2118/942054-G

[2] Arps, J. J. (1953). 'The effect of temperature on the density and electrical resistivity of sodium chloride solutions'. *Journal of Petroleum Technology,5*(10), 17-20, DOI: https://doi.org/10.2118/953327-G

[3] Baker, O. R, Yarranton, H.W & Jensen, H. (2015). *Practical reservoir engineering and characterization. Gulf Professional Publishing*. Waltham, US, Openhole Well Logs - Log Interpretation Basics, 297-338, ISBN: 978-0-12-801811-8.

[4] Békési, E., et al. (2020). 'An updated geothermal model of the Dutch subsurface based on inversion of temperature data'. *Geothermics, 88*, 101880, DOI: https://doi.org/10.1016/j.geothermics.2020.101880

[5] Bell, J.S. (1990). 'Investigating stress regimes in sedimentary basins using information from oil industry wireline logs and drilling records'. *Geological Society, London, Special Publications, 48*(1), 305-325, DOI: https://doi.org/10.1144/GSL.SP.1990.048.01.26

[6] Berger, D. L. (1992). *Lithologic properties of carbonate-rock aquifers at five test wells in the Coyote Spring Valley area, southern Nevada, as determined from geophysical logs*. 91(4167). US Department of the Interior, US Geological Survey.

[7] Boker, U & Leo, C. (2021, 8 Oktober). Provincie Utrecht Geothermie Potentieel [PowerPoint-slides]. PANterra. Available at: https://www.stateninformatie.provincie-utrecht.nl/documenten/Ingekomen-stukken-van-GS-naar-PS/20211207-bijlage-1-1-Regionale-potentiestudie-aardwarmte-geothermie-provincie-Utrecht-van-bureau-PanTerra.pdf (Accessed: 28-10-2024).

[8] Buckles, R.S. (1965, May). 'Correlating and Averaging Connate Water Saturation Data', *Journal of Canadian Petroleum Technology, 4*(01), 42-52, DOI: https://doi.org/10.2118/65-01-07

[9] Buijze, L., et al. (2019). 'Review of induced seismicity in geothermal systems worldwide and implications for geothermal systems in the Netherlands'. *Netherlands Journal of Geosciences, 98*, e13, DOI: https://doi.org/10.1017/njg.2019.6

[10] Bush, R. E., & Mardock, E. S. (1951). 'The quantitative application of radioactivity logs'.*Journal of Petroleum Technology, 3*(07), 191-198, DOI: https://doi.org/10.2118/951191-G

[11] Catinat, M., et al. (2023). 'Characterizing facies and porosity-permeability heterogeneity in a geothermal carbonate reservoir with the use of NMR-wireline logging data'. *Geothermics, 115*, 102821, DOI: https://doi.org/10.1016/j.geothermics.2023.102821

[12] Clavier, C., Hoyle, W., & Meunier, D. (1971). 'Quantitative interpretation of thermal neutron decay time logs: part I. Fundamentals and techniques'. *Journal of Petroleum Technology, 23*(06), 743-755, DOI: https://doi.org/10.2118/2658-A-PA

[13] Van Dalfsen, W., Doornenbal, J. C., Dortland, S., & Gunnink, J. L. (2006). 'A comprehensive seismic velocity model for the Netherlands based on lithostratigraphic layers'.*Netherlands Journal of Geosciences, 85*(4), 277-292, DOI: https://doi.org/10.1017/S0016774600023076

[14] Duin, E. J. T., Doornenbal, J. C., Rijkers, R. H., Verbeek, J. W., & Wong, T. E. (2006). 'Subsurface structure of the Netherlands-results of recent onshore and offshore mapping'. *Netherlands Journal of Geosciences, 85*(4), 245, DOI: https://www.nlog.nl/en/media/3006

[15] Fertl, W. H. (1975, June). Shaly sand analysis in development wells. *In SPWLA Annual Logging Symposium (pp. SPWLA-1975). SPWLA*. Denver, Colorado, June 9-12.

[16] Geluk, M. C. (2005, 24 February). *Stratigraphy and tectonics of Permo-Triassic basins in the Netherlands and surrounding areas [Doctoral thesis]*. Faculty of Geosciences, Utrecht University, DOI: file:///C:/Users/awhey/Downloads/full.pdf.

[17] Glennie, K. W. (2010). *Desert sedimentary environments*. e1, Amsterdam, Elsevier, ISBN: 9780080869254

[18] Glover, P. (2024). Formation Evaluation MSC Course Notes Paul Glover PDF. Available at: https://pdfcoffee.com/formation-evaluation-msc-course-notes-paul-glover-pdf-pdf-free.html (Accessed: 29-10-2024).

[19] Gonzalez, O. (2012). GeolOil - Water saturation equations: Archie, Simandoux, Indonesia, Fertl, and SW ratio. Available at: https://geoloil.com/computingSW.php (Assessed: 28-10-2024).

[20] Grötsch, J., & Gaupp, R. (2011). *The Permian Rotliegend of the Netherlands*. SEPM Society for Sedimentary Geology, 98, ISBN: 978-1-56576-300-5

[21] Kay, W. (1936). 'Gases and vapors at high temperature and pressure-density of hydrocarbon'. *Industrial & Engineering Chemistry, 28*(9), 1014-1019,
DOI: https://pubs.acs.org/doi/pdf/10.1021/ie50321a008

[22] Kombrink, H., et al. (2012). 'New insights into the geological structure of the Netherlands; results of a detailed mapping project'. *Netherlands Journal of Geosciences,91* (4), 419-446, DOI: https://www.nlog.nl/sites/default/files/kombrinketal.%20%282012%29.pdf

[23] Kortekaas, M. (2023, 16 November). Atlas of Deep Subsurface Resource In The Netherlands [PowerPoint-slides]. GEODE . Available at: https://www.ebn.nl/wp-content/uploads/2023/11/52023.11.16GEODE-Rotliegend Exploration-DayMarloes-Kortekaas.pdf (Assessed: 29-10-2024).

[24] Kurtz, A. D. (2013). *Determining Mineralogy from Traditional Well Log Data (Doctoral thesis, Marietta College)*. Available at : http://rave.ohiolink.edu/etdc/view?acc num=marhonors1366902854 (Accessed: 31-10-2024).

[25] Larionov, V.V. (1969). Borehole Radiometry Moscow, U.S.S.R. In: Nedra, M.R.L. and Biggs, W.P., Eds., Using Log-Derived Values of Water Saturation and Porosity, *Trans. SPWLA Ann. Logging Symp*. Paper, 10, 26.

[26] Leveaux, J., & Poupon, A. (1971). 'Evaluation of water saturation in shaly formations'.*The Log Analyst, 12*(04), 1-2.

[27] van Lochem, H., Ter Borgh, M., & Mijnlieff, H. (2021, October). 'Regional Geological Evaluation for the SCAN Geothermal Exploration Campaign, the Netherlands'. *In 82nd EAGE Annual Conference & Exhibition* (Vol. 2021, No. 1, pp. 1-5). European Association of Geoscientists & Engineers.

[28] Mckie, T. (2011). 'A comparison of modern dryland depositional systems with the Rotliegend Group in the Netherlands'. *PM Special Publications, 98*, 89-103, DOI: https://doi.org/10.2110/pec.11.98.0089

[29] Mijnlieff, H. F. (2020, March 19). 'Introduction to the geothermal play and reservoir geology of the Netherlands'. *Netherlands Journal of Geosciences, 99*, e2.DOI :10.1017/njg.2020.2

[30] Nieto, A.J., Yale, D.P., & Evans, R.J. (n.d.). 'Core Compaction Correction - A Different Approach'. *Society of Core Analysts*, 139-155, DOI: https://jgmaas.com/SCA/1990/SCA1990-07EURO.pdf

[31] Peters, E. J. (2012). *Advanced Petrophysics: Geology, porosity, absolute permeability, heterogeneity, and geostatistics*. Greenleaf Book Group, 04, ISBN: 978-1936909445

[32] Ponk, et al.(2010). Inventarisatie Bovenste Slochteren Laag voor Geothermische Energie Provioncie van Utrecht. Available at: file:///C:/Users/awhey/Downloads/Potentieonderzoek %20geothermie%20Noord-Holland%20en%20Flevoland%202022%20-%20Publieksrapportage.pdf (Accessed: 30-10-2024).

[33] Priddy, C. L., & Clarke, S. M. (2021). 'Spatial variation in the sedimentary architecture of a dryland fluvial system'. *Sedimentology, 68*(6), 2887-291, DOI: https://doi.org/10.1111/sed.12876

[34] Rehling, J., Zaalberg-Metselaar, G., ter Borgh, M., & Siemerink, E. (2020, October). 'The Dutch SCAN Geothermal Data Acquisition Program—Current status and future plans'. *In SEG International Exposition and Annual Meeting (p. D021S020R001)*. SEG.

[35] Rijks Geologische Dienst. (1983 March). Inventarisatie van de Upper Rotliegend Group (Slochteren Sandstone Formation) in Nederland t.b.v. de winning van aardwarmte. Available at: https://www.nlog.nl/sites/default/files/1983%2083ds05ex%20inventarisatie %20upper%20rotliegend%20group %20t.b.v.%20aardwarmte.pdf (Assessed: 29-10-2024).

[36] Schowalter, T. T. (1979). 'Mechanics of secondary hydrocarbon migration and entrapment'. *AAPG bulletin, 63*(5), 723-760, DOI: https://www.searchanddiscovery.com/documents/97018/mechan.htm28p

[37] Stieber, S. J. (1970, October). 'Pulsed neutron capture log evaluation-Louisiana Gulf Coast'. *In SPE Annual Technical Conference and Exhibition (pp. SPE-2961)*. SPE.

[38] Tiab, D., & Donaldson, E. C. (2024). *Petrophysics: theory and practice of measuring reservoir rock and fluid transport properties*. Elsevier. ISBN: 9780123838483.

[39] Tittman, J., & Wahl, J. S. (1965). 'The physical foundations of formation density logging (gamma-gamma)'.*Geophysics, 30*(2), 284-294, DOI: https://doi.org/10.1190/1.1439574

[40] TNO-GDN. (2017). Hellevoetsluis Formation. Available at: https://www.dinoloket.nl/en/' stratigraphic-nomenclature/hellevoetsluis-formation (Accessed: 30-10-2024).

[41] TNO-GDN. (2019). Lower Claystone Member. Available at: https://www.dinoloket.nl/en/stratigraphic-nomenclature/lower-claystone-member (Accessed: 30-10-2024).

[42] TNO. (2015, 27 January). Integrated pressure information system for the onshore and offshore Netherlands Final report. Available at: https://www.nlog.nl/sites/default/files/2020-05/TNO-Report-2015-R10065-final-public2020.pdf (Accessed: 30-10-2024).

[43] Vrijlandt, M. A. W., et al. (2019, June). 'ThermoGIS update: a renewed view on geothermal potential in the Netherlands'. *In Proceedings of the European Geothermal Congress, 10*.

[44] Worthington, P. F. (1993). 'The uses and abuses of the Archie equations, 1: The formation factor-porosity relationship'. *Journal of Applied Geophysics, 30*(3), 215-228, DOI: https://doi.org/10.1016/0926-9851(93)90028-W

[45] Wyllie, M. R. J., Gregory, A. R., & Gardner, L. W. (1956). 'Elastic wave velocities in heterogeneous and porous media'.*Geophysics, 21*(1), 41-70, DOI: http://dx.doi.org/10.1190/1.1438217

[46] Wyllie, M. R. J., & Rose, W. D. (1950). 'Some theoretical considerations related to the quantitative evaluation of the physical characteristics of reservoir rock from electrical log data'.*Journal of Petroleum Technology, 2*(04), 105-118, DOI: https://doi.org/10.2118/950105-G

[47] Zoback, M. D., Moos, D., Mastin, L., & Anderson, R. N. (1985). 'Well bore breakouts and in situ stress'.*Journal of Geophysical Research: Solid Earth, 90*(B7), 5523-5530, DOI: https://doi.org/10.1029/JB090iB07p05523

A

Appendices

A.1. Appendix The Borehole Correlation Trajectories

To illustrate the correlation trajectories of borehole combinations ALE-01-JUT-01, WSP-01-ALE-01, and BLA-01-WRV-01 as described and (as presented in Section **2.2**), their respective correlation trajectories have depicted (as illustrated in Figures **56**, **62**, & **59**).

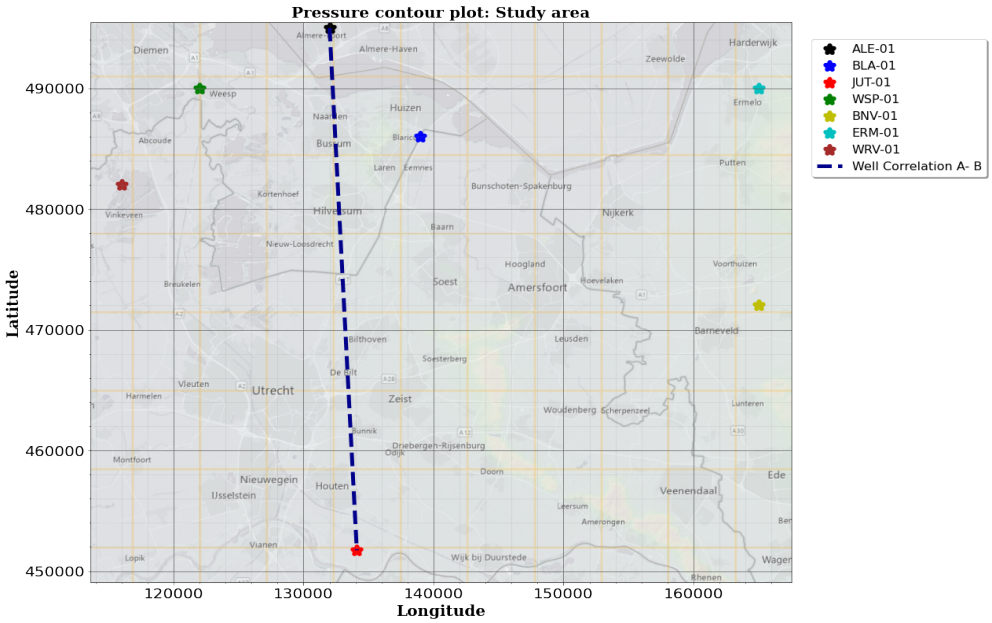

Figure 56: Thick bold line: The well trajectory for the well correlation of borehole combination JUT-01-ALE-01.

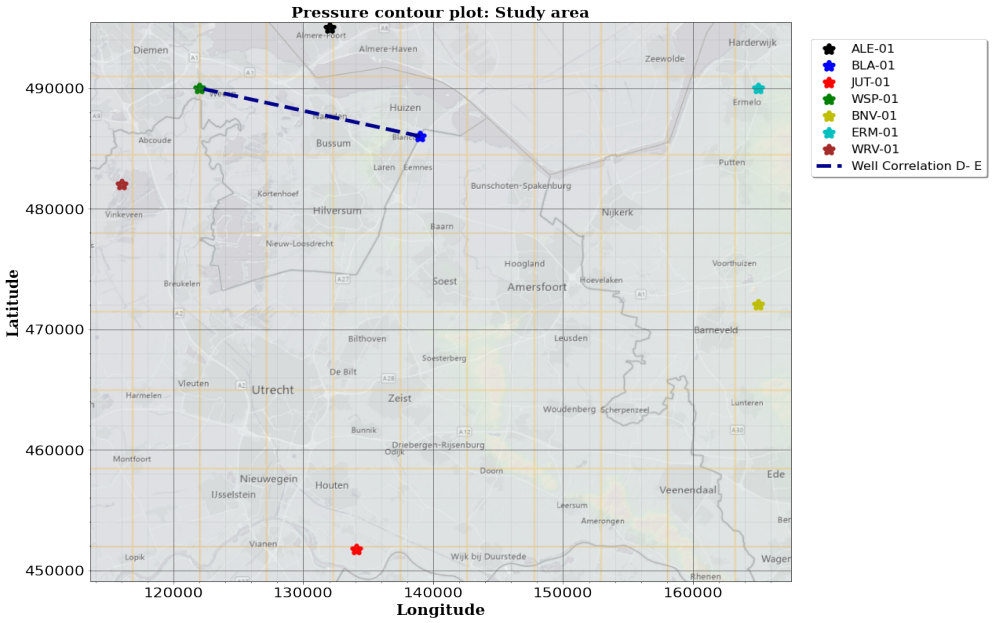

Figure 57: Thick bold line: The well trajectory for the well correlation of borehole combination WSP-01-BLA-01.

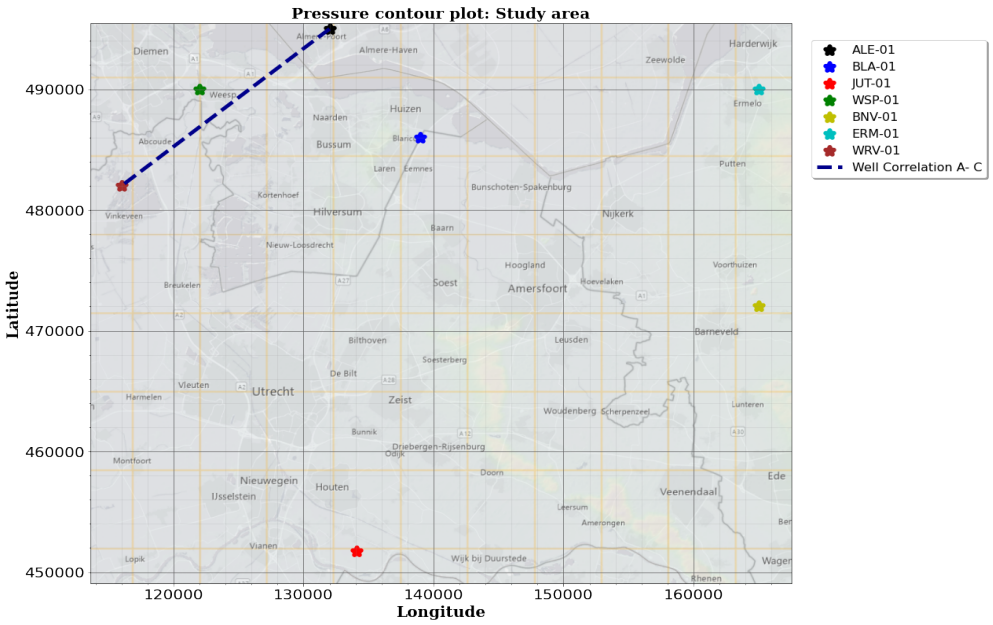

Figure 58: Thick bold line: The well trajectory for the well correlation of borehole combination JUT-01-ALE-01.

A.2. Appendix -The Core Slab Lithostratigrahic Columns

As mentioned in Section **2.3**, the core slab intervals for wells WSP-01, BNV-01, ERM-01, and JUT-01 have been analyzed for grain size, sorting, sedimentary patterns, and bioturbation distributions. The resulting lithostratigraphic columns have illustrated in Figures **61**, **62**, **59**, & **60**, which have generated by utilizing the SEDlog software.

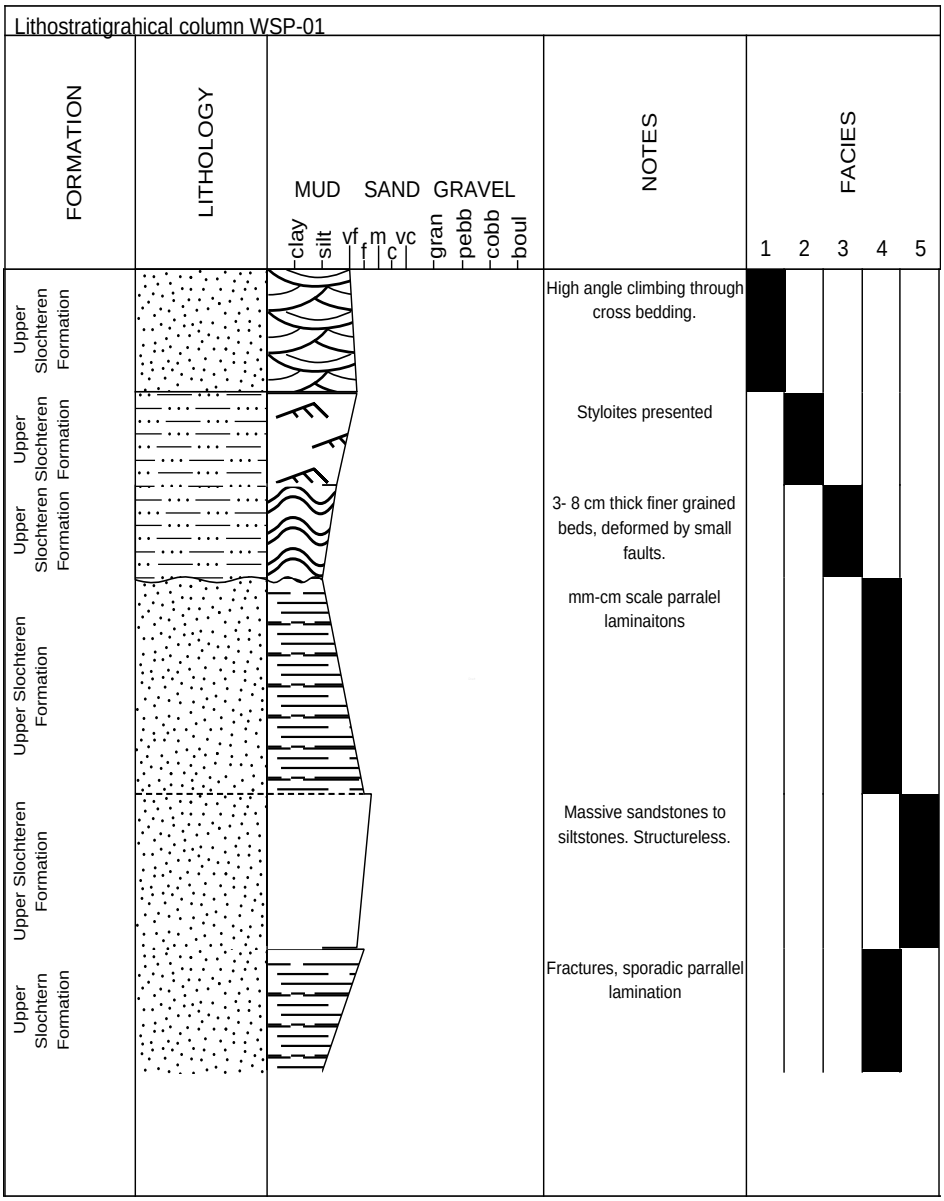

Figure 59: The lithostratigraphic column for the core interval for the borehole WSP-01.

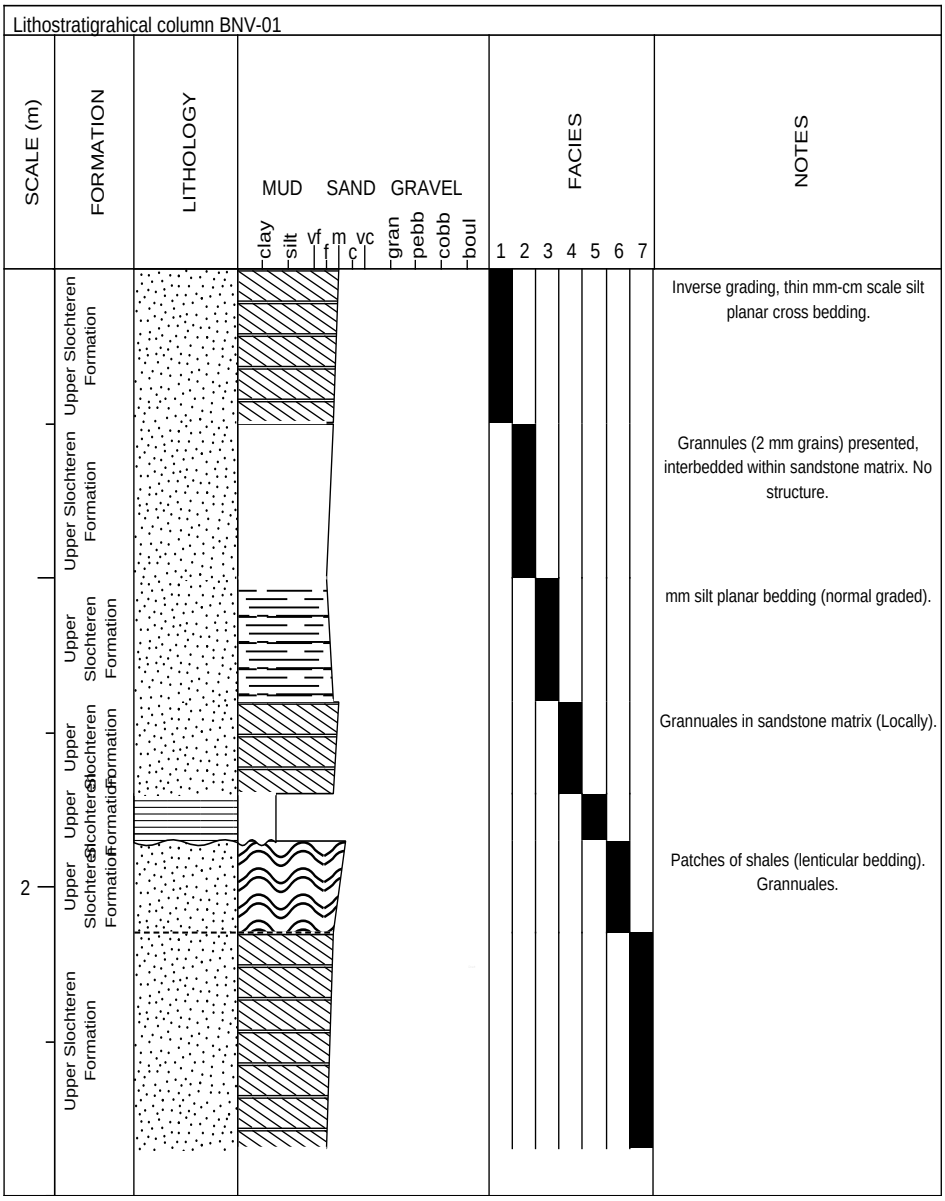

Figure 60: The lithostratigraphic column for the core interval for the borehole BNV-01.

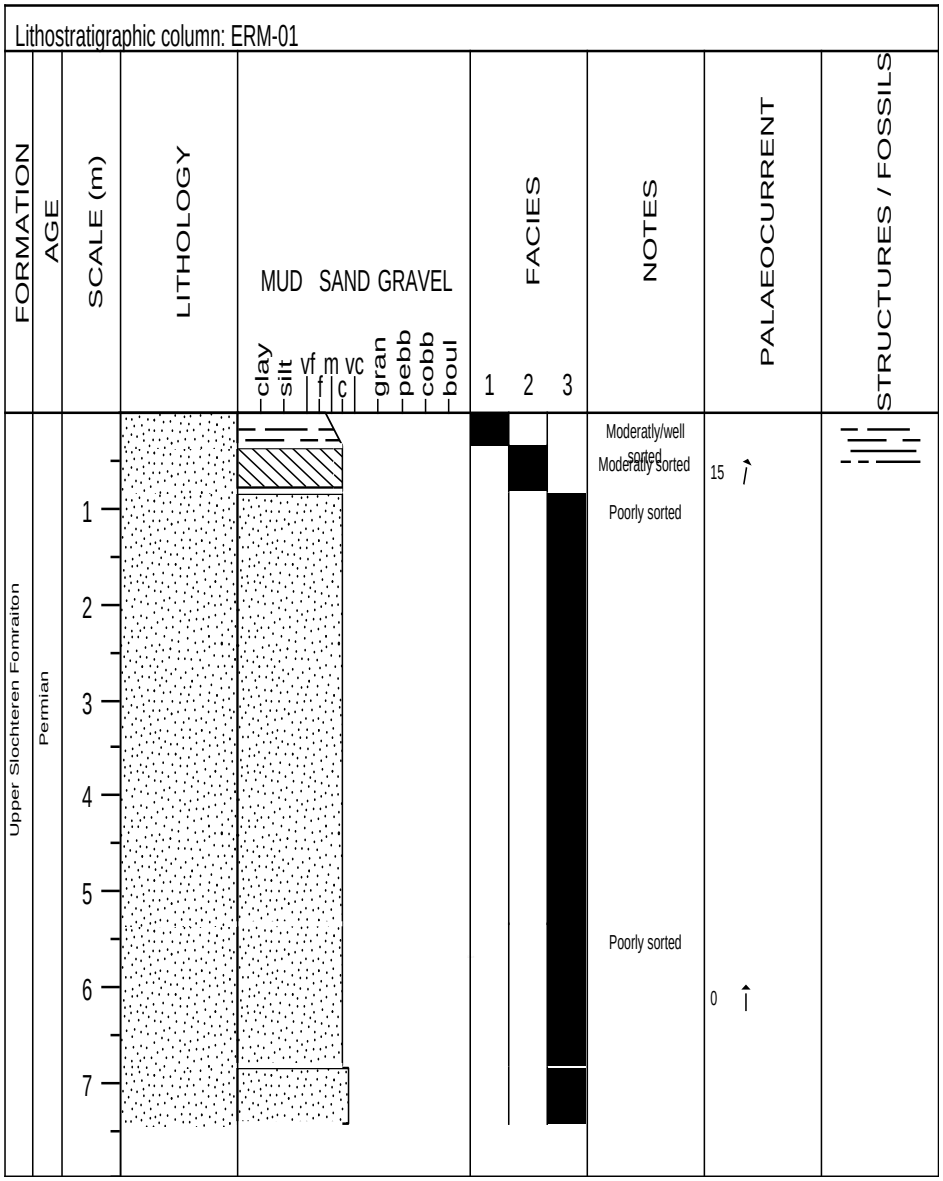

Figure 61: The lithostratigraphic column for the core interval for the borehole ERM-01.

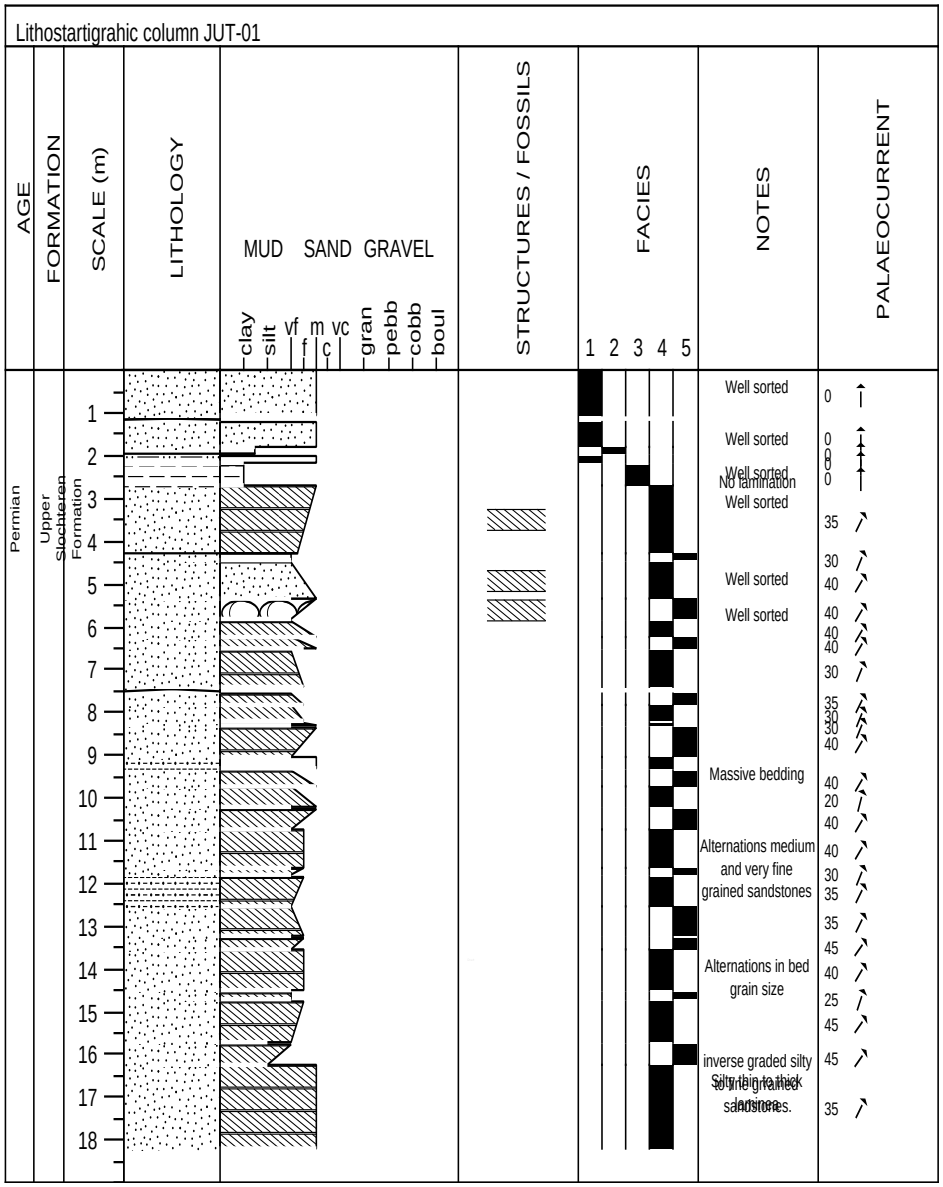

Figure 62: The lithostratigraphic column for the core interval for the borehole JUT-01.

A.3. Appendix -The Lithofacies & Facies Classes

In accordance with Section **2.3**, both lithofacies and facies units as described in Priddy, C. L., & Clarke, S. M. (2021) **[33]** study, have outlined in the corresponding tables (as listed in Tables **18** & **17**).

Table 17: Below are the characteristics of lithofacies as described, gathered from the study by Priddy, C. L., & Clarke, S. M. (2021) [**33**].. The following lithofacies definitions have utilized in the table below: **Sm**: Sub-areal unstructured sandstones, **Smxb**: planar cross-bedded sandstones, **Smtxb**: cross-bedded sandstones, **Smpb**: planar-bedded sandstones, and **Smf**: subaqueous unstructured sandstones. The abbreviations as utilized have defined as follows: vf: very fine, m: medium, f: fine, ws: well-sorted, mo: moderately-sorted.

Lithofacies Class	*Lithology*	*Sedimentary prints*
Sm	vf to m grained sandstones, ws	Unstructered
Smxb	f to m grained sandstones,ws	Planar cross bedded
Smtxb	f to m grained sandstones,ws	Through cross bedded
Smf	m grained sanstones, ms	Unstructered
Sfrl	siltstone to m grained sandstones, ms to ws	Ripple cross laminated
Smpb	f to m grained sandstones,ws	Planar bedded
Sxb	m grained sandstones, ws	Planar cross bedded
Srb	m grained sandstones, mo to ws	Cross bedded
Sfl	m grained sanstones, mo to ws	Flaser laminated

Table 18: The facies units, with their corresponding lithofacies units have derived from the study by Priddy, C. L., & Clarke, S. M. (2021) [**33**] have listed below.

Facies Class	*Morphology*	*Recongnizable Lithofacies*	*Width/thicknesses* $(\frac{W}{T})$ *Ratio*
Aeolian Dune (AD)	Tabular	Smxb, Smtxb	3.00
Sand Sheet (SS)	Tabular	Smpl, Sm	250.00
Inter Dune (ID)	Lensiodal	Sm, Spl,Sfrl	4.00
Fluvial Channel (FC)	U-shaped	Sxb,Spb,Sfrl	15.00
Sheet Flood (SF)	Tabular	Sma, Smf,Sfl, Sfrl	100

A.4. Appendix D -The Core Slab Facies Classifications

The facies for the core slab intervals of wells JUT-01, WSP-01, BNV-01, and ERM-01 have been classified and summarized in the respective tables (as shown in Tables **19**, **20**, **21**, & **22**).

Table 19: Below the lithofacies and facies for the core interval for borehole ERM-01 have classified and listed.

Lithofacies Class	***Depth top and bottom*** $[m]$	***Grain Size Trend***	***Facies Class***
Smpl	2640.6-2641.2	Finning upward	Aeolian Dune (AD)
Smf	2641.2-2647.5	Finning and coarsening upward	Sheet Flood (F)

Table 20: Below the lithofacies and facies for the core interval for borehole JUT-01 have classified and listed. NA: means the grain size trend has not observed.

Lihtofacies Class	***Depth bottom and top*** $[m]$	***Grain Size Trend***	***Facies Class***
Sm	3256-3258	Na	Sandsheet (SS)
Stpl	3258-3258.4	Coarsening upward	Inter Dune (ID)
Sm	3258.3-3258.8	Coarsening upward	Inter Dune (ID)
Stpl	3258.8-3259.1	Fining upward	Inter Dune (ID)
Smxb	3259.1-3260	Coarsening upward	Aeolian Dune (AD)
Sxb	3260-3261	Coarsening upward	Fluvial Channel (FC)
Smxb	3261-3261.5	Coarsening upward	Aeolian Dune (AD)
Sxb	3261.5-3262	Coarsening upward	Fluvial Channel (FC)
Smxb	3262-3262.6	NA	Aeolian Dune (AD)
Sxb	3262.6-3263	NA	Fluvial Channel (FC)
Sm	3263-3263.4	NA	Sandsheet (SS)
Sxb	3263.4-3264	NA	Fluvial Channel (FC)
Smxb	3264-3264.3	NA	Aeolian Dune (AD)
Sm	3264.3-3264.4	Coarsening upward	Sandsheet (SS)
Sxb	3264.4-3265.2	Coarsening upward	Fluvial Channel (FC)
Smxb	3265.2-3265.9	Coarsneing upward	Aeolian Dune (AD)
Sxb	3265.9-3266.2	Finning upward	Fluvial Channel (FC)
Smxb	3266.2-3266.8	Coarsening upward	Aeolian Dune (AD)
Sxb	3266.8-3267.2	Coarsening upward	Fluvial Channel (FC)
Smxb	3267.2-3269	Fining upward	Aeolian Dune (AD)
Sxb	3269.0-3269.3	NA	Fluvial Channel (FC)
Smxb	3269.3-3270	NA	Aeolian Dune (AD)
Sxb	3270-3272	NA	Fluvial Channel (FC)
Smxb	3272-3272.6	Finning and coarsening upward	Aeolian Dune (AD)
Sxb	3272.6-3273.0	Coarsening upward	Fluvial Channel (FC)
Smxb	3273.0-3274	Finnig upward	Aeolian Dune (AD)

Table 21: Below the lithofacies and facies for the core interval for borehole WSP-01 have classified and listed.

Lihtofacies Class	***Depth top and bottom*** $[m]$	***Grain Size Trend***	***Facies Class***
Smtxb	2192.0-2192.5	Finning upward	Aeolian Dune (AD)
Smf, Sfrl	2192.5-2193.0	Coarsening upward	Sheet Flood (F)
Smpb, Sm	2193.0-2194.0	Finning upward	Sand Sheet (SS)
Smpb	2194.0-2194.7	Coarsening upward	Sand Sheet (SS)

Table 22: Below the lithofacies and facies for the core interval for borehole BNV-01 have classified and listed.

Lihtofacies Class	***Depth top and bottom*** $[m]$	***Grain Size trend***	***Facies Class***
Smxb	3039.0-3039.5	Coarsening upward	Aeolian Dune (AD)
Sfl	3039.5-3040.0	Finning upward	Sheet Flood (F)
Srb,Spb	3040.0-3040.7	Coarsening upward	Inter Dune (ID)
Spb,Smf,Smpb	3040.7-3042.0	Finning upward	Inter Dune (ID)
Smxb	3042.0-3042.9	Coarsening upward	Aeolian Dune (AD)

A.5. Appendix - Caliper Logs

Along five boreholes caliper logs have retrieved from NLOG and have plotted along their formations intervals. It's shown that the borehole diameter is only considerable increased along the bottom formation of borehole WSP-01 (as illustrated in Figure **67**).

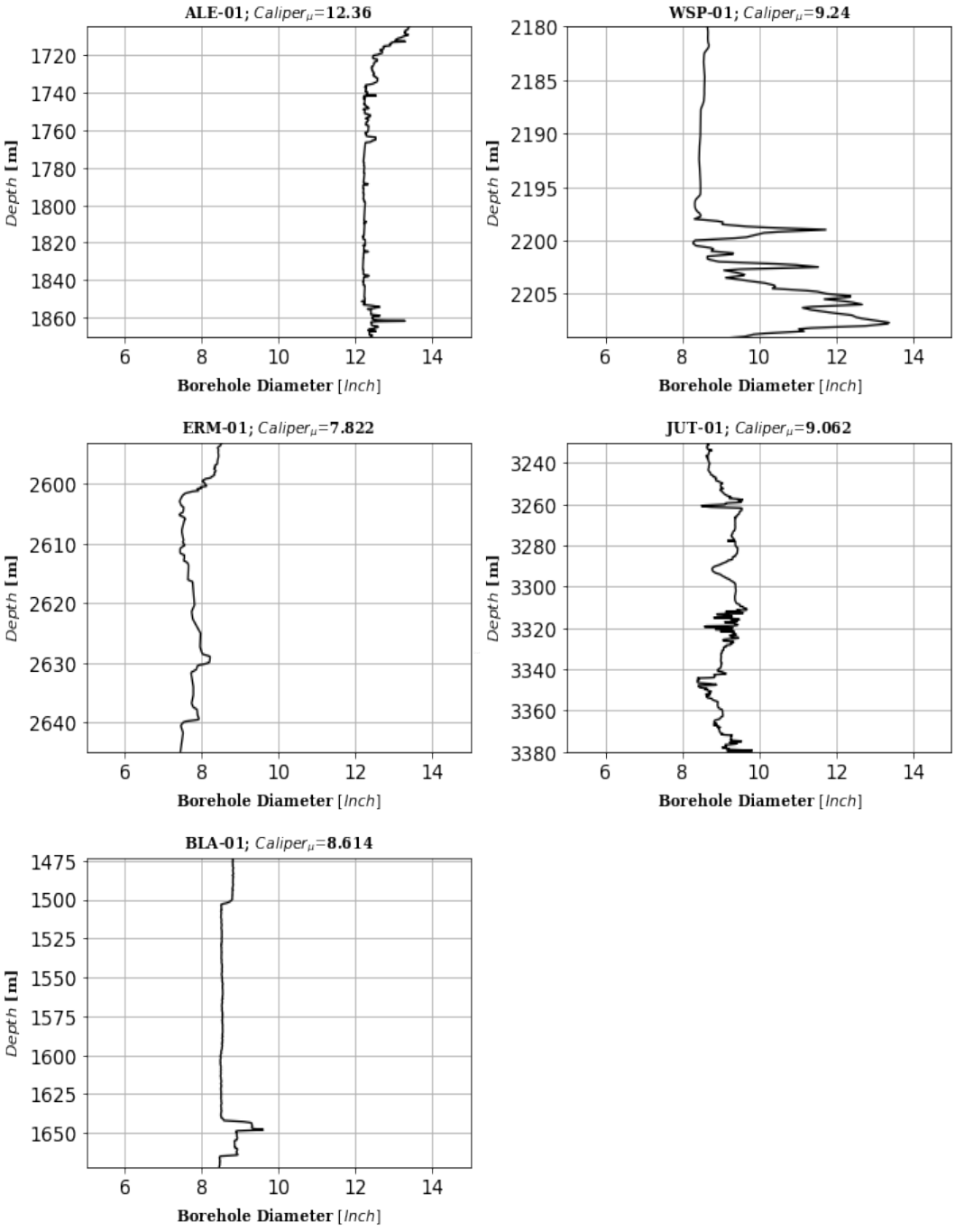

Figure 63: Black curves: the caliper logs along boreholes (ERM-01, WSP-01, ALE-01, BLA-01 & JUT-01) for their formations intervals, as indicated in (see the well information Table **4** as presented in Subsection **2.1**).

A.6. Appendix - The Gas Density Determination

Based on average reservoir temperature and pressure estimations along boreholes ALE-01 & BLA-01 (as presented in Subsection **2.4.5**). The formation it's gas compressibility factor has determined based on utilizing the gas diagrams, as retrieved from Schowalter, T. T. (1979) **[36]**. and (as presented in Figures **64** & **65**). Based on this value and the corresponding gas gravity as previously estimated the gas density has determined, by utilizing the diagram as shown in (Figure **66** from Schowalter, T. T. (1979) **[36]**).

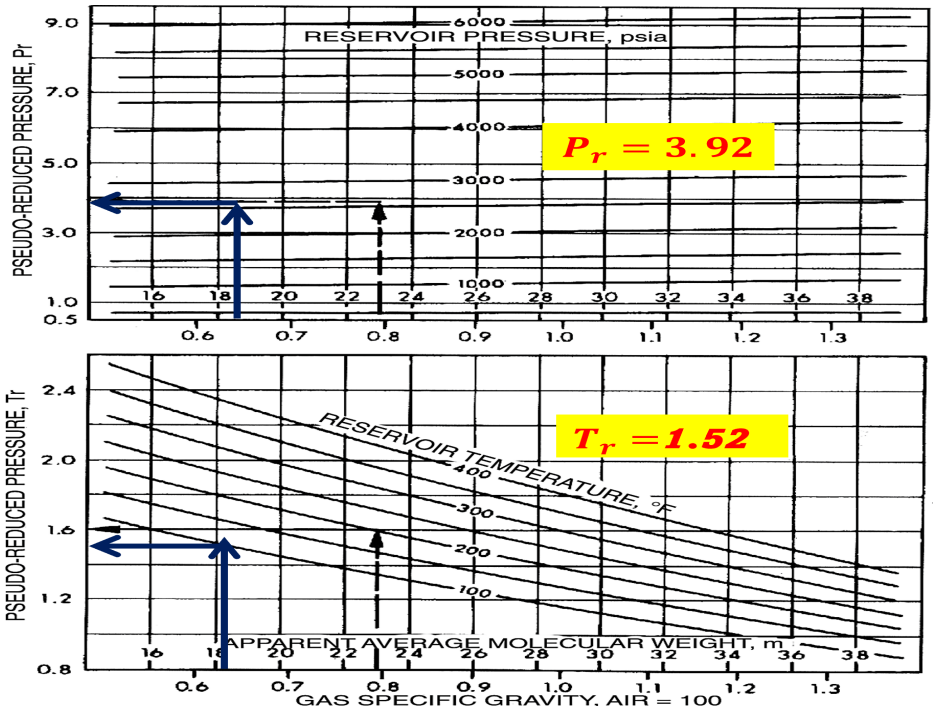

Figure 64: Schowalter, T. T. (1979) [**36**] diagram to estimate the formation it's psuedo-reduced temperature and pressure. Blue thick arrows: the determined pseudo-reduced temperature and pressure.

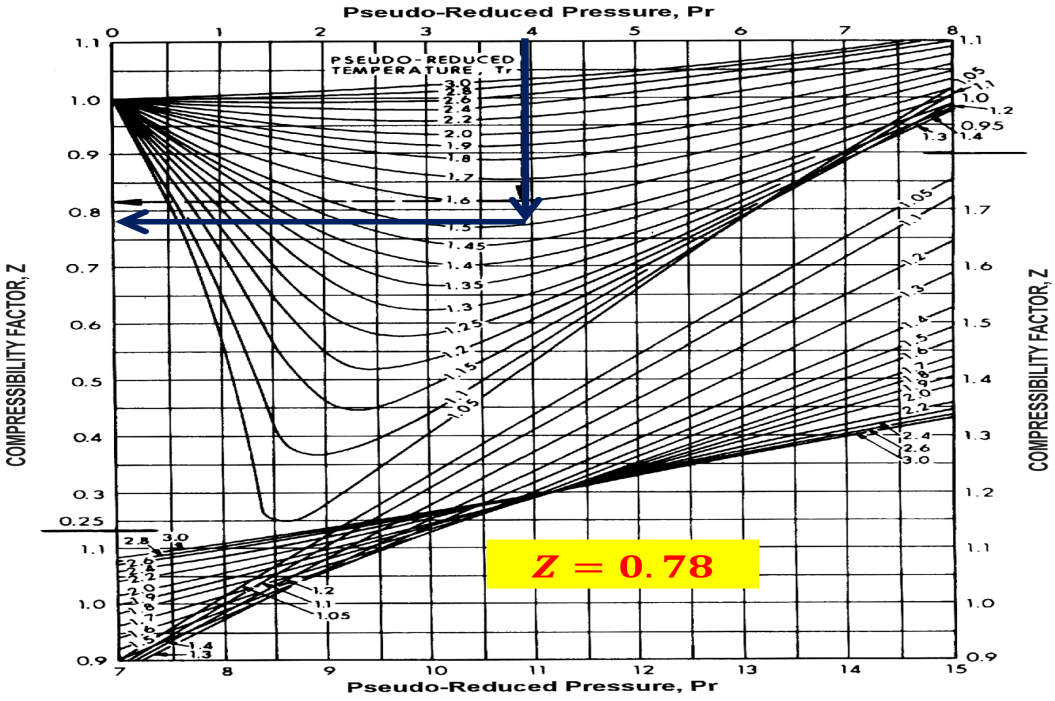

Figure 65: Schowalter, T. T. (1979) [**36**] diagram to estimate the formation it's gas compressibility value. Blue thick arrows: the determined gas compressibility.

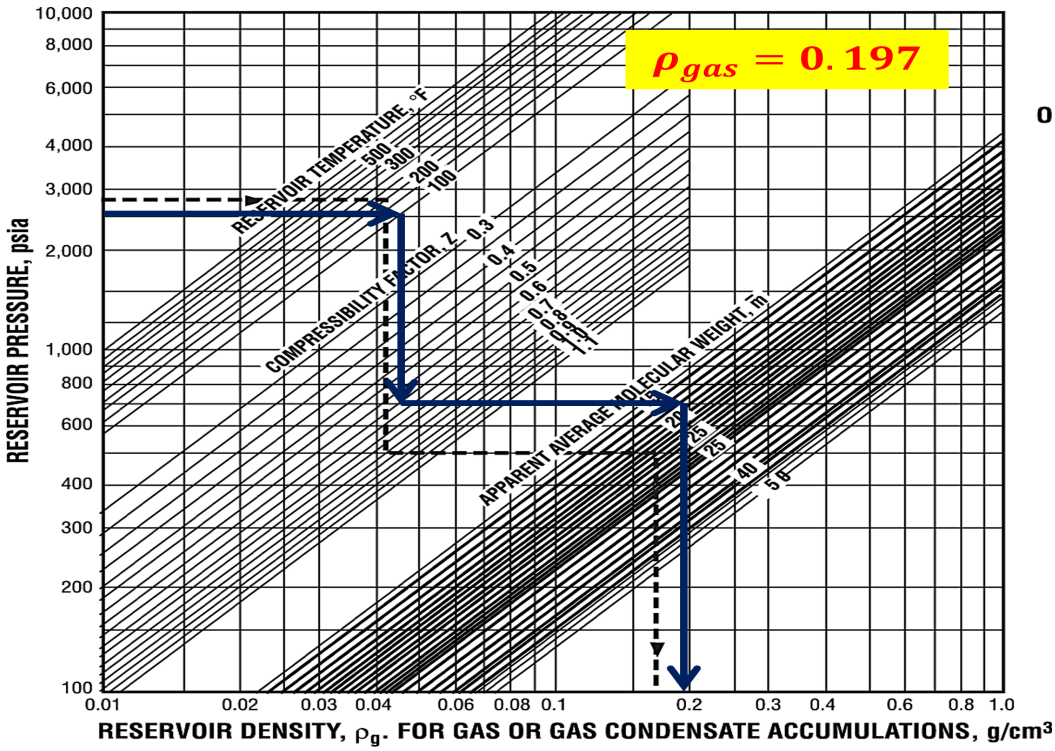

Figure 66: Schowalter, T. T. (1979) [**36**] diagram to estimate the formation it's gas density. Blue thick arrows: the determined gas density.

A.7. Appendix - The RHOB Log Corrections

As previously noted, the determined RHOB log correction factors for the presence of formation gas, has estimated based on Tittman, J., & Wahl, J. S. (1965) **[39]** diagram (as depicted in Figure **67**). Since, the porosity along borehole BLA-01 has indicated to having higher values, in respect to the porosity estimated along well ALE-01. That is the reason why a higher gas density correction has be selected, based on the Tittman, J., & Wahl, J. S. (1965) **[39]** (as presented in Subsection **2.4.7**). Along boreholes with available RHOB logs, the RHOB log has both corrected for the presence of formation shale and formation gas, which resulting logs have illustrated in Figure **68**.

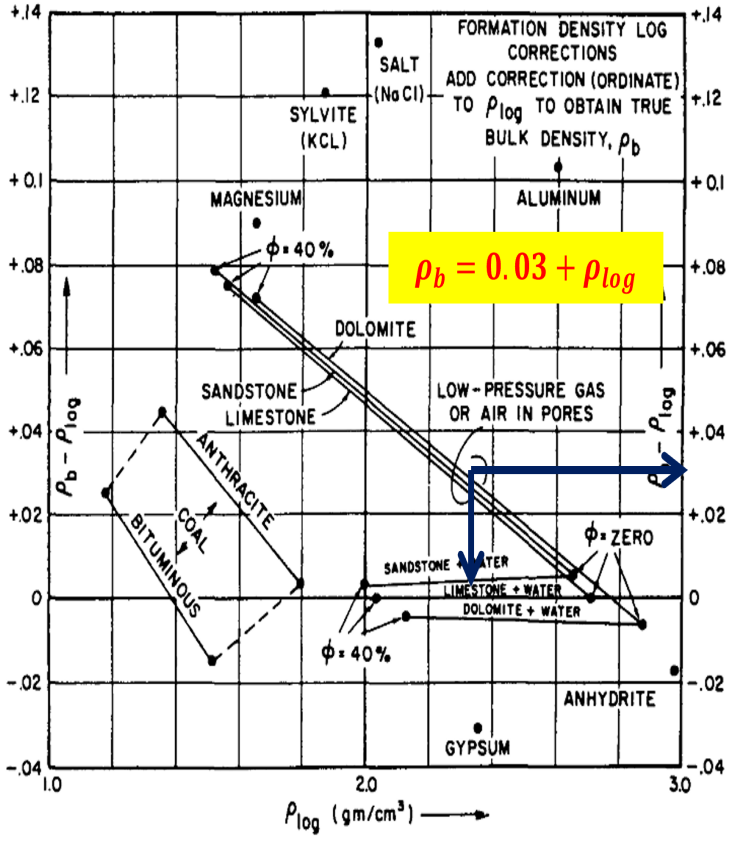

Figure 67: Chart: the Tittman, J., & Wahl, J. S. (1965) [**39**] diagram showing the residual amount of pore gas as function of the bulk density correction factor on the y-axis.

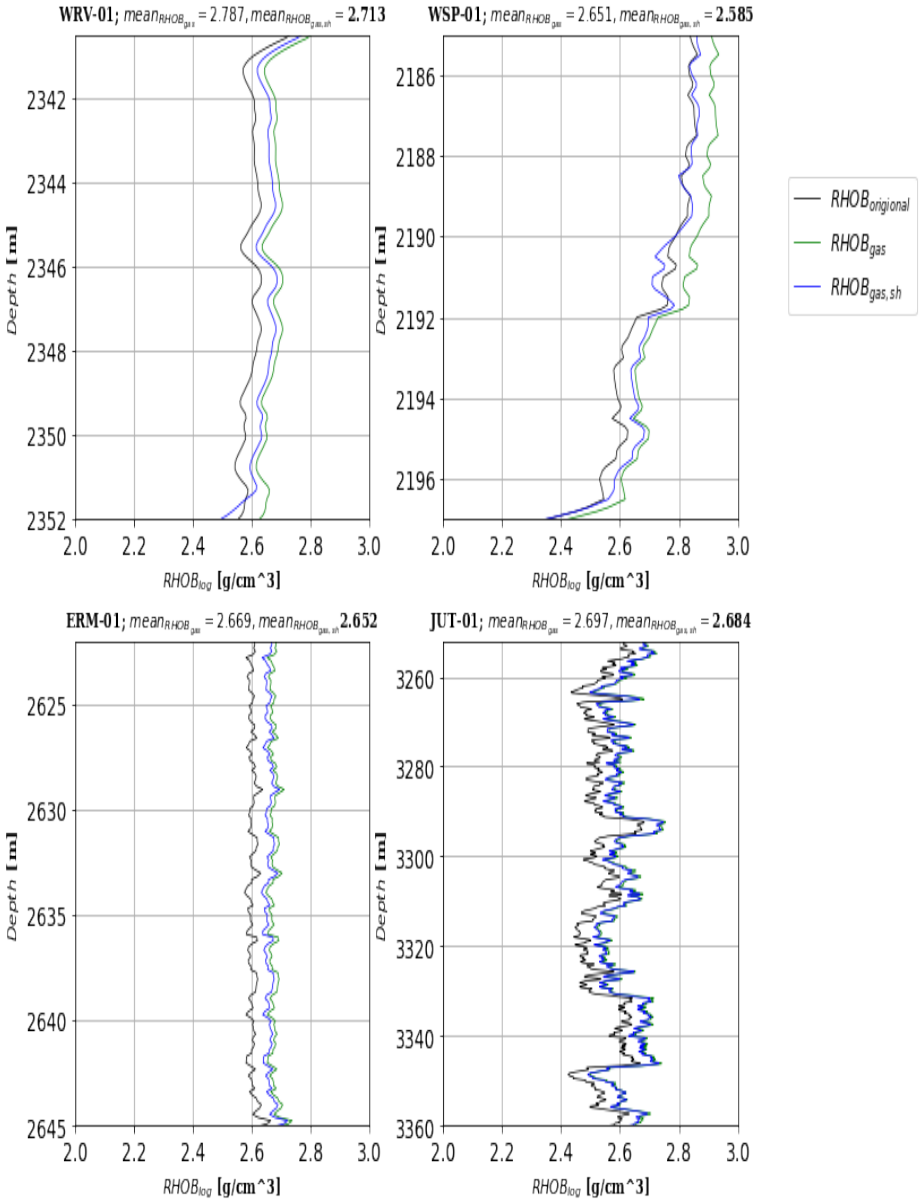

Figure 68: Coloured curves: the original RHOB log, the shale-corrected RHOB log, and the gas and shale corrected RHOB log along the remaining boreholes with available RHOB logs for boreholes WSP-01, WRV-01, ERM-01, and JUT-01.

A.8. Appendix- log Porosity Method Comparison

Several log porosity methods have employed, which have validated against core plug porosity data points along boreholes (ERM-01, BLA-01, & JUT-01), as presented in (See Subsection **2.4.8**). The following porosity log methods have utilized and listed: (absolute and effective) porosity based on the RHOB logs, (absolute and effective) porosity based on the NPHI logs, (absolute and effective) porosity based on the combination of the NPHI logs and DPHI porosity logs, and the (absolute and effective) porosity based on the DT logs.

This Appendix section is divided as follows: firstly, the porosity estimations based on the RHOB log are discussed, secondly, the combined porosity estimations based on the DPHI & NPHI logs are described, subsequently, the porosity estimations solely based on the NPHI log have addressed. Lastly, the porosity estimations based on the DT log has discussed.

The Porosity from the RHOB log

Along the boreholes with available RHOB logs, the absolute porosity, also denoted as the DPHI log, has estimated by utilizing (see Equation **27** from Peters, E. J. (2012) **[31]**. Along boreholes which having available LLD & MSFL logs as for ALE-01, BLA-01, WSP-01, and ERM-01, their estimated DPHI distributions have corrected for the presence of gas by utilizing (see Equation **28** as retrieved from Peters, E. J. (2012) **[31]**. Before the porosity as function of the volume of shale distribution has be validated (as described in Subsection **2.4.8**). The effective DPHI porosity has approximated based on the Clavier, C., et al. (1971) **[12]** volume of clay distribution, by utilizing (see Equation **29** as retrieved from Peters, E. J. (2012) **[31]**.

In Equations **27**, **28**, & **29** the following symbols are defined: ρ_{ma} the density of the sand matrix $[\frac{g}{cm^3}]$ (as listed in Table **7** in Subsection **2.3.4**), ρ_{bc} the corrected clay and gas RHOB log $[\frac{g}{cm^3}]$ (as described in Subsection **2.4.7**), ρ_{fl} the density of the formation brine $[\frac{g}{cm^3}]$ (as indicated in Table **7** in Subsection **2.4.4**), ρ_{bg} the corrected fluid/gas density $[\frac{g}{cm^3}]$, ρ_{mf} the density of the mud filtrate $[\frac{g}{cm^3}]$ (as listed in Table **9**), ρ_{gas} the density of the gas mixture $[\frac{g}{cm^3}]$ (as presented in Subsection **2.4.6**), S_{xo} the mud filtrate saturation (flushed zone) $[-]$, ϕ_D DPHI outcome $[-]$, $\phi_{D_{gas,sh}}$ the corrected gas and shale DPHI log $[-]$, ρ_{sh} the density of the dry clay $[\frac{g}{cm^3}]$ (as noted in Subsection **2.4.4**), and V_{cl} the Clavier, C., et al. (1971) **[12]** volume of clay distribution $[-]$ (as discussed in Subsection **2.4.6**).

$$\phi_D = \frac{\rho_{ma} - \rho_{bc}}{\rho_{ma} - \rho_{fl}} \tag{27}$$

$$\phi_{D_{gas}} = \frac{\rho_{ma} - \rho_{bc}}{\rho_{ma} - (S_{xo} \cdot \rho_{mf} + ((1 - S_{xo}) \cdot \rho_{gas}))} \tag{28}$$

$$\phi_{D_{gas,sh}} = \frac{\rho_{ma} - \rho_{bc}}{\rho_{ma} - \rho_{bg}} - V_{cl} \cdot \frac{\rho_{ma} - \rho_{sh}}{\rho_{ma} - \rho_{fl}} \tag{29}$$

The Combined NPHI log and DPHI log Porosity

The combined effective porosity based on the NPHI log and the DPHI log, has usually estimated based on the so-called NPHI against DPHI cross plot (as shown in Figure **68**). To construct this plot, first the density of the pure shale has estimated, by determining the formation it's bulk density of 2.664 $[\frac{g}{cm^3}]$ which corresponds with the highest GR value (as illustrated in Figure **69**). Subsequently, by linearly extrapolating it's pure shale point towards the line, which connects the dry clay point with the pore fluid point, as a result the wet clay density of 2.569 $[\frac{g}{cm^3}]$ has determined. Their corresponding pure shale and dry clay NPHI points ($NPHI_{shale} = 0.190\ [-]$ and $NPHI_{wet,clay} = 0.267\ [-]$) have determined, based on a linear RHOB log against NPHI log correlation (as denoted in Equation **30**). Based on this linear approximation, the determined dry clay matrix and sand matrix RHOB points have plugged in, to estimate their corresponding NPHI points.

In Equation **30**, the following symbols are defined: ρ_b the shale and gas corrected RHOB distribution $[\frac{g}{cm^3}]$, $NPHI$ the for sandstone- and gas corrected NPHI log $[-]$, a the slope coefficient $[-]$, and b the y-intercept $[-]$.

$$NPHI = \frac{\rho_b + b}{a} = \frac{\rho_b + 3.166}{2.569} \qquad R^2 = 0.999 \tag{30}$$

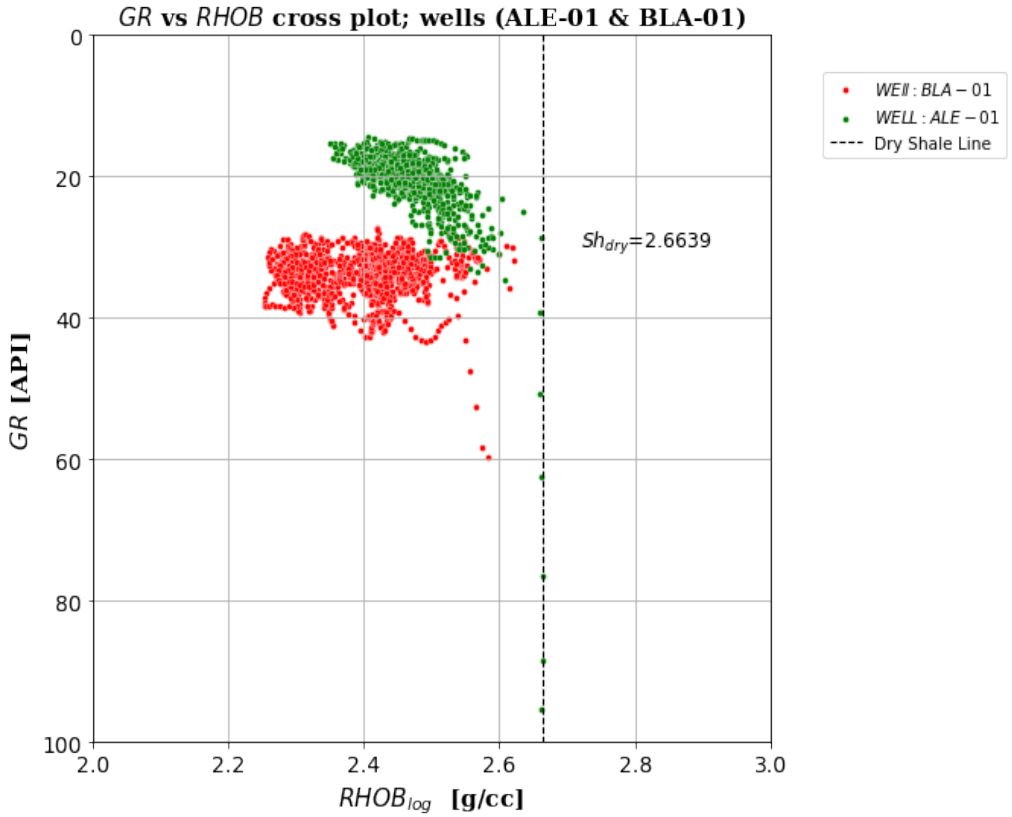

Figure 69: Coloured points: the formation it's GR log against RHOB log data points along the boreholes ALE-01 and BLA-01. Dotted black line: aligning the formation it's maximum GR value.

To correct the NPHI & DPHI distributions it's data points for the presence of formation clay, the data points have shifted along the wet shale line, by utilizing (Equations **31** & **32** taken from Kurtz, A. D. (2013) **[24]**). Since, it's noticed that after the preceding shale correction, some of the data points still were laying above the clean quartz line. Therefore, their corresponding data points which indicating the presence of gas have corrected, by projecting them on the quartz line by utilizing the slope of 0.667^{03}, as retrieved from Kurtz, A. D. (2013) **[24]**.

In Equations **31** & **32**, the following symbols have noted: V_{cl} the Clavier, C., et al. (1971) [12] based volume of clay distribution $[-]$ (as described in Subsection **2.4.6**), $NPHI_{litho,gas}$ the for sandstone- and gas corrected NPHI log $[-]$ (as described in Subsection **2.4.7**), $\phi_{D_{gas}}$ the for gas corrected DPHI distribution $[-]$, $\phi_{D_{clay,corrected}}$ the for clay- and gas corrected DPHI distribution $[-]$, $\phi_{N_{clay,corrected}}$ the for clay and gas corrected sandstone NPHI distribution $[-]$, $\phi_{D_{wet,clay}}$ the approximated wet clay DPHI value $[-]$, and $\phi_{N_{wet,clay}}$ the approximated wet clay NPHI value $[-]$.

$$\phi_{D_{clay,corrected}} = \phi_{D_{gas}} - (V_{cl}) \cdot (\phi_{D_{wet,clay}}) \tag{31}$$

$$\phi_{N_{clay,corrected}} = NPHI_{litho,gas} - (V_{cl}) \cdot (\phi_{N_{wet,clay}}) \tag{32}$$

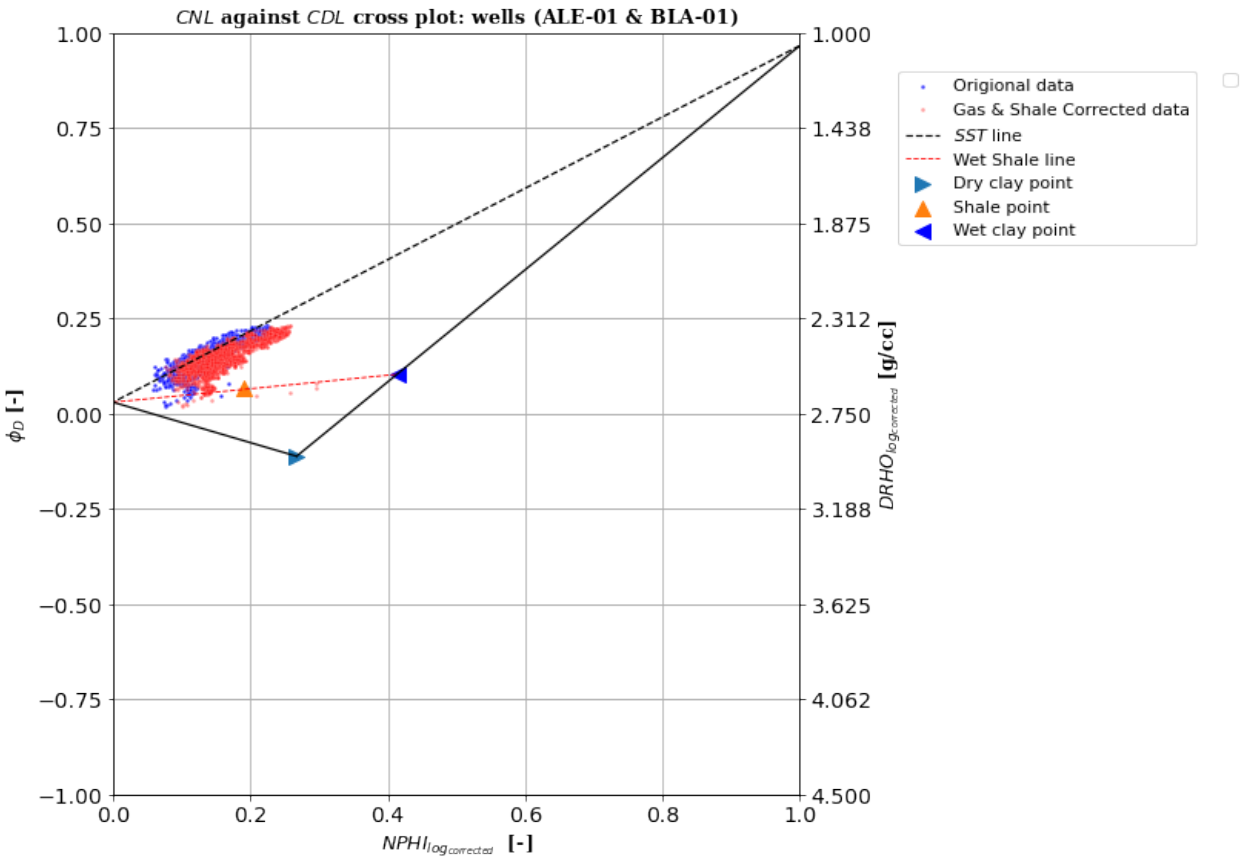

Figure 70: The Compensated Neutron Log (CNL) against the Compensated Density Log (CDL) cross plot along boreholes ALE-01 and BLA-01. Blue coloured points: original corrected log data (as mentioned in Subsection **2.4.7**). Red coloured points: the gas and shale corrected log data. Triangular points: dry clay point, pure shale point, and wet clay point.

The Porosity from the DT log

The DT readers had alongside influenced by the formation it's density and elasticity values. Since, their readers had affected by increasing formation compaction, accordingly it's needed to correct their corresponding DT logs. Therefore, the shale compaction factor has utilized for the Wyllie, M. R. J., et al. (1956) **[45]** porosity relationship (as denoted in Equation **34**).

Since residual formation gas had as well as influenced the DT logs, therefore the pore fluid DT term has be expanded for inclusion of the gas component, and rewritten as denoted in (Equation **33** as retrieved from Peters, E. J. (2012) **[31]**). Due that along boreholes WSP-01 & ERM-01 the flushed zone saturation distributions haven't yet estimated, that is why also for them surface water- and drilling mud resistivity values have retrieved (as listed in Table **23**). Subsequently, the for shale and gas-corrected effective DT porosity distributions have computed along these wells, by utilizing (see Equation **34**).

In Equations **34** & **33** the following symbols are defined: ϕ_{ac} the porosity from the DT log $[-]$, Δt_z the DT log reader $[\frac{\mu s}{ft}]$, Δt_m the formation it's matrix DT value $[\frac{\mu s}{ft}]$ (as listed in Table **7** in Subsection **2.4.4**), Δt_{fi} the formation it's brine fluid DT value $[\frac{\mu s}{ft}]$ (as presented in Appendix **A.11**), Δt_{cl} the dry clay matrix DT value $[\frac{\mu s}{ft}]$ (as noted in Subsection **2.4.4**), Δt_{gas} the mixture of gas DT value denoted to be 626.0 $[\frac{\mu s}{ft}]$ (as retrieved from Peters, E. J. (2012) **[31]**), S_{xo} the flushed zone saturation $[-]$ (as described in Subsection **2.4.7**), Δt_f the gas corrected pore fluid DT distribution $[\frac{\mu s}{ft}]$, and V_{cl} the Clavier, C., et al. (1971) **[12]** based volume of clay distribution $[-]$ (as described in Subsection **2.4.6**).

$$\Delta t_f = \Delta t_{fi} S_{xo} + \Delta t_{gas} \cdot (1.0 - S_{xo}) \tag{33}$$

$$\phi_{ac} = \left(\frac{\Delta t_z - \Delta t_m}{\Delta t_{fi} - \Delta t_m}\right)\left(\frac{100}{\Delta t_{cl}}\right) - V_{cl}\left(\frac{\Delta t_{cl} - \Delta t_m}{\Delta t_{fi} - \Delta t_m}\right) \tag{34}$$

Table 23: Below the surface drilling mud and water resistivity values for wells (WSP-01 & ERM-01) for their surface condition have reported.

Well	$R_{mud,surf}\ [\Omega \cdot m]$	$T_{mud,surf}\ [F^\circ]$	$R_{w,surf}\ [\Omega \cdot m]$	$T_{w,surf}\ [F^\circ]$
WSP-01	$4.50 \cdot 10^{-02}$	$5.90 \cdot 10^{+02}$	$1.73 \cdot 10^{-02}$	$5.90 \cdot 10^{+01}$
ERM-01	$7.70 \cdot 10^{-02}$	$5.72 \cdot 10^{+01}$	$1.51 \cdot 10^{-02}$	$6.62 \cdot 10^{+01}$

A.8.1. The Porosity method Results

All the previous estimated effective (DT, DPHI, NPHI, RHOB) porosity distributions along all boreholes (as illustrated in Figure **71**).

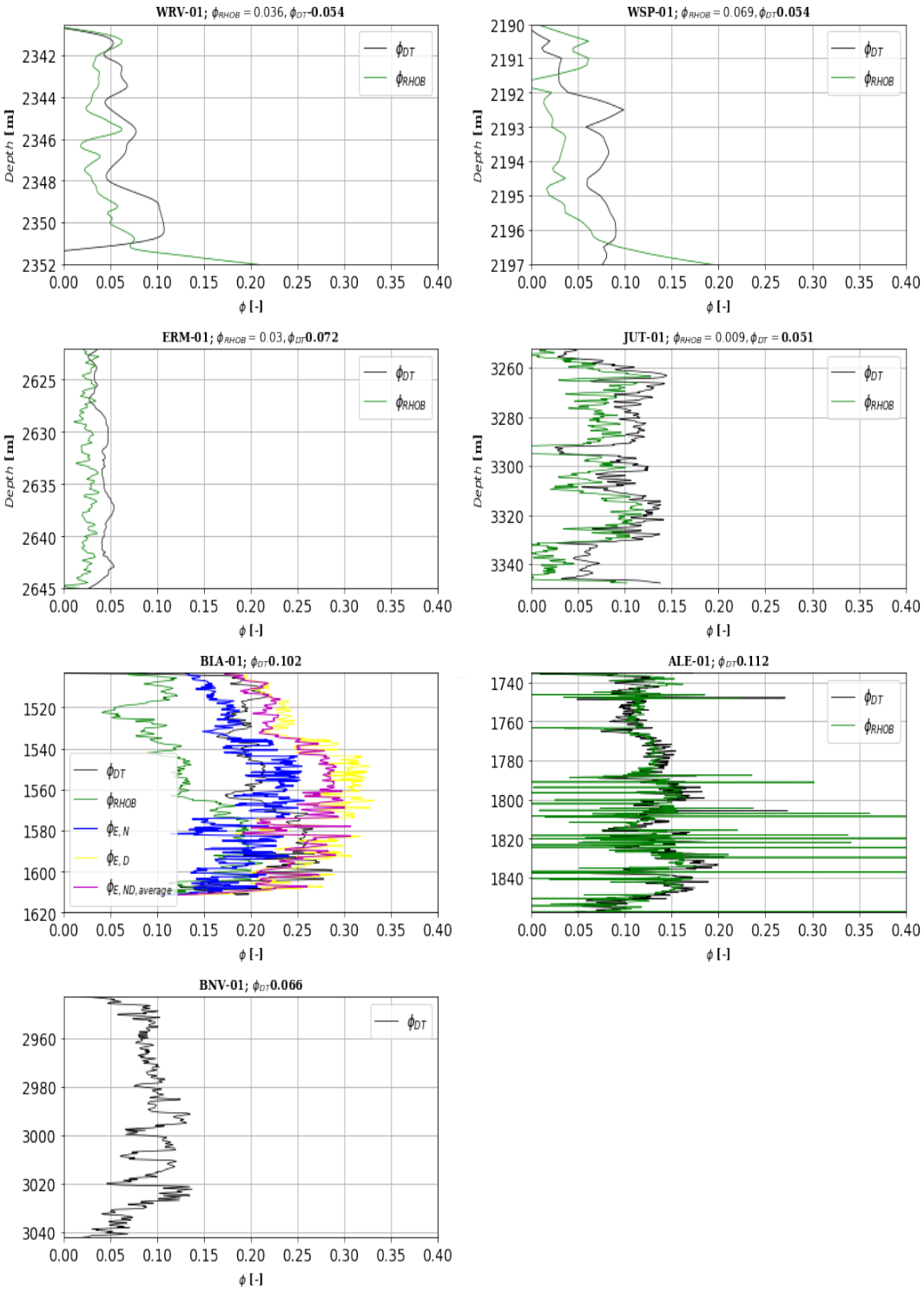

Figure 71: Coloured curves: the effective (DT, DPHI, NPHI & RHOB) porosity distributions shown along all wells.

A.9. Appendix- The RHOB against the DT Cross plot

To compute the DT porosity distributions, it's necessary to find the DT value of the pore fluid. Since, the RHOB value of the pore fluid has previously estimated, as denoted in (Table **7** in Subsection **2.4.4**). Therefore, the DT value of has obtained of 171.01 $[\frac{\mu s}{ft}]$, by approximating a linear correlation based on their DT and RHOB data points (as illustrated in Figure **72**).

In Equation **35** the following symbols have listed: $RHOB_{log}$ the RHOB log reader $[\frac{g}{cm^3}]$, DT_{log} the DT log reader $[\frac{\mu s}{ft}]$, a the slope coefficient $[-]$, and b the y-intercept $[-]$.

$$DT_{log} = a \cdot (\frac{1}{RHOB_{log}}) + b \quad \longrightarrow \quad DT_{log} = 174.836 \cdot (\frac{1}{RHOB_{log}}) + 0.092 \quad , \quad R^2 = 0.992 \tag{35}$$

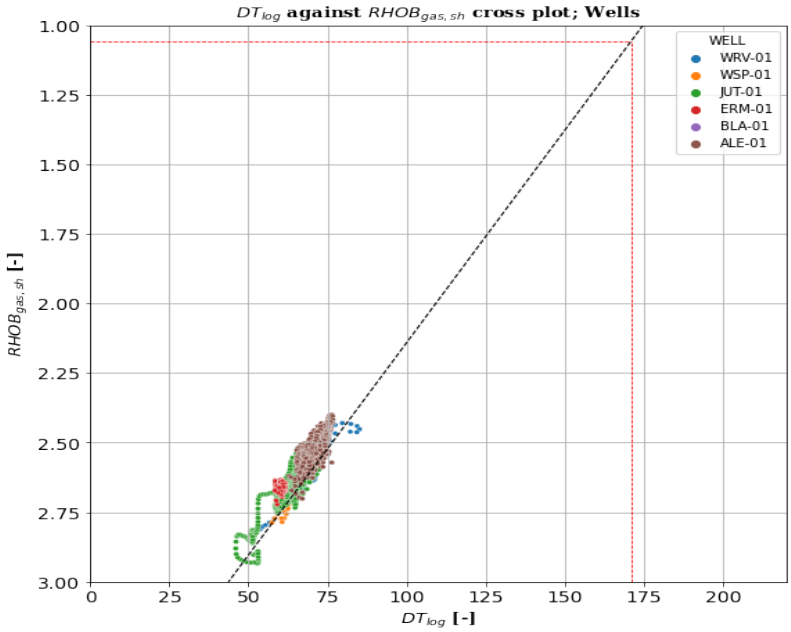

Figure 72: Coloured points: The DT log data points against the RHOB log data points along the six boreholes. Dotted lines: the lines to identify the DT pore fluid value.

A.10. Appendix - The Achies Parameters

To estimate the Archies cementation exponent along the boreholes ALE-01, WSP-01, ERM-01, & BLA-01, which have all available LLD logs. Therefore, the Hingle diagram has plotted, where in effective DT porosity distributions have linearly plotted against the LLD logs (logarithmic) (as illustrated in Figure **73**). Subsequently, the cementation exponent have founded to be 2.4 $[-]$, by correlating the leftmost data points in the graph with the 100% water saturation line. This 100% water saturation line has plotted based on an linear regression of the effective DT porosity data points against the resistivity quotient data points, as presented in Equation **36**. Accordingly, by trial and error it's found that for this cementation exponent, a 100% water saturation quotient holds of 0.0293 $[-]$.

In Equation **36**, the following symbols are defined: R_t the deep lateral resistivity reader form the LLD log $[\Omega \cdot m]$, ϕ_{Vsh} the effective DT distribution based on the I_{GR} volume of clay log $[-]$ (as described in Subsection **2.4.8**), a the tortuosity factor distribution $[-]$, n the saturation exponent $[-]$ (as defined in Subsection **2.4.5**), m the cementation exponent of 2.4 $[-]$, S_w the water saturation equal to 100%, R_w the water resistivity distribution as previously estimated $[\Omega \cdot m]$ (as described in Subsection **2.4.5**), y the scaled resistivity quotient value $[\Omega \cdot m]$, and b the y-intercept $[-]$.

$$y = a \cdot \phi_{VSH} + b \quad \longrightarrow \quad [\frac{1}{R_t}^{\frac{1}{m}}] = [\frac{S_w^n}{a \cdot R_w}]^{\frac{1}{m}} \cdot \phi_{Vsh} \tag{36}$$

The term $[\frac{S_w^n}{a \cdot R_w}]^{\frac{1}{m}}$ with S_w= 100% has denoted to be the slope coefficient a.

Subsequently, along these boreholes Archie, G. E. (1942) **[1]** first law was utilized to approximate the tortuosity constant distributions (as presented in Equation **37**). For this purpose, the formation's resistivity factor distributions, denoted as the ratio between matrix resistivity (R_t) and water resistivity (R_w) have computed (and has retrieved from Worthington, P. F. (1993) **[44]**).

In Equation **37**, the following symbols have arranged: F the formation resistivity factor distribution $[-]$, R_t the deep lateral resistivity reader from the LLD log $[\Omega \cdot m]$, and R_w the estimated water resistivity distribution $[\Omega \cdot m]$ (as described in Subsection **2.4.5**).

$$a = F \cdot \phi_{Vsh}^m \quad \longrightarrow \quad a = \frac{R_t}{R_w} \cdot \phi_{Vsh}^m \tag{37}$$

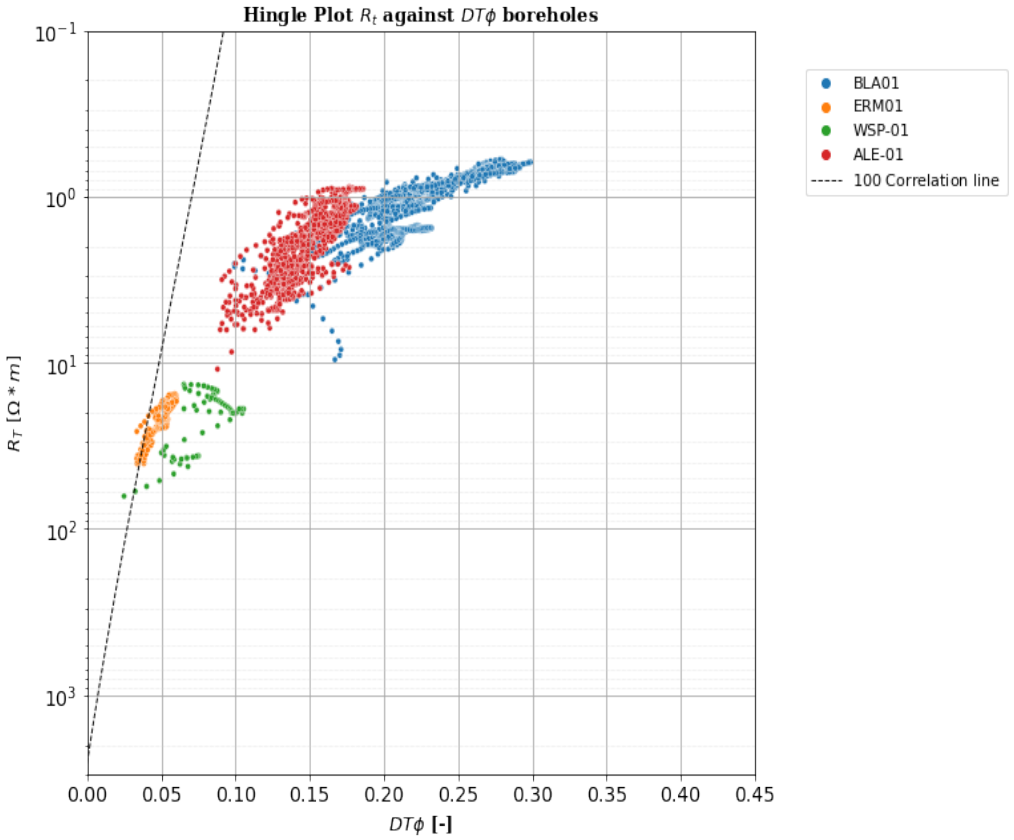

Figure 73: Coloured points: the R_t data points against the $DT\phi_{Vsh}$ data points along boreholes ALE-01, ERM-01, BLA-01 & WSP-01, known to be the Hingle Plot. Black dotted line: the approximated 100% water saturation line.

A.11. Appendix - The Log against the core plug Permeability

Based on the water saturation sensitivity analysis, the resulting Wyllie, M. R. J., et al. (1956) **[45]** based permeability log distributions along borehole BLA-01 have validated against the core plug permeability data points (as illustrated in Figure **74**).

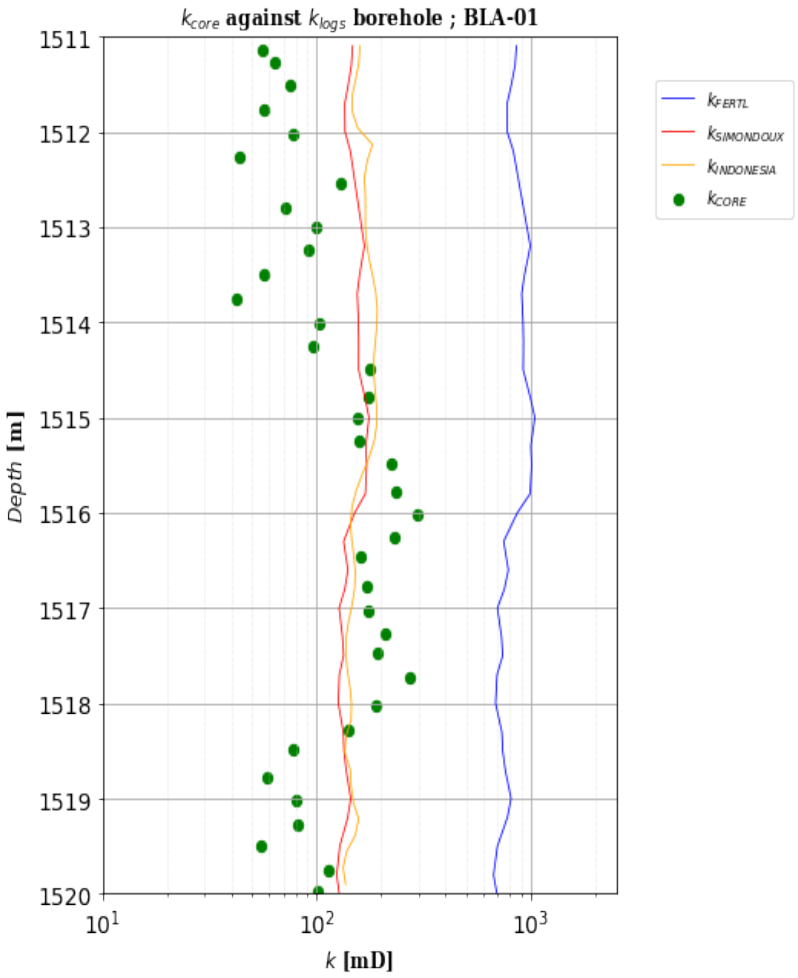

Figure 74: Coloured curves: the permeability distributions based on (Fertl, W. H. (1975) [**15**], Gonzalez, O. (2012) [**19**], and Leveaux, J., & Poupon, A. (1971) [**26**]) based water saturation relationships. Dotted green points: The core plug permeability data points along borehole BLA-01.

A.12. Appendix - The Log porosity against the log Permeability Cross plot

The effective DT porosity based on the I_{GR} volume of clay method data points have plotted against the Leveaux, J., & Poupon, A. (1971) **[26]** based permeability data points, as shown in the cross plot (as illustrated in Figure **75**).

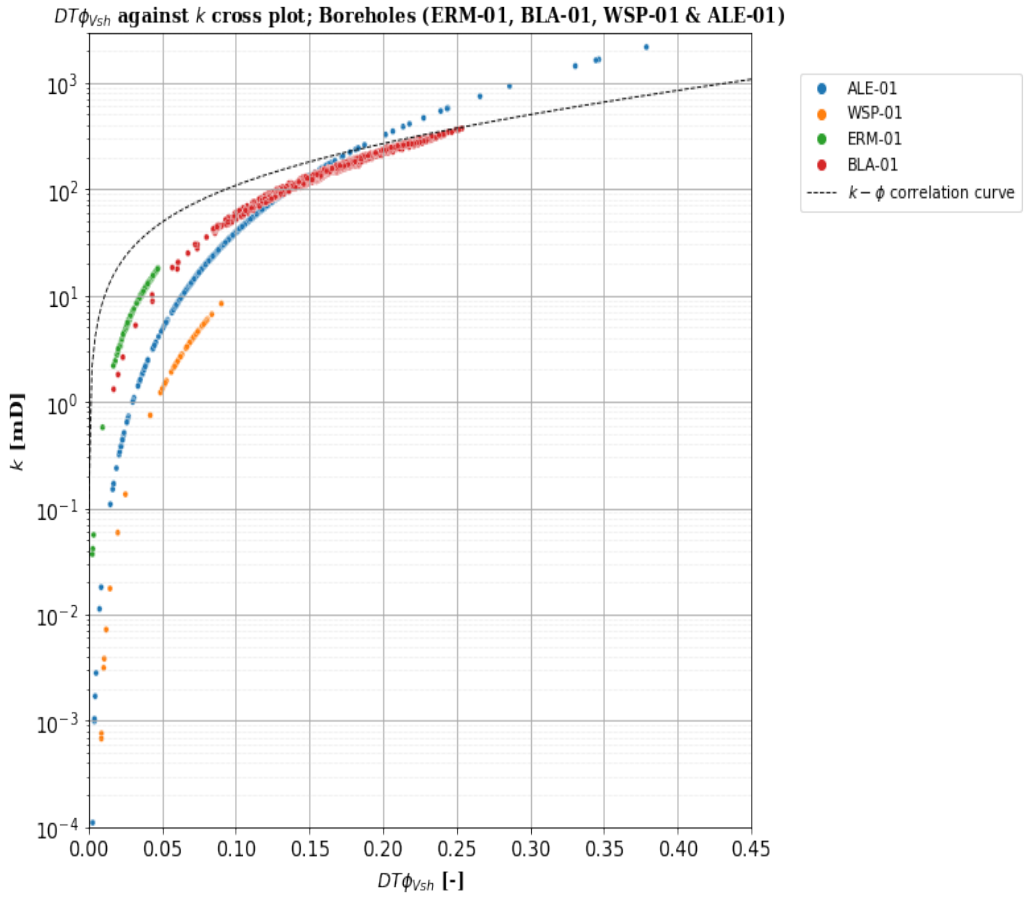

Figure 75: Coloured points: The permeability log data points against the effective DT porosity data points along boreholes (BLA-01, ALE-01, WSP-01 & ERM-01). Black dotted line: The exponential regression curve.

A.13. Appendix H - The Facies log Porosity & log Permeability

As previously described in Subsection **2.4.10**, the resulting facies effective porosity and permeability distributions along all the core intervals have plotted in corresponding histograms (as depicted in Figure **76**).

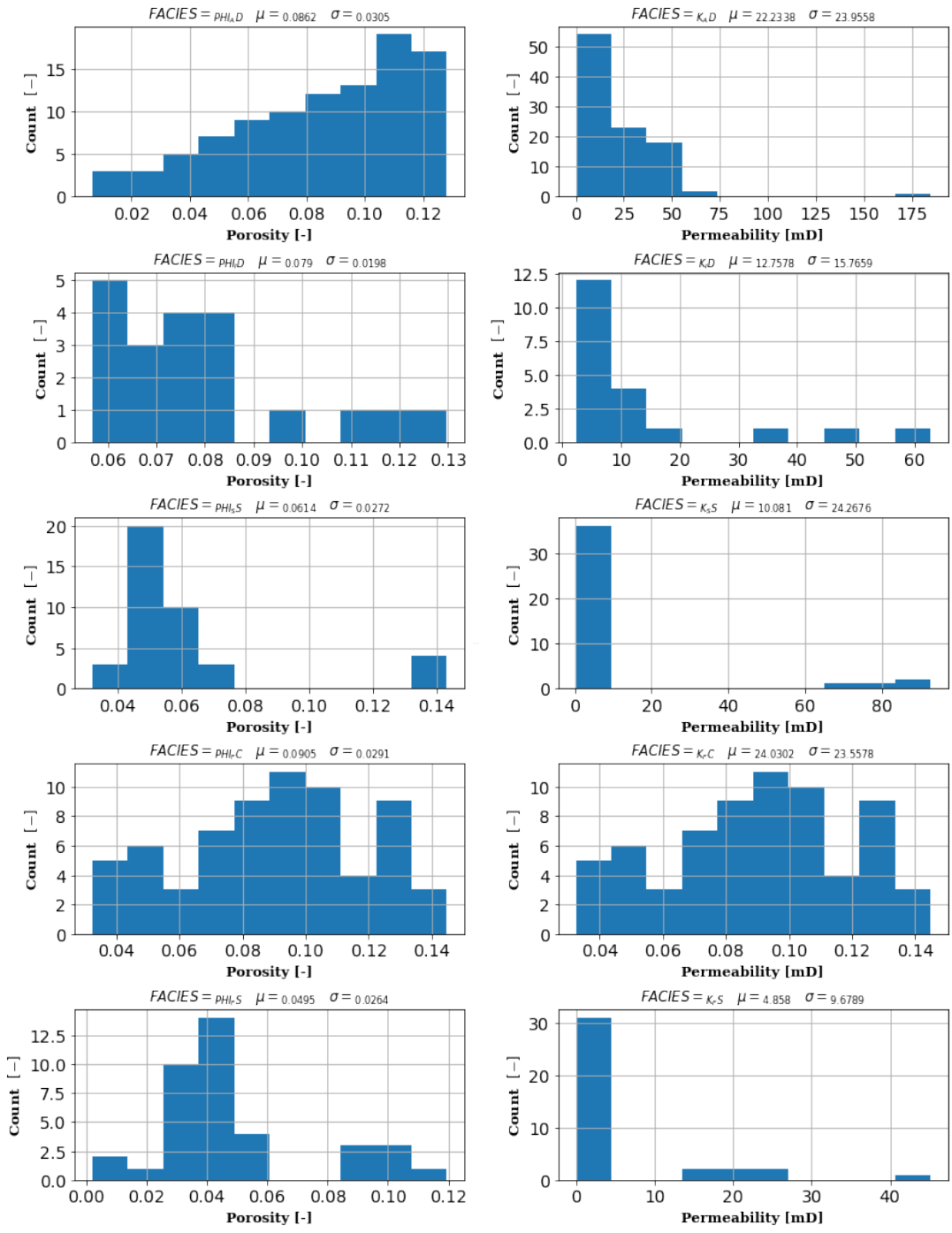

Figure 76: The log porosity (left histograms) distributions and the log permeability (right histograms) distributions along each of the following facies units: SF, AD, SS, FC & SF.

A.14. Appendix - The Facies against Cutting Column comparison

The resulting facies and sand column profiles for the drilling profiles WSP-01, BLA-01, ALE-01, WRV-01 & WRV-01 have compared with cutting interpretations extracted from corresponding borhole reports available in NLOG (see Figure **77**). Their findings indicate that the generated sand column profiles align well with the grain size interpretation columns derived from the cutting interpretations.

However, despite generally matching results, only for drilling profile WSP-01, the cutting interpretation column has deviated from the corresponding sand column. The cutting interpretation identifies a mixture of silt with an interspersed sandstone bed, whereas the resulting sand column predominantly indicates sand with silt beds at the top and bottom of the column. Additionally, for drilling profile ERM-01, the top of the sand column consists of clay, whereas the cutting interpretation column suggests that the formation primarily comprises sandstones.

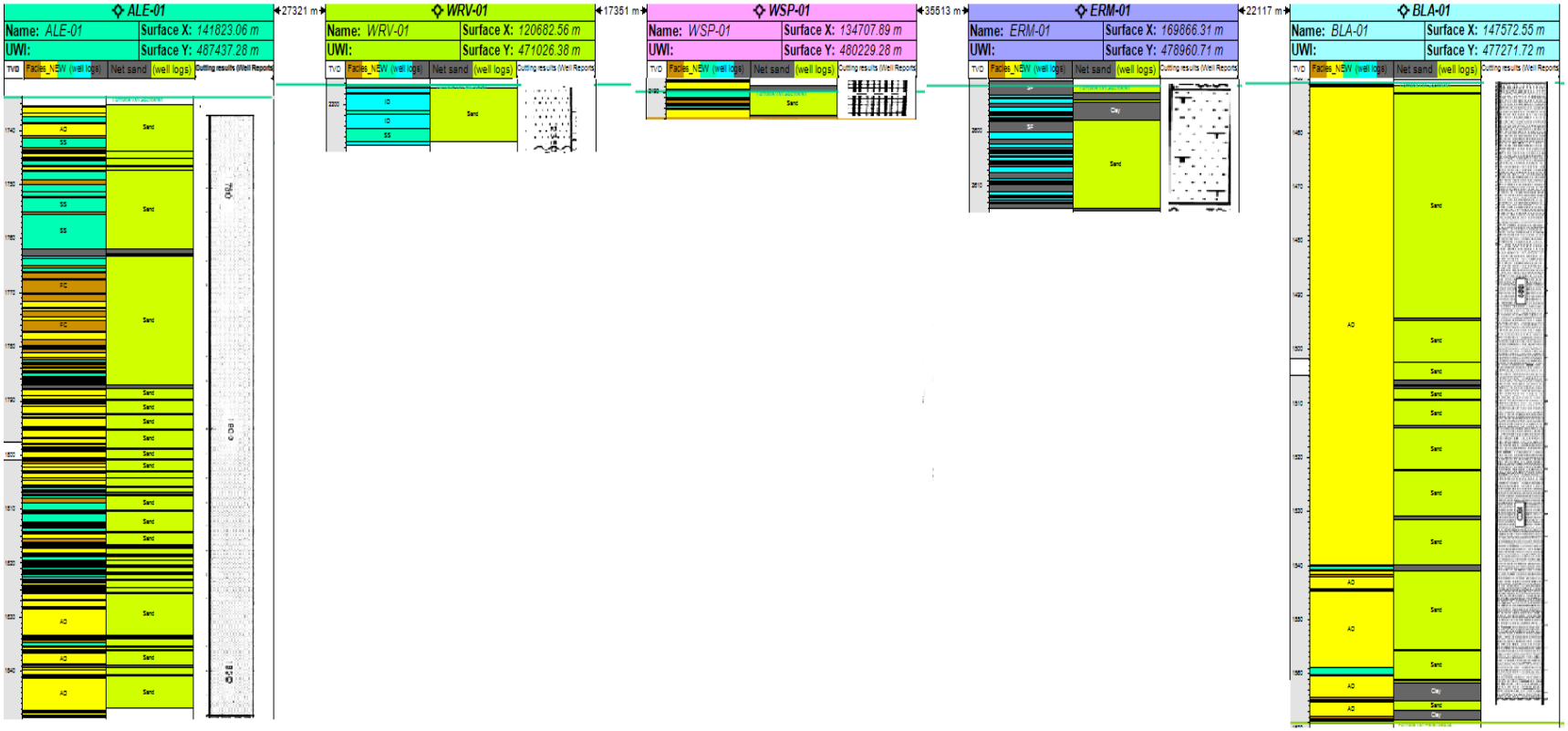

Figure 77: Left log: the upscaled facies column, middle log: the net sand column, and right log: the cuttings image as retrieved from the well report from NLOG. The logs are illustrated for the boreholes ALE-01, BLA-01, WSP-01, WRV-01, & ERM-01.

A.15. Appendix - The Facies Object Based Parameters

As mentioned in Section **3.4**, for the facies units in the stochastic object-based model, their sedimentary morphological- values and distributions have inputted in Petrel. Thus, to create the top and bottom facies maps of the formation, the morphological values and distributions used for their facies have listed below (as presented in Tables **24** & **25**).

Table 24: Below the ephemeral facies (Fluvial Channel (FC), & Flood Sheet (SF)) morphological values and distributions as inputted in Petrel have listed.

Geometry Facies	*Facies [channel & Levee]*	*Orientation [distib: min,mean,max]*	*Amplitude [distib: min,mean,max]*	*Wavelength [distib: min,mean,max]*	*Relative sinousity [distib: min,mean,max]*	*Channel width [distib: min,mean,max]*	*Channel tickness [distib: min,mean,max]*	*Levee width [distib: min,mean,max]*	*Levee thicknesses [distib: min,mean,max]*
Adaptive channels	FC and SF	Triangular: 290,295,300	Triangular:1,2,3	Triangular: 0.5,3,10	Triangular: 0.2,0.3,0.4	Triangular: 0.1,1,3	Triangular: 0.1,0.4,1	Triangular: 1, 75,150	Triangular: 0.1,0.35,0.9

Table 25: Below the aeolian facies (Aeolian Dune (AD), Inter Dune (ID), & Sand Sheet (SS)) morphological values and distributions as inputted in Petrel have listed.

Morphology	**Facies Class**	**Orientation [distib: min,mean,max]**	**Minor Width [distib: min,mean,max]**	**Major/minor [distib: min,mean,max]**	**Thickness [distib: min,mean,max]**
Box	SS	Triangular: 270,257,280	Triangular: 150,300,450	Triangular: 0.5,0.8,1	Triangular: 0.05,0.3,1
Lower half pipe	ID	Triangular: 270,257,281	Triangular: 0.01,1,3	Triangular: 0.1,0.3,1	Triangular: 0.1,0.4,0.9
Aeolian sand dune	AD	Triangular: 270,257,282	Triangular: 2,10,40	Triangular: 0.5,1.5,20	Triangular: 0.5,1.5,20

A.16. Appendix -The OWT Borehole Logs

As previously discussed in Section **3.2**, interval velocity well profiles were used for wells BLA-01, WRV-01, & BNV-01 to generate the 3D velocity model of the formation. Since the interval velocity profiles have generated by utilizing synthetic borehole logs for these wells, and the synthetic drilling profiles have based on One Way Travel Time (OWT) logs, the OWT drilling profiles as used for BLA-01, WRV-01, & BNV-01 are displayed in Petrel, as presented below (as illustrated in Figure **78**).

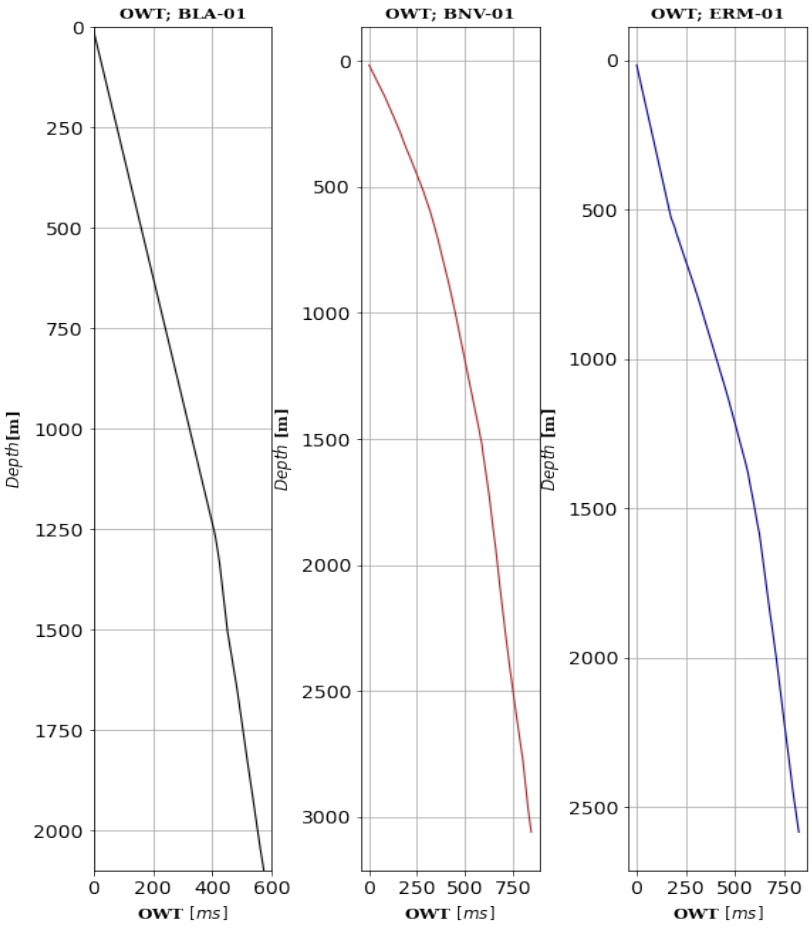

Figure 78: The OWT borehole logs for BLA-01, BNV-01 & BLA-01.


M&L SCIENCE PARK


HermanDeGroot


TU Delft